# Phase Field Crystal Modeling of Active Matter

Dissertation

zur Erlangung des akademischen Grades
Doctor rerum naturalium (Dr. rer. nat.)

vorgelegt

dem Bereich Mathematik und Naturwissenschaften
der Technischen Universität Dresden

von

Francesco Alaimo

geboren am 03. Oktober 1988 in Bologna, Italien

| | |
|---|---|
| Tag der Einreichung: | 04. September 2018 |
| Tag der Verteidigung: | 02. November 2018 |

| | |
|---|---|
| Gutachter: | Prof. Dr. rer. nat. habil. Axel Voigt<br>*Technische Universität Dresden*<br>Prof. Dr. Igor Aronson<br>*Pennsylvania State University* |

# Abstract

Active matter describes systems that convert energy from their environment into directed motion. Therefore, these systems are in intrinsic nonequilibrium, unlike their passive counterparts. From a theoretical point of view, such active systems have been modeled by agent-based models, as well as hydrodynamic approaches, which allowed for the investigation of a wide range of observed collective phenomena characterizing active matter. In this thesis we develop a microscopic field-theoretical approach to describe generic properties of active systems. This description combines the phase field crystal model with a polar order parameter and a self-propulsion term. First, we validate this approach by reproducing results obtained with corresponding agent-based models, such as binary collisions, collective migration and vortex formation. We also perform a direct comparison between our model and a microscopic phase field description of active matter. Next, we use this continuum approach to simulate some larger active systems and to analyze the coarsening process in active crystals, as well as the mechanisms leading to mobile clusters. We show the generality of our approach by extending it to binary mixtures of interacting active and passive particles. Also in this case, we first validate the model by reproducing known results, such as enhanced crystallization via active doping and the suppression of collective migration in an active bath in the presence of fixed obstacles. Interestingly, for the regime of mobile passive particles in an active bath a laning state is found, which is characterized by an alignment of the active particles that is globally nematic, but polar within each lane. This state represents a theoretical prediction feasible to be validated experimentally. Finally, we explore the field of topological active matter. We develop an agent-based model to describe self-propelled particles on curved surfaces and study the complex spatiotemporal patterns that emerge.

# Zusammenfassung

Aktive Materie beschreibt Systeme, die Energie aus ihrer Umgebung in gerichtete Bewegung umwandeln. Im Gegensatz zur passiven Materie befinden sich diese Systeme nie im physikalischen Gleichgewicht und offenbaren dadurch interessante physikalische Phänomene. Vom theoretischen Standpunkt her wurde aktive Materie bereits simuliert, typischerweise durch agenten-basierte Modelle oder hydrodynamische Ansätze, die es ermöglichen eine Vielzahl der auftretenden kollektiven Bewegungsprinzipien zu untersuchen. In dieser Doktorarbeit entwickeln wir einen mikroskopischen Kontinuumsansatz um die generischen Eigenschaften von aktiven Systemen zu untersuchen. Unsere Beschreibung kombiniert das Phasenfeld-Kristall Modell mit einem polaren Ordnungsparameter und einem Antriebsterm. Zuerst validieren wir den Ansatz durch Reproduktion bekannter Ergebnisse agenten-basierter Modelle, wie binäre Kollisionen, kollektive Bewegung und Wirbelformationen. Des Weiteren führen wir einen direkten Vergleich zwischen unserem Modell und einer mikroskopischen Phasenfeldbeschreibung aktiver Materie durch. Danach nutzen wir den kontinuierlichen Ansatz um große aktive Systeme zu simulieren und analysieren den Vergröberungsprozess in aktiven Kristallen und Mechanismen der mobilen Aggregatbildung. Wir illustrieren die Allgemeingültigkeit unseres Simulationsansatzes durch die Erweiterung auf binäre Systeme, in denen sowohl aktive als auch passive Partikel enthalten sind. Auch in diesem Fall validieren wir das Modell durch Vergleiche mit bekannten Resultaten, wie zum Beispiel die verstärkte Kristallisation durch aktives Doping oder die Unterdrückung kollektiver Bewegung durch die Einführung von Hindernissen in einem aktiven Bad. Interessanterweise finden wir bei der Präsenz mobiler passiver Partikel in einem aktiven Bad einen Fahrspur-Zustand, in welchem die aktiven Partikel nematische Fahrspuren bilden und sich nur jeweils innerhalb einer Fahrspur nematisch polar anordnen. Dieser bisher unbekannte Zustand stellt eine theoretische Vorhersage dar, die experimentell geprüft werden kann. Schließlich begeben wir uns auf das Gebiet der topologischen aktiven Materie. Wir entwickeln ein agenten-basiertes Modell um selbst-angetriebene Partikel auf gekrümmten Oberflächen zu beschreiben und untersuchen die dabei auftretenden zeitlich und räumlich komplexen Muster.

# Contents

# Introduction

Active matter provides deep insights into the self-organization of systems that are intrinsically in a nonequilibrium state such as living matter. This intrinsic nonequilibrium is obtained because energy taken up on the microscopic scale can be converted into macroscopic, collective motion. It differs from the standard nonequilibrium observed in passive systems because the system is driven internally, without the presence of external fields. Active particles can be defined as self-propelled units that take up energy from their environment and convert it into directed motion [1–3]. According to this definition, microscopic organisms (e.g. algae and bacteria), as well as more complex ones (e.g. birds and fish), can be classified as active particles and exhibit collective coordinated motion at large scale, such as vortex formation, flocking and swimming [4, 5]. Understanding these collective behaviors is a problem of ever-increasing interest and importance and it is motivating a lot of theoretical and experimental efforts. Theoretically, such behavior can be addressed either from the microscopic scale, taking the interactions into account or from the macroscopic scale, focusing on the emerging phenomena.

From the macroscopic point of view, hydrodynamic approaches aim at establishing a field theory for active matter [1, 6]. In this case methods from nonequilibrium statistical mechanics [7] are used in order to obtain a coarse-grained description of the long timescale behavior of the system in terms of a few, accurately selected, continuum variables. The Toner-Tu model, which describes the dynamics of dry flocks [8–10], and the active polar gel, which describes the dynamics of the cytoskeleton [11–13], are both examples of a hydrodynamic method. However, microscopic details are mostly lost when using such a coarse-grained approach.

Agent-based models are examples for the microscopic viewpoint [14]. In these models, particles move at a constant speed along their orientation and their direction changes according to interaction rules which comprise explicit alignment and noise. They are widely used thanks to their simplicity, efficiency and their ease of implementation. They also often give reliable results about collective phenomena observed in active matter, such as collective migration [15–17] and motility induced phase separation [18–21]. However, these methods cannot be used to describe long time- and large length-scale dynamics, or systems where the particle internal structures and deformations play an important role, such as in migrating tissue cells [22].

Besides these approaches, microscopic phase field models have been proposed in the context of collective cell migration [23, 24]. Each cell is thereby approximated by a deformable phase field variable and the physical processes behind cell motility are considered using an active polar gel theory [11–13]. These are more detailed microscopic descriptions which, unlike a hydrodynamic approach, model the deformation and internal processes within each cell. However, due to the complexity of these models the number of cells which can be considered numerically is limited.

In [25, 26] a microscopic field-theoretical approach that includes aspects from the microscopic and the macroscopic scales has been proposed to model active crystals. It combines the phase field crystal method, introduced to model elasticity in crystalline materials [27, 28], with a polar order parameter and a self-propulsion term. Our aim is to extend this approach in order to describe individual active particles instead of crystals. In doing so, we try to fill the gap between microscopic phase field approaches and agent-based modeling [29]. The resulting model can, in fact, be seen as a coarse-graining of the detailed description given by microscopic phase field methods. Instead of describing the particles by a phase field function, particles are represented by peaks in a particle density field. In this way, the number of particles that can be simulated is larger than for phase field models, but smaller than what is achievable with agent-based modeling. Critically, particle internal structure and, to some extent, deformations, are still accounted for.

In this thesis we validate this microscopic field-theoretical approach and use it to study emerging macroscopic phenomena in active systems with microscopic details, thus combining the efficiency of an agent-based description with the comprehensiveness of a microscopic phase field model.

## Structure of the thesis

Chapters 1 and 2 are introductory chapters where we offer a brief overview over the main concepts and ideas needed to understand the rest of the thesis. Chapter 1 focuses on the mathematical and computational tools needed, such as the phase field crystal model and its modifications, together with a short discussion on how to simulate the resulting system of PDEs. In chapter 2 some physical concepts are introduced. Here we discuss how active matter has been modeled in the last years, from agent-based modeling, through hydrodynamic approaches, to phase field modeling.

In chapter 3 we introduce the active vacancy phase field crystal model, which can be considered as a microscopic field-theoretical approach to active matter. First, we validate this model comparing our results with the ones obtained via agent-based and phase field approaches. To this end we consider binary collisions, collective migration and vortex formation in confined geometries. Finally we show that, thanks to an efficient parallelization algorithm, this newly introduced model can be used to solve large scale problems. In this case we analyze the formation of collective migration and the appearance of large mobile clusters.

An extension of this model towards the description of binary mixtures of interacting active and passive particles is given in chapter 4. Here, we first analyze a collision event between a passive and an active particle, and then we concentrate our attention towards bigger systems. Enhanced crystallization in passive systems via active doping is observed, qualitatively confirming previous experimental and numerical studies. We further study how collective migration is affected by a disordered environment and we show theoretical predictions for an active bath with mobile passive particle, where laning states and chain formations are observed.

Another important field of active matter, namely topological active matter, is treated in chapter 5. In this case, a microscopic agent-based model for nematic active particles on curved surfaces is presented, with a special emphasis on the defects dynamics. Using this model we find oscillations between different defects configurations, a phenomenon that was observed experimentally for the case of a sphere [30]. We also study the connection between the defects location and geometric properties of ellipsoids, such as Gaussian curvature and umbilical points.

Chapters 3, 4 and 5 are based on the following publications:

1. F. Alaimo, S. Praetorius, A. Voigt, *A microscopic field theoretical approach for active systems*, New. J. Phys., 18:083008, 2016
2. F. Alaimo, C. Köhler, A. Voigt, *Curvature controlled defect dynamics in topological*

*active nematics*, Sci. Rep., 7:5211, 2017

3. F. Alaimo, A. Voigt, *Microscopic field theoretical approach for mixtures of active and passive particles*, Phys. Rev. E, 98:032605, 2018

# 1 Theoretical framework

In this first chapter we offer a brief overview over the mathematical and computational tools that will be needed in the rest of this thesis. It can be seen as a useful, though not exhaustive, reference to better understand the concepts and the models introduced in the following chapters. An introduction to the physical system we want to model (active matter) will be given in chapter 2.

We start by introducing the phase field crystal (PFC) model, which can be seen as a microscopic theory for crystallization. We will then show a modification of this model – the vacancy phase field crystal (VPFC) model. The VPFC can be used to describe individual particles via a particle density field and it will be our model of choice in the following chapters. An extension of it that allows for a second species of particles to be introduced in the system, the binary VPFC, is also presented. Next, a coupling between the PFC model and the Navier-Stokes equation is discussed and a fully continuous approach to describe (passive) colloidal suspensions with hydrodynamic interactions is shown. Finally, we concentrate our attention on how to simulate the partial differential equations (PDEs) governing the PFC. We consider a finite element method (FEM) for the spatial discretization of the PFC model (and its modifications), showing how to exploit the strengths of AMDiS, the C++ library that we used, to efficiently solve our PDEs.

## 1.1 The phase field crystal (PFC) model

In this thesis, we want to build a continuum description of active particles more efficient than microscopic phase field approaches, but that, at the same time, contains more information about the particles internal structure than agent-based modeling. The PFC model bridges the gap between molecular dynamics and phase field approaches and is our model of choice. It is a microscopic field approach based on a free energy functional $\mathcal{F}_{\text{pfc}}$ of the time-average density field $\psi(\boldsymbol{r}, t)$ and a dynamical equation for the density evolution. The PFC model has been originally introduced as a phenomenological theory to model elasticity in crystalline materials [27, 28], but it has also been used to describe various solid state phenomena, such as crystal nucleation [31, 32], dendritic growth [32–34] and crack propagation [28]. It has later been shown that the same PFC model can be derived from the overdamped Langevin equations of motion for colloidal particles via dynamical density functional theory [35].

Elder and Grant derived the free energy functional for the PFC model by phenomenological reasoning [28]. Their aim was to build a free energy whose ground state would be given by a spatially periodic structure. They argued that the simplest possible free energy $\mathcal{F}$ that encourages spatial periodicity in its ground state is given by a Swift-Hohenberg-like energy [36]:

$$\mathcal{F}_{\text{SH}}[\phi] = \int_{\Omega} \left\{ \frac{\phi}{2} \left[ a + \lambda(q_0^2 + \nabla^2)^2 \right] \phi + \frac{g}{4}\phi^4 \right\} d\boldsymbol{r}', \tag{1.1}$$

where $\nabla^2$ is the spatial Laplacian operator, $a, \lambda, g$ are system specific parameters and $q_0$ is the wavenumber which sets the lattice distance to $\frac{2\pi}{q_0}$. $\phi$ is the nondimensional one-particle density field defined with respect to a reference density $\bar{\phi}$:

$$\phi = \frac{\phi_{crys} - \bar{\phi}}{\bar{\phi}}, \tag{1.2}$$

where $\phi_{crys}$ is the one-particle density field. $\Omega \subset \mathcal{R}^m$, $m = 1, 2, 3$, is the spatial domain, but we will not consider the $m = 3$ case in this thesis.

Defining the undercooling parameter $r = \frac{a}{\lambda q_0^4}$ and making the following substitutions [37],

$$q_0 \boldsymbol{r}' \to \boldsymbol{r}, \qquad \sqrt{\frac{g}{\lambda q_0^4}}\phi \to \psi, \qquad \frac{g}{\lambda^2 q_0^6}\mathcal{F}_{\text{SH}} \to \mathcal{F}_{\text{pfc}}, \tag{1.3}$$

we obtain the dimensionless PFC functional $\mathcal{F}_{\text{pfc}}$:

$$\mathcal{F}_{\text{pfc}}[\psi] = \int_{\Omega} \left\{ \frac{\psi}{2} \left[ r + (1 + \nabla^2)^2 \right] \psi + \frac{\psi^4}{4} \right\} d\boldsymbol{r}, \tag{1.4}$$

From a more microscopic point of view this functional arises by splitting the Helmholtz free energy in an ideal gas contribution and an excess free energy, rescaling and shifting $\psi$, expanding the ideal gas contribution in real-space and the excess free energy in Fourier-space, and simplifications by removing constant and linear terms that would vanish in the dynamical equations. A detailed derivation of the energy and its relation to classical density functional theory can be found in [35].

The dynamics is given by the following overdamped equation of motion for a conserved field:

$$\frac{\partial \psi}{\partial t} = M_0 \nabla^2 \left( \frac{\delta \mathcal{F}_{\text{pfc}}}{\delta \psi} \right), \tag{1.5}$$

where $M_0$ is a mobility coefficient and $\frac{\delta \mathcal{F}_{\text{pfc}}}{\delta \psi}$ denotes the functional derivative of the PFC functional $\mathcal{F}_{\text{pfc}}$ with respect to the density $\psi$.

Equations (1.1) and (1.5) are the set of equations we refer to when we speak of PFC model. Notice that the equation of motion (1.5) is a sixth-order PDE, a point we will come back to, when speaking about how to simulate the PFC model.

In one dimension the PFC model has two ground states: (i) a periodic state usually given by the one-mode approximation:

$$\psi \simeq A \sin(qx) + \bar{\psi}, \tag{1.6}$$

where $q = \frac{2\pi}{d}$, with $d$ being the distance between two successive maxima in the density $\psi$ (i.e. the 1d lattice distance), and (ii) a constant state given by $\psi = \bar{\psi}$. It is possible to calculate the free energy for both states by inserting the respective densities into the free energy functional (1.4) and minimizing the resulting free energies with respect to the parameters $A$ and $q$. To understand for which system parameters - the undercooling parameter $r$ and the reference density $\bar{\psi}$ - a certain state is reached these free energies must be compared. This is done via a Maxwell construction and the corresponding phase diagram is shown in figure 1.2(a) [28].

In two dimensions the 1d periodic state becomes a striped state, the 1d constant state does not change and we additionally have a 2d periodic state given by (in the one-mode approximation):

$$\psi_t = A \sum_{j=1}^{3} \left( e^{i \boldsymbol{k}_j \cdot \boldsymbol{x}} + e^{-i \boldsymbol{k}_j \cdot \boldsymbol{x}} \right) + \bar{\psi}, \tag{1.7}$$

where $\boldsymbol{k}_{1,2,3} = \hat{x}, (\sqrt{3}/2)\hat{y} \pm (1/2)\hat{x}$. This gives a lattice distance $d = \frac{4\pi}{\sqrt{3}}$. In figure 1.1 snapshots of the periodic and striped states are shown.

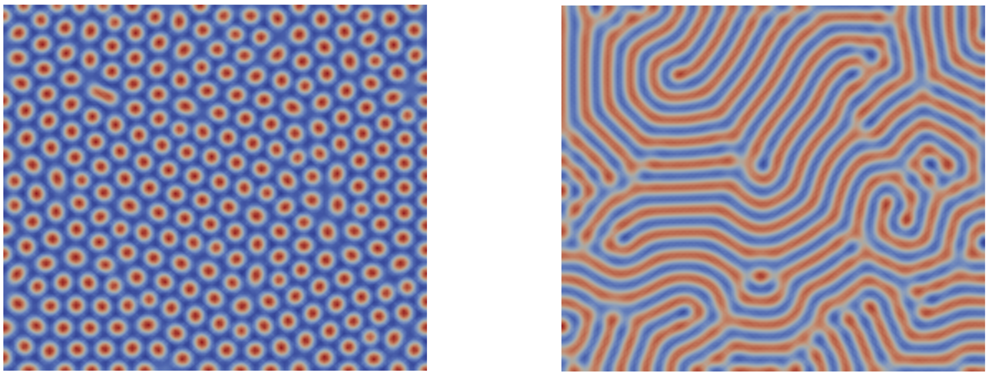

(a)

(b)

Figure 1.1: Two-dimensional PFC simulations obtained numerically solving equation (1.5). (a) Periodic state obtained with parameters $r = -0.4, \bar{\psi} = -0.3$, (b) Striped state $r = -0.4, \bar{\psi} = 0$.

Substituting equation (1.7) for $\psi_t$ into the free energy functional (1.4) gives:

$$\frac{\mathcal{F}_{\text{pfc}}[\psi^t]}{S} = \frac{45}{2}A^4 - 12A^3\bar{\psi} + \frac{\bar{\psi}^2}{4}\left(2 + 2r + \bar{\psi}^2\right) + 3A^2\left(r + 4\bar{\psi}^2\right), \tag{1.8}$$

with $S$ a unit area. Minimizing with respect to A we obtain [28]:

$$\begin{aligned} \frac{\mathcal{F}_{\text{pfc}}[\psi^t]}{S} &= -\frac{1}{10}\left(r^2 + \frac{13\bar{\psi}^4}{50}\right) + \frac{\bar{\psi}^2}{2}\left(1 + \frac{7r}{25}\right) + \frac{4\bar{\psi}}{25}\sqrt{-15r - 36\bar{\psi}^2}\left(\frac{4\bar{\psi}^2}{5} + \frac{r}{3}\right), \\ A &= \frac{1}{5}\left(\bar{\psi} + \frac{1}{3}\sqrt{-15r - 36\bar{\psi}^2}\right). \end{aligned} \tag{1.9}$$

To obtain a phase diagram in two dimensions this free energy density must be compared to the free energy densities of the other two possible ground states: the striped and the constant ones. This is done in [28] and shown in figure 1.2(b), where we observe coexistence regions. Henceforth all our simulations will be in 2d. Figure 1.2(b) tells us for which parameters of $r$ and $\bar{\psi}$ the system will be in the periodic state in this case.

### 1.1.1 Vacancies

The PFC model can be used to describe collective properties of a crystal, but it cannot be used to describe the motion of each individual particle. The peaks (i.e. the maxima) in the local density $\psi$ can be interpreted as particles, but their number is not conserved. In

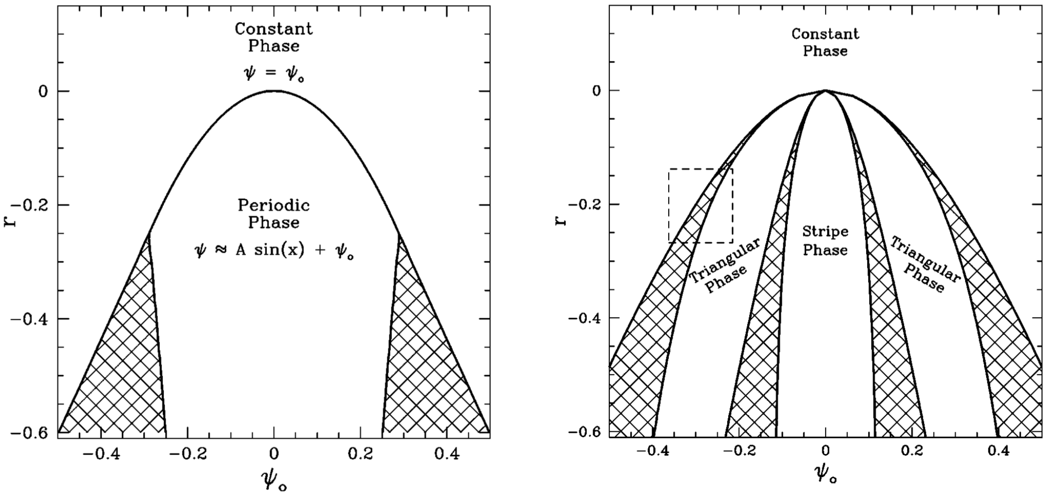

(a) (b)

Figure 1.2: One-dimensional (a) and two-dimensional (b) phase diagram in the one-mode approximation for the PFC model. $\psi_0$ is the average density (called $\bar{\psi}$ in the main text). The hatched area corresponds to coexistence regions. The image is taken from [28].

fact, even if we start with a very low average density $\bar{\psi}$, any configuration will evolve into a perfectly periodic configuration filling the space when the system is in a triangular phase, see figure 1.1(a). In other words, there is no space for vacancies. This is due to the fact that the density $\psi$ can take arbitrary large negative values[1]. Starting from this observation Chan et al. [38] introduced the so-called positivity of density constraint $\psi > 0$ in the whole domain in order to account for vacancies. They have shown that by imposing this constraint the system can partition itself in a region with a periodic configuration and a region with $\psi = 0$. This modified version of the PFC model is known as vacancy PFC (VPFC) model and it can be used to describe the motion of individual particles.

To include the positivity density constraint in the PFC model the free energy $\mathcal{F}_{\text{pfc}}$ must be modified. Any term that introduces a penalty for negative values of $\psi$ is allowed. A typical choice, dictated by numerical stability, is to add the following penalty term [38, 39]:

$$\mathcal{F}_{\text{penalty}}[\psi] = H \int_{\Omega} \left( |\psi|^3 - \psi^3 \right) d\boldsymbol{r}, \tag{1.10}$$

---

[1] Remember that, even though it is called density, $\psi$ is actually a density difference, see equation (1.2). It is for this reason that it can take negative values.

with a penalization parameter $H \simeq 1500$. The final VPFC energy functional reads:

$$\mathcal{F}_{\text{vpfc}} = \mathcal{F}_{\text{pfc}} + \mathcal{F}_{\text{penalty}}, \tag{1.11}$$

while the form of the equation of motion (1.5) remains unchanged, but the free energy $\mathcal{F}_{\text{vpfc}}$ is used instead of $\mathcal{F}_{\text{pfc}}$.

This state where vacancies are accounted for is however not always attainable. We need a phase diagram that tells us for which values of the undercooling parameter $r$ and the average density $\bar{\psi}$ the energy of this configuration is lower than the energy of a perfectly periodic configuration without vacancies. Chan et al. [38] have shown that starting with the one-mode approximation (1.7) and adding the positivity density constraint $\psi > 0$ this separation of phases is obtained when:

$$-\frac{636}{343} < r < -\frac{72}{84}, \qquad \bar{\psi} < \sqrt{\frac{-48-56r}{133}}, \tag{1.12}$$

see also figure 1.3 where the shaded area corresponds to a region where stable vacancies can coexist with a periodic phase.

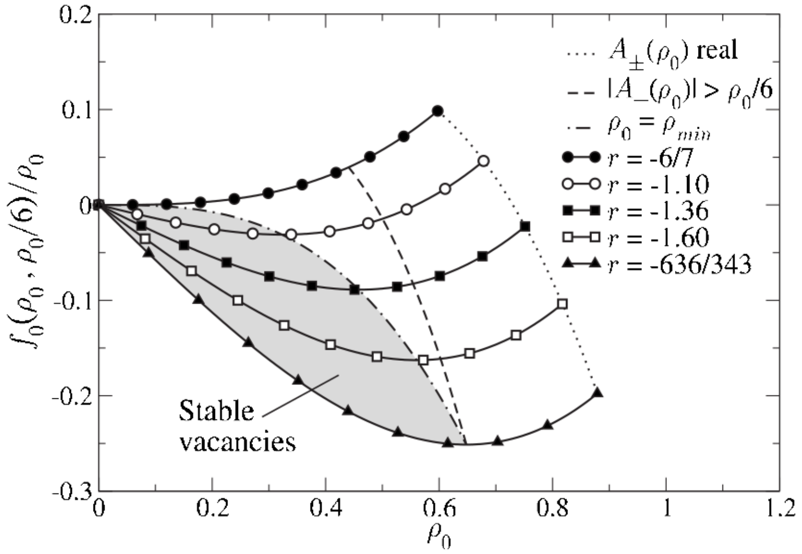

Figure 1.3: The shaded area corresponds to a region where vacancies can be present. $\rho_0$ is the average density (called $\bar{\psi}$ in the main text). Based on the figure we will almost always work with $r = -0.9$ when simulating the VPFC model. The image is taken from [38].

In this regime, the ground state that minimizes the energy functional (1.11) can partition itself into two domains: (i) a perfectly periodic domain with density $\psi_1 = \sqrt{\frac{-48-56r}{133}}$ occupying an area $b_1 = B_0\bar{\psi}/\psi_1$, where $B_0$ is the total area of the domain, and (ii) a domain with $\psi = 0$, corresponding to vacancies.

With the VPFC model we are now able to simulate individual particles instead of crystals. For this reason it is useful to think in terms of total number of particles $N$ in the system instead of an average density $\bar{\psi}$. This can be done by supposing that each particle occupies an area $A_p$. If we want to have $N$ particles we will have $b_1 = NA_p$ and therefore we can write $\bar{\psi}$ as a function of $N$ as:

$$\bar{\psi}(N) = \frac{NA_p}{B_0}\sqrt{\frac{-48-56r}{133}}. \tag{1.13}$$

The lattice distance $d = \frac{4\pi}{\sqrt{3}}$ helps us in quantifying the area occupied by each particle $A_p = \pi(d/2)^2 \simeq 0.78d^2$. However particles are not always perfect circles and $A_p$ should also account for interparticle spacing. Therefore it is usually better to take a slightly higher prefactor for $A_p$, a usual choice being $A_p \simeq 0.9d^2$.

Finally, we need an explicit form for a function that has $N$ peaks (corresponding to $N$ particles), which is continuous and is equal to zero when no particles are present. This function will be used as initial condition when simulating the VPFC model to ensure particles are conserved. In [40] it is proposed to use a composition of local density peaks whose form is given by:

$$\psi_0^{(i)}(\boldsymbol{r}) = \begin{cases} A\left[\cos(\frac{\sqrt{3}}{2}|\boldsymbol{r}-\boldsymbol{r}_i|)+1\right], & \text{for } |\boldsymbol{r}-\boldsymbol{r}_i| < \frac{d}{2} \\ 0, & \text{otherwise,} \end{cases} \tag{1.14}$$

where $\boldsymbol{r}_i$ is the position of particle $i$. Then the density can be written as a sum of these peaks centered around the different particles positions:

$$\psi(\boldsymbol{r}) = \sum_{i=1}^{N} \psi_0^{(i)}(\boldsymbol{r}). \tag{1.15}$$

In figure 1.4 snapshots from different VPFC simulations are shown. It is possible to see that by changing the value of $\bar{\psi}$ also the total number of particles increases, as given by equation (1.13). More importantly the density is always positive (up to some numerical noise) and the particles are not filling the whole space anymore.

Finally, we would like to mention an alternative method to obtain vacancies in the system starting from the PFC model. Instead of adding the positivity density constraint it is possible to set the undercooling parameter $r$ and the mean density $\bar{\psi}$ so that the system is in the coexistence region between a triangular and a constant phase (the left hatched region in figure 1.2(b)). In this case, so-called “localized states” are observed, where vacancies are present in the system, but the density can still assume negative values. [41]. However, in this thesis we will only focus on the VPFC model, without exploring these localized states further.

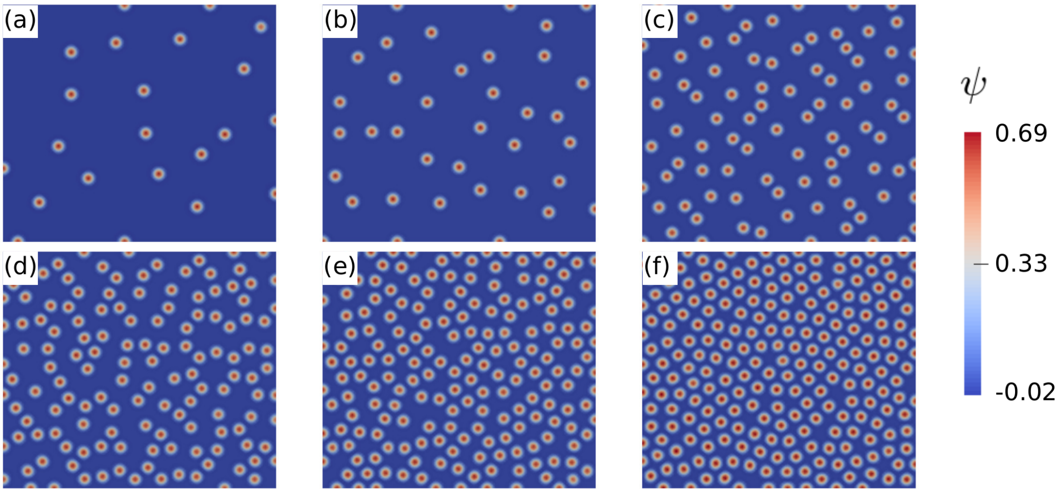

Figure 1.4: Snapshots of different VPFC simulations for $r = -0.9, H = 1500$ and different values of the average densities $\bar{\psi}$. (a) $\bar{\psi} = 0.01$, (b) $\bar{\psi} = 0.02$, (c) $\bar{\psi} = 0.05$, (d) $\bar{\psi} = 0.08$, (e) $\bar{\psi} = 0.11$, (f) $\bar{\psi} = 0.14$. Notice that all these values of $r$ and $\bar{\psi}$ are inside the shaded area of figure 1.3, corresponding to a region where vacancies can be present.

### 1.1.2 Binary mixtures

Various ways have been introduced to extend the classical PFC model towards a second species, thus modeling binary mixtures [34, 39, 42]. We adopt one of these approaches for the VPFC model by considering energies for species $A$ and $B$ with

$$\mathcal{F}[\psi_A, \psi_B] = \mathcal{F}^A_{\text{vpfc}}[\psi_A] + \mathcal{F}^B_{\text{vpfc}}[\psi_B] + \mathcal{F}^{AB}_{\text{int}}[\psi_A, \psi_B], \tag{1.16}$$

where $\mathcal{F}^i_{\text{vpfc}}[\psi_i], i = A, B$ is given by equation (1.11) and

$$\mathcal{F}^{AB}_{\text{int}}[\psi_A, \psi_B] = \frac{a}{2}\psi_A^2\psi_B^2, \tag{1.17}$$

is an interaction energy with $a > 0$. The same overdamped and conservative equation of motion (1.5) is used for both species:

$$\begin{aligned} \frac{\partial \psi_A}{\partial t} &= M_0^A \nabla^2 \left( \frac{\delta \mathcal{F}^A_{\text{vpfc}}}{\delta \psi_A}[\psi_A] + \frac{\delta \mathcal{F}^{AB}_{\text{int}}}{\delta \psi_A}[\psi_A, \psi_B] \right), \\ \frac{\partial \psi_B}{\partial t} &= M_0^B \nabla^2 \left( \frac{\delta \mathcal{F}^B_{\text{vpfc}}}{\delta \psi_B}[\psi_B] + \frac{\delta \mathcal{F}^{AB}_{\text{int}}}{\delta \psi_B}[\psi_A, \psi_B] \right). \end{aligned} \tag{1.18}$$

As in the VPFC model, the peaks in the local density $\psi_A$ ($\psi_B$) are interpreted as particles belonging to species $A$ ($B$). In figure 1.5 we show snapshots of the solution of the binary VPFC, equations (1.18), where the coloring corresponds to an order parameter $\Delta\hat{\psi} = \psi_A/\hat{\psi}_A - \psi_B/\hat{\psi}_B$, where:

$$\hat{\psi}_i = \frac{\psi_A^{\max}\psi_B^{\max} - \psi_A^{\min}\psi_B^{\min}}{\psi_i^{\max} + \psi_i^{\min}}. \tag{1.19}$$

This means that when $\Delta\hat{\psi} \simeq +1$ ($-1$) the local value of $\psi_A$ ($\psi_B$) is high and we have a particle belonging to species A (B).

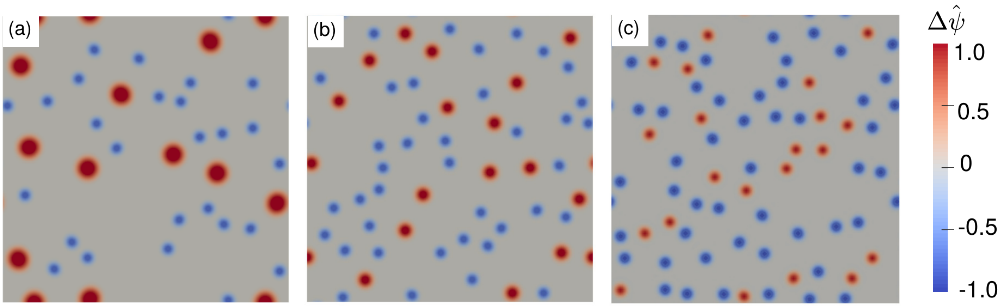

Figure 1.5: Binary VPFC simulations for different values of $q_A$, i.e. the value that controls the size of the particles belonging to species A (red particles). (a) $q_A = 0.5, \bar{\psi}_A = 0.039, \bar{\psi}_B = 0.020$, (b) $q_A = 0.75, \bar{\psi}_A = 0.025, \bar{\psi}_B = 0.032$, (c) $q_A = 1, \bar{\psi}_A = 0.017, \bar{\psi}_B = 0.040$. Other parameters are $r = -0.9, H = 2000, q_B = 1$.

Elder et al. [34] derived a PFC model for binary alloys by linking the PFC with the classical density functional theory of freezing [43]. They used this model to simulate eutectic and dendritic microstructures. See [39] for a discussion on the differences between the model given by equation (1.16) and the one presented in [34].

A straightforward extension of the binary VPFC model is to consider particles with different sizes. To this end, the PFC free energy can be rewritten with an extra parameter

$q$ as:

$$\mathcal{F}^{(q)}_{\text{pfc}}[\psi] = \int_\Omega \left\{ \frac{\psi}{2} \left[ r + (q^2 + \nabla^2)^2 \right] \psi + \frac{\psi^4}{4} \right\} d\boldsymbol{r}. \tag{1.20}$$

In this case the lattice distance is $d_q = \frac{4\pi}{\sqrt{3}q}$. In the case of a single species we can just assume $q = 1$, thus obtaining equation (1.4). For the binary case we can use two different values of $q$ for the two species, thus changing their relative size. Figure 1.5 shows snapshots of the solution of the binary VPFC for varying values of $q_A$ and $q_B = 1$.

### 1.1.3 Hydrodynamic interactions

A possible addition to the standard PFC model is the inclusion of hydrodynamic interactions. This is achieved by coupling the PFC equation of motion (1.5) to the Navier-Stokes equation [25, 40, 44–46]. In particular, in [40] a fully continuous approach suited for the VPFC model is introduced. This is based on the fluid particle dynamics (FPD) method [47] and is used to describe (passive) colloidal suspensions with hydrodynamic interactions.

FPD is a method introduced to model colloidal suspensions that combines continuous and discrete descriptions. Here, colloidal particles are treated as fluid particles with viscosity $\eta_p$, which are suspended in a fluid of viscosity $\eta_f$. We have $\eta_f \ll \eta_p$ and, in the limit $\eta_p/\eta_f \to \infty$, fluid particles become solid ones. A viscosity profile, that is described by a smooth interfacial profile function, is introduced to describe the total viscosity $\eta$. This means that the total viscosity $\eta$ must be equal to $\eta_p$ inside the particles, to $\eta_f$ in the fluid, and it must change continuously when passing between the two regions. In [40] this is achieved by introducing a viscosity profile which depends from the VPFC density $\psi$ as:

$$\eta(\psi) = \left( \frac{\eta_p}{\eta_f} - 1 \right) \phi(\psi). \tag{1.21}$$

$\phi(\psi)$ is a tanh-concentration field used for a phase field description of the particles given by [40, 47]:

$$\phi(\psi) = \frac{1}{2} \left( 1 + \tanh \left( \left( \psi_{(0)} - \sigma \right) \frac{3}{\epsilon} \right) \right), \tag{1.22}$$

where $\sigma = \frac{1}{2}(1 + \cos(a))$ is a shifting parameter with $a$ controlling the width of the phase field function. $\psi_{(0)}$ is the one-mode approximation of the PFC model $\psi_t$ given by equation

(1.7) in two dimensions, rescaled and translated according to:

$$\psi_{(0)} = \frac{1}{2}\left(1 + \frac{\psi_t - \bar{\psi}}{A}\right), \tag{1.23}$$

and $\epsilon$ defines the width of the smoothing region.

In [25, 26] a first coupling between the PFC model and the Navier-Stokes equation based on the FPD method has been introduced. Here, the effects of the moving particles on the surrounding fluid are mimicked by a term $\boldsymbol{F}$ ensuring that the fluid velocity $\boldsymbol{u}$ is equal to the particle velocity $\boldsymbol{v}_i$ at the particle position $\boldsymbol{R}_i$. This term is added as a force to the Navier-Stokes equation and it reads:

$$\boldsymbol{F}(\boldsymbol{r}) = \gamma \sum_{i=1}^{N_p} (\boldsymbol{v}_i - \boldsymbol{u})\delta(\boldsymbol{r} - \boldsymbol{R}_i), \tag{1.24}$$

where $N_p$ is the number of particles (i.e. number of density peaks) and $\gamma > 0$ is a large penalty parameter. The position and velocity of each individual particle need to be calculated to evaluate this term, meaning that this approach still has a discrete component. In [40] it is shown that the force term (1.24) can be approximated as:

$$\boldsymbol{F}(\boldsymbol{r}) \simeq -(M_1 + M_2\psi)\nabla\frac{\delta\mathcal{F}_{\text{vpfc}}}{\delta\psi}, \tag{1.25}$$

with $M_1, M_2$ scalar parameters.

We now have all the ingredients to combine the FPD model with the VPFC approach and obtain a fully continuous description of colloidal suspensions [40]:

$$\begin{aligned}
\partial_t\boldsymbol{u} + (\boldsymbol{u}\cdot\nabla)\boldsymbol{u} &= \nabla\cdot\tilde{\boldsymbol{\sigma}} - M_2\psi\nabla\frac{\delta\mathcal{F}_{\text{vpfc}}}{\delta\psi}, \\
\nabla\cdot\boldsymbol{u} &= 0, \\
\partial_t\psi + \boldsymbol{u}\cdot\nabla\psi &= M_0\nabla^2\frac{\delta\mathcal{F}_{\text{vpfc}}}{\delta\psi},
\end{aligned} \tag{1.26}$$

where:

$$\tilde{\boldsymbol{\sigma}} = -\left(p + M_1\frac{\delta\mathcal{F}_{\text{vpfc}}}{\delta\psi}\right)\boldsymbol{I} + \frac{1}{Re_f}(1 + \eta(\psi))(\nabla\boldsymbol{u} + \nabla\boldsymbol{u}^{\mathsf{T}}). \tag{1.27}$$

$p$ represents a pressure, $Re_f$ is the fluid Reynolds number and $\eta(\psi)$ is the viscosity profile given by equation (1.21).

This fully continuous formulation for colloidal particles with hydrodynamic interactions offers an efficient numerical treatment and it is therefore well suited to describe emerging phenomena on large scale. A coupling with other fields is also in principle possible. For instance, by coupling equations (1.26) with an orientation field it is possible to describe active particles with hydrodynamic interactions. This been done in [25, 26] using equation (1.24) to couple the PFC model and the Navier-Stokes equation. This active PFC model with hydrodynamic interactions will be presented in chapter 2.

## 1.2 Computational details

The equation of motion (1.5) is a sixth-order PDE. Equations (1.18) are two sixth-order PDEs coupled via a repulsion term. In this section we give some information about the methods we used to discretize this system. Further details, such as the elements and the solvers used, initial and boundary conditions and other problem specific parameters, are given inside each chapter. A full mathematical treatment of the numerics needed to solve the PFC equation is given in [48].

A semi-implicit Euler discretization is used for the time discretization. In case more accuracy and stability are required it is also possible to use a Rosenbrock time-discretization scheme [49]. For the spatial discretization of the PFC equation different methods can be used, such as finite difference discretization [50–53] and spectral methods [54, 55]. Spectral methods are however restricted to periodic geometries. These methods are also difficult to use when coupling the PFC equations with other fields, as we will do in the following chapters, and when dealing with complex geometries. A finite element method (FEM) overcomes this problem and it is therefore what we consider for the spatial discretization of the PFC equation. This is implemented using the parallel adaptive finite element framework AMDiS [56, 57].

### 1.2.1 AMDiS

AMDiS is an open source C++ library capable of solving a broad class of PDEs using adaptive finite elements. It is developed and maintained at the Institute of Scientific Computing (TU-Dresden). It can be used to solve stationary and instationary problems in 1d, 2d and 3d and it can handle complex geometries and curved surfaces. It uses the MTL4 and PETSc libraries for sequential and parallel linear algebra computations respectively, allowing the usage of the solvers present in these libraries. In particular, the developing of optimized preconditioners for the iterative solvers, together with the ability to deal with parallel grid, offers the possibility to efficiently run simulations in parallel. The possibility of using an adaptive unstructured mesh is one of its main features. In figure 1.6 we show the meshes used to solve the binary VPFC problem for species A (panel a) and B (panel b). We observe a higher spatial resolution (a finer mesh) where there is a change in the density, i.e. in the proximity of particles, depicted as red or blue circles. In the vacancy regions the density has a constant value equal to zero and this is reflected in a coarser mesh. Notice also how in this case a multi-mesh implementation has been used, with two different meshes for $\psi_A$ and $\psi_B$ [58], which further enhances the efficiency of the simulations.

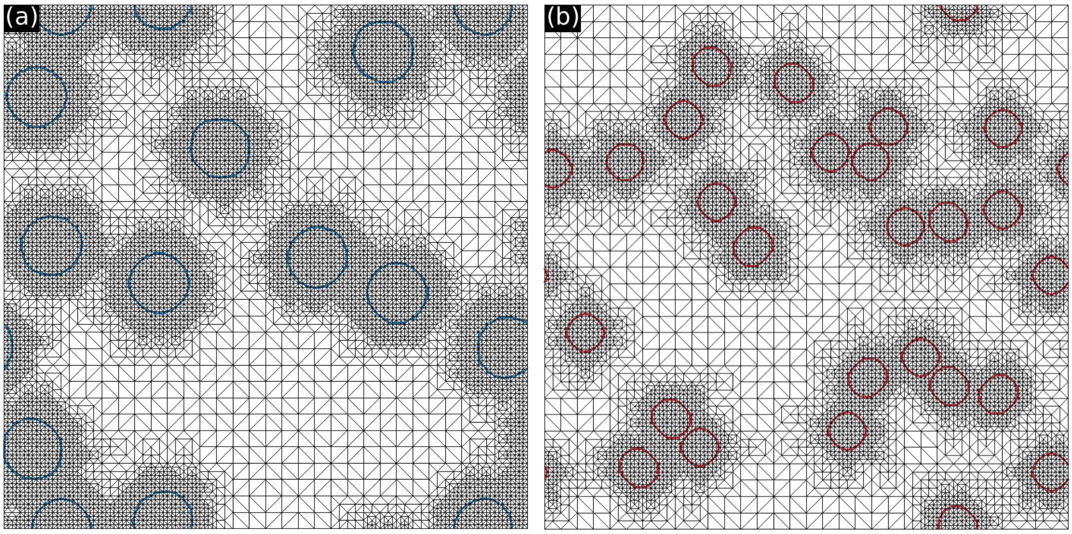

Figure 1.6: Meshes used to solve the binary VPFC equation (1.18). (a) Mesh used to solve the equation for $\psi_A$. The mesh is highly refined in correspondence of particles of species A, represented by red circles. (b) Same as (a) for species B. Notice that the meshes in a) and b) are different, even though $\psi_A$ and $\psi_B$ are coupled. This is possible thanks to a multi-mesh implementation.

### Solving the VPFC equation in AMDiS

We can write down the VPFC dynamical equation explicitly to obtain:

$$\frac{\partial \psi}{\partial t} = M_0 \Delta \left[ \psi^3 + (q^4 + r)\psi + 2q^2 \Delta \psi + \Delta^2 \psi + 3H(\psi|\psi| - \psi^2) \right], \tag{1.28}$$

which can be rewritten as three second-order coupled PDEs:

$$\begin{aligned}
\frac{\partial\psi}{\partial t} &= M_0\Delta\mu,\\
\mu &= \psi^3+(q^4+r)\psi+2q^2\Delta\psi+\Delta\nu+3H(\psi|\psi|-\psi^2),\\
\nu &= \Delta\psi.
\end{aligned} \tag{1.29}$$

Equations (1.29) need to be supplemented by boundary and initial conditions. These are problem specific and are given in the following chapters.

Considering a semi-implicit Euler scheme with timestep $\tau$ and linearizing in $\psi$, the following system needs to be solved in order to obtain $\psi(t_n+\tau)=\psi(t_{n+1})=\psi^{(n+1)}$ within a finite element implementation:

$$\begin{bmatrix} 1 & A_{12}(\psi) & -\Delta \\ -M_0\Delta & \frac{1}{\tau} & 0 \\ 0 & -\Delta & 1 \end{bmatrix}^{(n)} \begin{bmatrix} \mu \\ \psi \\ \nu \end{bmatrix}^{(n+1)} = \begin{bmatrix} R_0(\psi) \\ \frac{\psi}{\tau} \\ 0 \end{bmatrix}^{(n)}, \tag{1.30}$$

where the superscript represents the time at which each matrix is evaluated and

$$A_{12}(\psi) = -3\psi^2-q^4-r-2q^2\Delta-6H(|\psi|-\psi),$$

$$R_0(\psi) = -2\psi^3+3H(\psi^2-\psi|\psi|).$$

The next step in order to obtain a continuum description of active particles is to couple the VPFC dynamical equation, formula (1.29), to an orientation field $\boldsymbol{P}$ via a term $v_0$ representing self-propulsion. This is done in chapter 3. Before, however, we present the field of active matter, with a special focus on the different methods that have been developed to model it.

# 2 Modeling active matter

Active matter is a wide field that has grown in many different directions in the last years. Broadly speaking we can define active systems as systems composed of self-propelled units that take up energy from their environment and convert it into directed motion. This simple fact sets the system in nonequilibrium and collective phenomena can be observed at very different scales, ranging from bacteria colonies to fish schools.

We will begin this chapter by giving a short introduction to active matter, introducing the main ideas and concepts, as well as the new field of topological active matter. However, giving a rigorous overview of active matter goes beyond the purpose of this work (for reviews see [1, 2, 59, 60]). We concentrate our attention only on the modeling aspect of active matter, trying to understand the main features of different models and their context. In general two approaches have been used to model active matter: an agent-based description and continuum theories based on a hydrodynamic approach. We will explain how the former works and where it has been used. In doing so we will introduce the Vicsek model, which is often said to have paved the way for the field of active matter. We will then shift our attention to hydrodynamic approaches, i.e. continuum descriptions of active matter in terms of a few (accurately selected) macroscopic variables[1]. Also in this case we will show one of the most famous examples: the Toner-Tu model, that can be seen as a coarse-grained version of the Vicsek model. We will sketch two possible derivations of this hydrodynamic model: a phenomenological one and a microscopic one. The latter, while more complex from a mathematical point of view, has the advantage of giving explicit expressions in terms of microscopic variables for the parameters entering the model.

---

[1] Note that there exist also continuum, but non hydrodynamic approaches to active matter, such as the one in [61]. However, these will not be considered in this thesis.

We will then move towards a phase field modeling of active matter. Here a phase field variable is introduced to model individual particles, thus allowing for a more accurate description of both the particle internal structure and its shape. This phase field approach is unfortunately very expensive from a computational point of view. It is however possible to study a coarse-grained version of this approach - what we call a “microscopic field-theoretical approach” - that allows to consider a much larger number of particles. This model and two possible applications of it are shortly introduced in this chapter. It will be used and studied more in detail in the following two chapters to study collective phenomena for active particles and for binary mixtures of interacting active and passive particles.

## 2.1 Active particles

Active particles are self-propelled units that convert energy from their environment into directed motion [14]. These systems are in intrinsic nonequilibrium, which differs from standard nonequilibrium in that they are driven internally, as opposed to systems driven by the boundaries or by an external field [1, 2] . Examples of active living systems can be found across many different length scales, from flocks of birds at the macroscale [4] to bacterial colonies at the microscale [5, 62–64], whereas Pt/Au colloids are an example of synthetic microswimmers that can mimic living systems [65].

Active systems are studied both to better understand the mechanism of motility [66] and to investigate collective behavior [67]. An example of the former is spontaneous symmetry breaking and the onset of cell motility [68, 69], whereas the latter concerns nonequilibrium emergent behaviors and macroscopic collective motion [60].

It is possible to classify active systems according to their orientational order. This classification is based on the kind of internal symmetry that the individual particles have in the system. We speak of polar symmetry when the particles have a head and a tail [8, 10, 14]. It is a ferromagnetic-like symmetry because all the particles tend to align in the same direction. Bacteria and schools of fish are a typical example of active systems possessing polar symmetry. The order parameter is a vector $\boldsymbol{p}$, known as the polarization vector. On the other hand, when particles have no head or tail (such as vibrating rods or elongated objects) we speak of nematic symmetry [70–72]. In this case, the particles are active but do not exhibit any mean motion. The order parameter is a tensor and the orientational order is the same that is observed for a nematic liquid crystal [73]. It is also possible that active particles do not posses any orientational symmetry, meaning that no alignment between particles is present. This latter possibility is typical of spherical self-propelled synthetic colloids. In this case, motility induced phase separation (MIPS) can be observed [19], a phenomenon that we will explore in more detail at the end of this chapter.

Furthermore, active particles move in a solvent and therefore their dynamics is affected by hydrodynamic interactions [74–77]. We speak of dry active systems when the medium simply provides friction to the system (and momentum is not conserved). Wet active systems are characterized by a more active role of a medium, where, for instance, the hydrodynamic flow affects the motion of the active particles, like in suspensions [78–80].

Summing up, the defining and underlying features of active systems are: (i) the driving force acts on each unit, meaning that the symmetry is broken locally and not globally, (ii) the presence of emerging behavior: collective coordinate motion at large scale is observed, (iii) most active particles are elongated (synthetic colloids are an exception), meaning that they order in states that have an orientational order, and (iv) the presence of a strong coupling between orientational order, flow (in the case of suspensions) and motion.

### Topological active matter

It is a well-known mathematical fact (Poincaré-Hopf theorem) that it is impossible to cover a sphere (or a topologically equivalent surface, like an ellipsoid) with the lines of a vector field without creating at least a singular point (e.g. the earth longitudinal lines meeting at the poles). This singular point is what is known as a topological defect [81]. Defects are for instance observed when confining passive particles with an orientation on a sphere, see figure 2.1. These defects are however static, but their motion can be induced by adding self-propulsion to the particles.

This is an example of how confining an active system on a curved surface gives rise to new spatiotemporal patterns (in this case the defects dynamics). It has also been proposed that topologically constraining active systems might be a key in morphogenesis [82]. More generally, the study of how topology and curvature affects an active system is what is typically referred to as topological active matter.

Experimental works studied the resulting defects dynamics of confining an active nematics

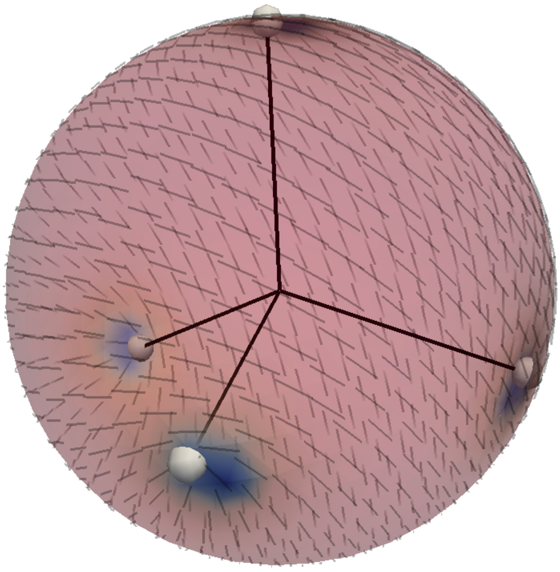

Figure 2.1: Defects, shown as white spheres, arise when confining passive particles with an orientation (shown as black lines) on a sphere. If, as in this case, the particles have a nematic symmetry, four $+\frac{1}{2}$ defects are observed. The color coding corresponds to the nematic order parameter $P$ (see chapter 5) with minima in the four defects.

system comprised of microtubules and molecular motors within a spherical vesicle and a toroidal droplet [30, 83]. Agent-based and hydrodynamic models have been used to study the effects of confining nematic [84–86] and polar systems [87–90] on spheres or ellipsoids. More recently continuum equations for polar orientational ordering and for the nematic liquid crystal on curved surfaces have been derived and used in simulations [91, 92]. These could be used in the future to further study active liquid crystals and polar fluids on evolving surfaces.

Topological active matter remains, however, a quite recent field and the complex dynamics of topological active systems is still largely unexplored. This makes it a fascinating and fast developing new field. We will come back to this topic in chapter 5, where a model to describe dry active nematics on curved surfaces (published in [84]) will be presented in more detail.

## 2.2 Agent-based models

In agent-based modeling the particles in the system are treated as self-propelled units that move with a certain speed (often assumed to be constant) along their orientation. Their direction changes according to interaction rules which can comprise explicit alignment and noise. This is an example of a model on the microscopic scale, where every single unit is taken into consideration and interactions must be known a priori [59]. Even though algorithmic and computational advances allow for simulations of systems containing millions of particles [93], continuous modeling is needed to understand the long time- and large length-scale dynamics of a very large system [1, 2, 94]. Another intrinsic issue in an agent-based approach is that physical interactions between particles or internal symmetries (such as polar or nematic) are imposed as explicit rules. For this reason, agent-based models are not as general as their continuous counterpart. A new set of equations is indeed needed every time that a different interaction is introduced in the system.

These models are however widely used for their simplicity, their ease of implementation and because they have proved to be a valid tool to study emerging phenomena in active matter, such as MIPS [18–21], collective migration [15, 16] and, in more recent years, active dynamics on surfaces [84, 85, 87, 88, 95]. The success of agent-based models is therefore due to the fact that, in their simplicity, they provide a minimal tool to investigate the emergent behavior predicted by more complicated models and observed in the experiments.

Active Brownian Particles (ABPs) are an example of agent-based modeling that has been widely used in the last years [20, 59, 96, 97]. In this framework, particles are represented as repulsive spheres self-propelling with velocity $v_0$. Their translational and rotational dynamics are coupled via rotational diffusion, which induces changes in the particles trajectories. No orientational order is present, meaning that there is no alignment between the particles. The particles dynamics is given by:

$$\begin{aligned}\dot{\boldsymbol{r}}_i &= v_0\boldsymbol{p}_i + \gamma^{-1}\boldsymbol{F}_i + \sqrt{2D_T}\boldsymbol{\xi}(t)\\ \dot{\boldsymbol{p}}_i &= \sqrt{2D_r}\boldsymbol{\eta}(t) \times \boldsymbol{p}_i,\end{aligned} \tag{2.1}$$

where $\boldsymbol{r}_i$ and $\boldsymbol{p}_i$ represents the position and the orientation of the $i$-th particle respectively and $\boldsymbol{F}_i$ represents the forces acting on the $i$-th particle (including steric forces as well). $\gamma$ is the friction coefficient, $D_t, D_r$ are the translational and rotational diffusion coefficients, and $\boldsymbol{\xi}(t), \boldsymbol{\eta}(t)$ represent independent white noise with zero mean and $\langle \xi_\alpha(t)\xi_\beta(t')\rangle = \delta_{\alpha\beta}\delta(t-t')$ (similarly for $\boldsymbol{\eta}(t)$).

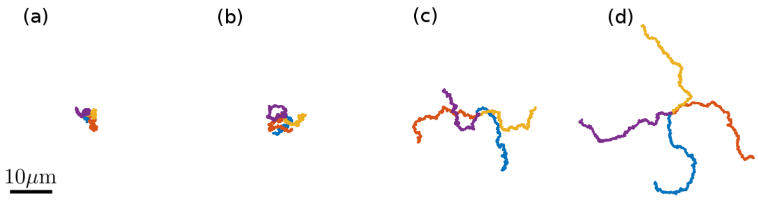

Figure 2.2: Four different equal time trajectories of a single Active Brownian Particle in two dimensions for fixed translational and rotational diffusion $D_T, D_R$. (a) $v_0 = 0$ (corresponding to Brownian motion), (b) $v_0 = 1$, (c) $v_0 = 2$, (d) $v_0 = 3$. By increasing the activity $v_0$ the particle moves over longer distances, before changing its direction because of rotational diffusion. The image is adapted from [59].

In figure 2.2 two-dimensional trajectories of one ABP with $\boldsymbol{F} = 0$ are shown for different values of $v_0$. If $v_0 = 0$ (panel a) the rotational and translational dynamics decouple and we simply observe Brownian motion. Increasing $v_0$ (panels b-d) the particle moves over longer distances, before changing its direction because of rotational diffusion. We will not treat ABP further in this thesis, for a review of this approach see [59], whereas recently ABP with polar alignment has also been introduced [98].

The Vicsek model is considered to have started the field of active matter. A general version of it has been introduced by Reynolds in 1987 in a computer graphics context [99]. A special version of it has been studied in 1995 by Vicsek to study the dynamics of flocks of birds and it has been inspired by an analogy with ferromagnetism [14]. In the following section, we will introduce and analyze this model in more detail to give an explicit example of how agent-based modeling works. The Toner-Tu model [8–10], that will be introduced later, is a coarse-grained approach of the Vicsek model and its study should help us to understand how a continuum theory is constructed and when it can be used.

### 2.2.1 Vicsek model

The Vicsek model was introduced as a minimal numerical model to better understand flocking [14, 100]. It uses a discrete-time cellular automata approach to describe the overdamped dynamics of $N$ points representing self-propelled particles (or birds in the original formulation). The particles travel at a constant speed $v_0$ and try to align their direction of motion with the one of their neighboring particles (inside a sphere of radius

$R$) with some uncertainty due to a noise $\eta_i(t)$. In two dimensions the time-discrete dynamics reads:

$$\begin{aligned} \boldsymbol{r}_i(t+\Delta t) &= \boldsymbol{r}_i(t) + v_0 \hat{\boldsymbol{e}}_i(t+\Delta t)\Delta t \\ \theta_i(t+\Delta t) &= \langle \theta_i(t) \rangle_R + \eta_i(t), \end{aligned} \tag{2.2}$$

where $\boldsymbol{r}_i(t)$ and $\theta_i(t)$ are the position and the angle associated with the orientation of the $i$-th particle at time $t$, $\langle \cdot \rangle_R$ denotes an average over the set particles $j$ inside a circle of radius $R$ from the $i$-th particle: $|\boldsymbol{r}_j(t) - \boldsymbol{r}_i(t)| < R$, and $\eta_i(t)$ is a random angle with zero mean and standard deviation $\eta$:

$$\langle \eta_i(t) \rangle = 0, \qquad \langle \eta_i(t)\eta_j(t') \rangle = \eta \delta_{ij} \delta_{tt'}. \tag{2.3}$$

Notice that equations (2.2) only comprise short-ranged interactions and that the model has rotational symmetry, i.e. the flock is equally likely to move in any direction.

Equations (2.2) describes a system that is fully characterized by the noise amplitude $\eta$, the particles speed $v_0$ and the particles packing fraction $\rho = N/V$, where $V$ is the total volume of the system. In this system, particles move at fixed speed $v_0$, while trying to align their orientation with that of their neighbors.

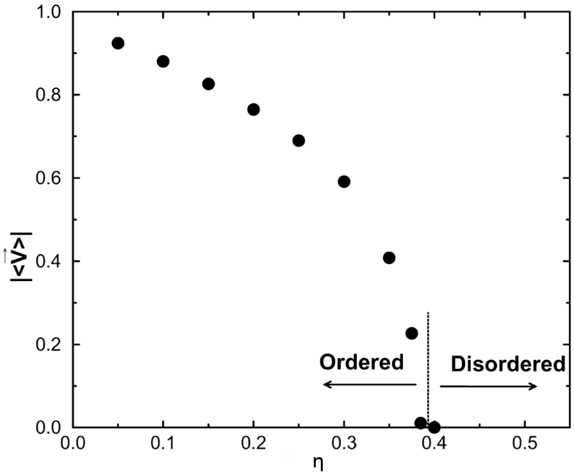

Figure 2.3: Average velocity for a flock described by the Vicsek model, equations (2.2), versus noise strength $\eta$. For low non-zero noise we clearly observe a moving ordered phase ($|\langle \boldsymbol{v} \rangle| > 0$). This phase disappears at a threshold noise value ($\eta \simeq 0.4$), after which a disordered phase ($|\langle \boldsymbol{v} \rangle| = 0$) is observed. The image is adapted from [10].

Simulations showed that for low noise $\eta$ or high density $\rho$ an ordered state where all the particles are on average moving in the same direction (a ferromagnetic flock) is found

[101]. In figure 2.3 it is shown that indeed the average velocity

$$|\langle \boldsymbol{v} \rangle| = \frac{1}{N v_0} \langle | \sum_{i=1}^{N} \boldsymbol{v}_i(t) | \rangle_t \tag{2.4}$$

assumes non-zero values for low noise $\eta$ and we also observe a phase transition from a disordered state ($|\langle \boldsymbol{v} \rangle| \simeq 0$) to an ordered state ($|\langle \boldsymbol{v} \rangle| > 0$) at a critical noise $\eta_c$. The interesting aspect of this ordered state is that it is not imposed by an external field but it arises as the result of *local* interactions between particles. The fact that this ordered state is present also in two dimensions is in apparent contrast with the Mermin-Wagner theorem [102], known to be valid in equilibrium statistical mechanics. This theorem states that no continuous symmetry can be spontaneously broken in an equilibrium system with short-ranged interactions at a non-zero temperature (encoded in the noise in the present discussion) in dimension $d \leq 2$. Figure 2.3 however clearly shows that continuous rotational symmetry is spontaneously broken in the Vicsek model (that has only short-ranged interactions) for a noise amplitude $\eta \neq 0$ and $d = 2$. The answer to this apparent contradiction is that the Vicsek model is out-of-equilibrium. The nonequilibrium aspect comes from particles motion and Vicsek was the first one to realize this. This observation was a big conceptual advancement for the knowledge on flocking and helped in founding the field of active matter.

Figure 2.3 shows a second-order phase transition (i.e. a continuous one), based on simulations of equations (2.2) done in [10]. However, later simulations [103] have shown that, by increasing the system size, the transition becomes discontinuous and a third state, characterized by traveling bands, is observed [101, 103]. It is now accepted that the continuous nature of the phase transition observed in figure 2.3 is due to finite-size effects and that the onset of a moving ordered phase is discontinuous.

The Vicsek model can be made arbitrary complex, by adding new terms and interactions. A lot of possible variations indeed exist and have been studied, such as considering nematic rather than ferromagnetic alignment [104]. However, we have seen that the simple model reported above has already all the necessary ingredients for self-propulsion, nonequilibrium and to account for a spontaneous symmetry breaking, even in two dimensions.

In writing down the Vicsek model different assumptions have been made on how birds (particles) move, such as alignment with their neighbors. This means that a lot of information was needed in order to write down the Vicsek model. Now let's suppose that almost nothing is known about how birds (or self-propelled particles) move and interact. Writing down microscopic equations such as (2.2) is of course not possible given the inability to know which rules to impose. What can be done is to write down a continuum theory, described by certain fields, based on some very generic assumptions and a clever use of the symmetries in the system. This is exactly what is done in a hydrodynamic approach.

## 2.3 Hydrodynamic approach

The aim of a hydrodynamic approach is to offer a continuum description in terms of the dynamics of the so-called slow variables. These are given by conserved quantities, broken symmetry variables and order parameters [6, 105, 106]. In active matter, the motivation for a hydrodynamic approach is given by the need to write down a field theory for it and thus have a coarse-grained description of long time-scale behavior of very large systems given in terms of some continuum fields. The strategies that have been developed to obtain a description of active matter in terms of a few macroscopic fields come from methods of nonequilibrium statistical mechanics [7] and are essentially two: (i) a symmetry-based phenomenological approach and (ii) a full microscopic derivation of hydrodynamic equations. The former approach is based on the symmetries and conservation laws of the system, is very generic and allows us to write down fields equations also when we have very little information about the system. Its main drawback is that the parameters entering the model are undetermined. The microscopic derivation is performed by starting from a specific microscopic model, making several approximations and coarse-graining it. Several calculations are involved, but in the end it is possible to obtain the values of the different parameters entering the equations, overcoming the biggest disadvantage of a phenomenological derivation.

To better understand how a hydrodynamic approach works and its main differences with an agent-based model we are going to introduce the Toner-Tu model, that is essentially a continuous (and therefore more general) version of the Vicsek model. In other words, the Vicsek model is a possible microscopical realization of the Toner-Tu model, corresponding to a specific choice of the phenomenological parameters. Variations of the Vicsek model with, for instance, different alignment rules or attractive interactions, corresponds to other possible realizations of the Toner-Tu model, with a different set of phenomenological parameters. This observation should stress the power and generality -

or better, *universality* - of hydrodynamic approaches.

### 2.3.1 Toner-Tu model

The Toner-Tu model is a continuum theory for dry flocks [8–10]. It has been originally derived using a phenomenological approach only on the basis of the symmetries and conservation laws present in the system [8]. More recently the same model has been derived by coarse-graining the Vicsek model [107–109]. While not giving any explicit derivation of the Toner-Tu model, we will try to sketch the main ideas behind both approaches.

#### Phenomenological approach

In a phenomenological approach, we have very little information about the system we want to model and want to derive a field theory for its long time scale. To this end, the only things we need to know are the symmetries and the conservation laws of the system [106].

Flocks are rotationally invariant, meaning that all directions of space are equivalent to other directions. Furthermore, conservation of particles is assumed. This symmetry and conservation law restrict the terms allowed in the hydrodynamic model. The slow-moving variables in the system are the same of a simple fluid: the density $\rho$ and the coarse-grained particle velocity $\boldsymbol{P}$. These will be the hydrodynamic variables for the Toner-Tu model.

Within this framework, we should be able to write down the most general continuum equations for $\rho$ and $\boldsymbol{P}$ consistent with rotational symmetry and conservation of particles [8–10]. Since we are interested in the long time-scale behavior of very big flocks the equations can be further simplified by performing a gradient expansion, meaning that only the lowest order terms in spatial gradients and time derivatives are kept. The resulting equations read:

$$\begin{aligned}
&\frac{\partial \rho}{\partial t} + \nabla \cdot (\rho \boldsymbol{P}) = 0 \\
&\frac{\partial \boldsymbol{P}}{\partial t} + \lambda_1 (\boldsymbol{P} \cdot \nabla)\boldsymbol{P} + \lambda_2 \boldsymbol{P}(\nabla \cdot \boldsymbol{P}) + \lambda_3 \nabla(|\boldsymbol{P}|^2) = \alpha \boldsymbol{P} - \beta |\boldsymbol{P}|^2 \boldsymbol{P} - \nabla P(\rho) + \\
&+ D\nabla(\nabla \cdot \boldsymbol{P}) + D_1 \nabla^2 \boldsymbol{P} + D_2 (\boldsymbol{P} \cdot \nabla)^2 \boldsymbol{P} + \boldsymbol{f}.
\end{aligned} \tag{2.5}$$

The first equation just states that particles in the flock are conserved. The $\lambda$ terms on the left-hand side of the second equation correspond to the convective term of the Navier-Stokes equation. Here, however, there is no Galilean invariance because “birds” (or particles) move through a resistive medium. This provides a preferential frame and therefore $\lambda_{2,3} \neq 0$. When $\alpha$ changes from negative to positive values the system undergoes a phase transition from a disordered phase to an ordered flock moving with velocity $|\langle \boldsymbol{P} \rangle| \simeq \sqrt{\alpha/\beta}$. The $D$ terms are the diffusion coefficients and basically controls the restoring torque in the ordered flock, representing the equivalent of alignment between neighbors. In this respect, it has been said that “a flock governed by equations (2.5) is a strange blend of magnet and fluid” [2].

All the parameters entering equations (2.5) will not be discussed further here, see instead [1, 2, 10]. However, the phenomenological derivation just shown does not shed any light on their physical meaning. As we have already mentioned, a more systematic derivation is needed in order to obtain explicit expressions for these parameters. In this case the hydrodynamic equations are derived by explicitly coarse-graining the microscopic dynamics given by (2.2) or a similar microscopic model.

### Microscopic derivation

The scope of this section is to explain the general ideas behind the systematic coarse-graining process used to obtain hydrodynamic equations starting from a microscopic model. This is an alternative method to the phenomenological approach described above. It is a more complex process, requiring a lot of mathematics and some approximations, but it provides explicit expressions for the phenomenological coefficients.

The main steps necessary for this coarse-graining operation are essentially three: (i) write down the coupled overdamped Langevin equations for the particles positions and orientations, (ii) transform the Langevin equations into a Smoluchowski equation for the one-particle distribution function [110], and (iii) further coarse-grain the Smoluchowski equation to obtain a set of coupled equations for the slow variables of the system [108, 111].

The methods needed to perform these steps come from nonequilibrium statistical mechanics [7], but are beyond the scope of this presentation. For a detailed derivation see [1, 108, 111] . However, it should be mentioned that the “molecular chaos” approximation (normally used to derive the Boltzmann equation) is needed to complete the calculations and thus obtain a set of coupled closed equations for the hydrodynamic variables. This approximation corresponds to assuming weak interactions and low density in order to express the two-particle probability density as the product of two one-particle probability densities.

Notice that if the microscopic model of step (i) is the Vicsek model, then the hydrodynamic equations that are obtained will correspond to equations (2.5) describing the Toner-Tu model. But this time the phenomenological parameters will be known: they are explicitly given in terms of the microscopic coefficients entering the Langevin equations. It is also possible to start with a different microscopic model. In [112], for instance, the starting point is a microscopic model of a self-propelled hard rod with steric interactions. In this case, the system has a nematic symmetry and therefore the hydrodynamic description contains also a third slow variable: the nematic order parameter $\boldsymbol{Q}$.

A final comment on the explicit expressions that link the phenomenological coefficients of the hydrodynamic model with the parameters entering the microscopic description is necessary. These expressions are dependent on the microscopic model we began with. Starting with two different (but similar) microscopic models might lead to the same hydrodynamic equations, but the connection between the phenomenological coefficients will be given by different expressions in the two cases.

### 2.3.2 Microscopic phase field modeling

Many complex biological phenomena cannot be treated within the agent-based and hydrodynamics frameworks described above. Indeed, when using these approaches it is often not possible to provide a detailed description of the internal structure of the self-propelled particles. Moreover, individual particle deformations, another important feature in many phenomena, cannot be easily incorporated in the methods above as well. Using a phase field description of the particles [113, 114] it is possible to allow for particle deformations, as well as providing a description of internal processes within each particle. This is, therefore, a promising approach to model all those phenomena which need a more detailed description.

Cell motility is a prominent example where an accurate description of the particle interface and internal structure is necessary [115]. Key processes involved in cell motility include, e.g., the interaction of myosin with the actin filaments inside the cell and substrate-related adhesion [116–118]. The underlying mathematical phase field modeling is not trivial. A cell is described by a deformable phase field variable $\phi$ [119], while the surroundings of the cell are regarded as Newtonian fluids. Additionally, when local adhesion of the cell on a substrate is minimal [120], the bulk (i.e. the actin cytoskeleton) can be considered as a solution of actin filaments strongly connected via myosin motors. Actin-myosin interactions lead to an active contractile stress and the dynamics is modeled via an active polar gel theory [11–13]. Figure 2.4 shows a schematic representation of this model.

**The model for the phase field active polar gel**. Here, we want to show the equations governing the phase field active polar gel model used to describe multiple cells in the context of cell migration. We consider $N$ cells and cell $i$ is described by the phase field variable $\phi_i$, with $i = 1..N$. The average orientation of the actin filaments in cell $i$ is represented by the orientation field $\boldsymbol{P}_i$, $i = 1..N$. The governing equations for cell $i$ are given by three different coupled PDEs [24, 68, 121]:

- a fourth order PDE for the phase field variable $\phi_i$:

$$\begin{aligned}
&\partial_t \phi_i + \boldsymbol{\nabla} \cdot (\boldsymbol{u}\phi_i) = \gamma \Delta \phi_i^\natural \\
&\phi_i^\natural = \frac{1}{Pa}\left(-\frac{c_4}{2}|\boldsymbol{P}_i|^2 - \beta_1 \boldsymbol{\nabla} \cdot \boldsymbol{P}_i\right) - \frac{\mu}{Ca} + \frac{1}{In}\left(B'(\phi_i)\sum_{\substack{j=1\\ j\neq i}}^{N} w_j + w_i' \sum_{\substack{j=1\\ j\neq i}}^{N} B(\phi_j)\right) \\
&\mu = \epsilon \Delta \phi_i - \frac{1}{\epsilon}(\phi_i^2 - 1)\phi_i,
\end{aligned} \tag{2.6}$$

where the last term in the second equation represents the repulsive interaction energy between different cells, $B(\phi_i) = \frac{1}{\epsilon}(\phi_i^2 - 1)^2$,

$$w_j = \begin{cases} \exp[-\frac{1}{2}(\ln \frac{1+\phi_j}{1-\phi_j})^2], & \text{for } |\phi_j| < 1 \\ 0, & \text{otherwise,} \end{cases} \tag{2.7}$$

$\epsilon$ represent the thickness of the diffuse interface and $\mu$ accounts for surface tension effects.

- a PDE for the hydrodynamic variable $\boldsymbol{P}_i$:

$$\begin{aligned}
&\partial_t \boldsymbol{P}_i + (\boldsymbol{u} \cdot \nabla)\boldsymbol{P}_i + \boldsymbol{\Omega} \cdot \boldsymbol{P}_i = \xi \boldsymbol{D} \cdot \boldsymbol{P}_i - \frac{1}{\kappa}\boldsymbol{P}_i^\natural \\
&\boldsymbol{P}_i^\natural = \frac{1}{Pa}\left(-c_1\phi_i \boldsymbol{P}_i + \frac{c_4}{2}\boldsymbol{P}_i^2 \boldsymbol{P}_i - \Delta \boldsymbol{P}_i + \beta_2 \boldsymbol{\nabla}\phi_i\right),
\end{aligned} \tag{2.8}$$

where $\boldsymbol{\Omega} = 1/2(\nabla \boldsymbol{u}^{\mathbf{T}} - \nabla \boldsymbol{u})$ is the vorticity tensor and $\boldsymbol{D} = 1/2(\nabla \boldsymbol{u} + \nabla \boldsymbol{u}^{\mathbf{T}})$ is the deformation tensor. This equation can be derived from the active polar gel theory [11–13].

- the incompressible Navier-Stokes equation for the fluid velocity $\boldsymbol{u}$:

$$\begin{aligned} Re\,(\partial_t \boldsymbol{u} + (\boldsymbol{u} \cdot \boldsymbol{\nabla})\boldsymbol{u}) + \boldsymbol{\nabla} p &= \boldsymbol{\nabla} \cdot \boldsymbol{\sigma} \\ \boldsymbol{\nabla} \cdot \boldsymbol{u} &= 0. \end{aligned} \tag{2.9}$$

The stress tensor $\boldsymbol{\sigma}$ have different contributions:

$$\boldsymbol{\sigma} = \boldsymbol{\sigma}^{\text{viscous}} + \boldsymbol{\sigma}^{\text{active}} + \boldsymbol{\sigma}^{\text{distortion}} + \boldsymbol{\sigma}^{\text{ericksen}}, \tag{2.10}$$

the most important of which is the active one $\boldsymbol{\sigma}^{\text{active}}$. This is the term that sets the system out of equilibrium. It basically represents the role of the myosin motors linked to the actin filaments. Mathematically it is given by [2, 122]:

$$\boldsymbol{\sigma}^{\text{active}} = \xi \sum_{i=1}^{N} \boldsymbol{P}_i \otimes \boldsymbol{P}_i, \tag{2.11}$$

where $\xi > 0$ for contractile activity and $\xi < 0$ for extensile activity.

The formula for each of the remaining stress contributions, as well as an explanation of all the parameters and other details can be found in [68, 121]. For some applications of this model see [23, 69, 123–125], whereas an obvious extension has to do with the inclusion of substrate adhesion [23].

**Dry version**. For comparison with other models, it is useful to introduce a dry model (i.e. without the Navier-Stokes equation) of this microscopic phase field formulation of active matter. This is not as easy as simply removing the Navier-Stokes equation, formula (2.9), because this would mean losing the transport term as well as forces and stress. We consider the following model instead [24, 121]:

$$\begin{aligned} \partial_t \phi_i + v_0 \nabla \cdot (\phi_i \boldsymbol{P}_i) &= \gamma \Delta \phi_i^{\natural}, \quad i = 1..N \\ \partial_t \boldsymbol{P}_i + (v_1 \boldsymbol{P}_i \cdot \nabla)\boldsymbol{P}_i &= -\frac{1}{\kappa} \boldsymbol{P}_i^{\natural}, \quad i = 1..N \end{aligned} \tag{2.12}$$

where the chemical potential $\boldsymbol{P}_i^{\natural}$ and $\phi_i^{\natural}$ are defined as above. We refer to this model as

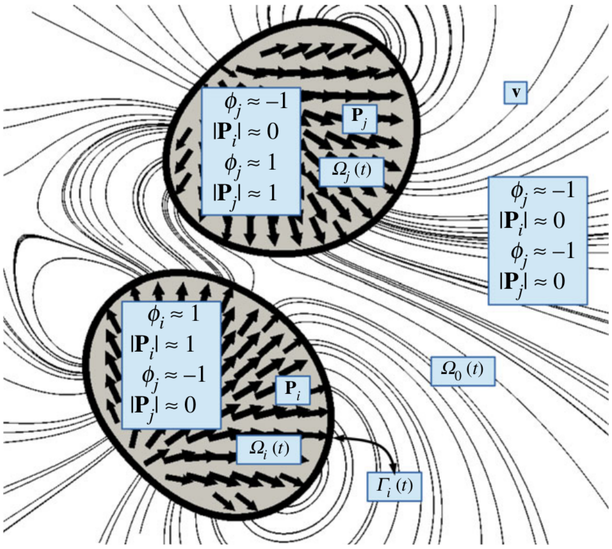

Figure 2.4: Schematic representation of the phase field model used to describe two moving cells. The microscopic actin filaments are coarse-grained and represented by an orientation field $\boldsymbol{P}_{i,j}$. The streamlines of the velocity profile $\boldsymbol{v}$ (called $\boldsymbol{u}$ in the main text) of the surrounding Newtonian fluid are shown, as well as the cell membrane $\Gamma_{i,j}(t)$, corresponding to the zero-level set of the phase field $\phi_{i,j}$. The image is taken from [24].

the dry version (or non-hydrodynamic) of the phase field active polar gel model and we will use it in chapter 3 to perform some qualitative comparisons with the microscopic field-theoretical approach introduced in the next section.

The main drawback of a phase field approach is its complexity on a computational level. Even though different methods exist to numerically solve the phase field active polar gel model, including an efficient parallel one for the dry version [126], solving its equations remains a very expensive task. In [25, 26] a new continuum modeling approach was introduced for active crystals. This can be seen as a coarse-grained description of the phase field model just presented. In this method, particles are not described anymore by a phase field function, but they are represented by the peaks in the PFC density field $\psi$ introduced in the previous chapter. This coarse-grained method, named microscopic field-theoretical approach, accounts for particle internal structure and, to some extent, deformations but allows one to consider a much larger number of particles.

## 2.4 Microscopic field-theoretical approach

A microscopic field-theoretical approach has been first introduced to model active crystals [25, 26]. It was intended as a minimal model for crystallization in active systems and it is the first continuum model including both orientational and translational ordering. This new field approach, that can be seen as a coarse-grained model of the detailed phase field descriptions of the previous section [23, 24], provides the ability to study emerging macroscopic phenomena in active systems with microscopic details.

This approach combines the phase field crystal (PFC) model introduced in chapter 1 with a polar order parameter $\boldsymbol{P}$ similar to the one of the Toner-Tu model and a self-propulsion term $v_0$. The model reads in scaled units:

$$\begin{aligned}\partial_t \psi &= M_0 \Delta \frac{\delta \mathcal{F}}{\delta \psi} - v_0 \nabla \cdot \boldsymbol{P} \\ \partial_t \boldsymbol{P} &= \Delta \frac{\delta \mathcal{F}}{\delta \boldsymbol{P}} - D_r \frac{\delta \mathcal{F}}{\delta \boldsymbol{P}} - v_0 \boldsymbol{\nabla} \psi.\end{aligned} \tag{2.13}$$

See the supplement in [25] for a detailed non-dimensionalization of the equations, which can be derived from microscopic dynamical density functional theory [127, 128]. The energy functional is $\mathcal{F} = \mathcal{F}_{\text{pfc}} + \mathcal{F}_{\boldsymbol{P}}$, where $\mathcal{F}_{\text{pfc}}$ is the dimensionless PFC energy functional given by equation (1.4) and the polarization dependent part reads:

$$\mathcal{F}_{\boldsymbol{P}}[\boldsymbol{P}] = \int_\Omega \left[ \frac{1}{2} C_1 \boldsymbol{P}^2 + \frac{1}{4} C_4 (\boldsymbol{P}^2)^2 \right] d\boldsymbol{r}, \tag{2.14}$$

with $C_4 \geq 0$ to ensure thermodynamic stability (with a strict inequality in the $C_1 \leq 0$ case). To understand the role of the other parameters, we can compare the equation for the polar order parameter $\boldsymbol{P}$ to the second equation of the Toner-Tu model, expression (2.5). To this end, we insert (2.14) into the second equation of (2.13) to obtain:

$$\partial_t \boldsymbol{P} = \Delta(C_1 \boldsymbol{P} + C_4 \boldsymbol{P}^2 \boldsymbol{P}) - D_r (C_1 \boldsymbol{P} + C_4 \boldsymbol{P}^2 \boldsymbol{P}) - v_0 \nabla \psi. \tag{2.15}$$

Neglecting the convection terms ($\lambda_i = 0$) and the noise ($\boldsymbol{f} = 0$) and setting $D = D_2 = 0$ in equation (2.5) of the Toner-Tu model, we recover equation (2.15) with $v_0 = 0$, up to the $\Delta(C_4 \boldsymbol{P}^2 \boldsymbol{P})$ term that contributes to translational diffusion. This analogy allows us to better understand the orientational behavior of the active crystals described by equation (2.13). The case $C_1 \geq 0$ in (2.15) corresponds to $\alpha \leq 0$ in (2.5), i.e. a disordered phase. In this case, orientational ordering causes an increase of the polarization free energy

(2.14) and is not favored, meaning that collective ordered motion is in general avoided. An activity threshold for the movement of the active crystals described by equation (2.13) is indeed observed when $C_1 \geq 0$, see figure 2.5 (blue dots and red rhombi). Here, the crystals start to move only when the activity strength $v_0$ increases above a certain threshold value. On the contrary, for $C_1 < 0$ in (2.15) an ordered phase is energetically favorable, meaning that movement is observed for every value of $v_0 \neq 0$, see figure 2.5 .

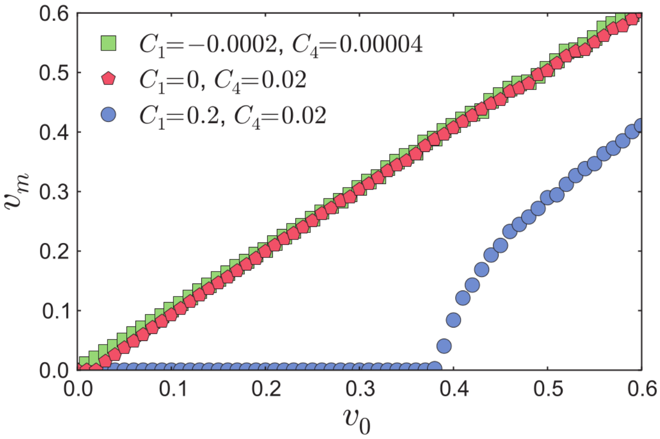

Figure 2.5: Collective migration speed $v_m$ of the active crystals as a function of the activity strength $v_0$. The parameters are $(r, \bar{\psi}, D_r) = (-0.98, -0.4, 0.5)$. For $C_1 \geq 0$ (blue dots and red rhombi) a non-zero activity threshold is observed. This is a consequence of the fact that in this case orientational order is energetically unfavorable, as explained in the main text using an analogy with the Toner-Tu model. For $C_1 < 0$ an ordered phase is energetically favorable and $v_m = v_0$ for every value of $v_0$. The image is taken from [26].

In figure 2.6 snapshots taken from [25] show different phases of the active PFC model for the more interesting $C_1 > 0$ regime. We see that, apart from the activity threshold effect explained above, also other new phases are observed and the activity strength $v_0$ allows transitions between these phases. For low activities, the usual resting hexagonal structure typical of the PFC model is observed (panel a). Increasing $v_0$ this structure starts moving and we have a traveling hexagonal structure (panel b). This transition occurs at a specific threshold value $\tilde{v_0}$ which varies according to the values of the other parameters in the system. By further increasing $v_0$ a traveling quadratic structure is observed (panel c) until, for an even higher activity strength, traveling lamellae are found (panel d).

In the next sections we present two extensions of this microscopic field-theoretical approach that have been introduced in [25, 26] and [90] to consider hydrodynamic interactions and active crystals on a sphere, respectively.

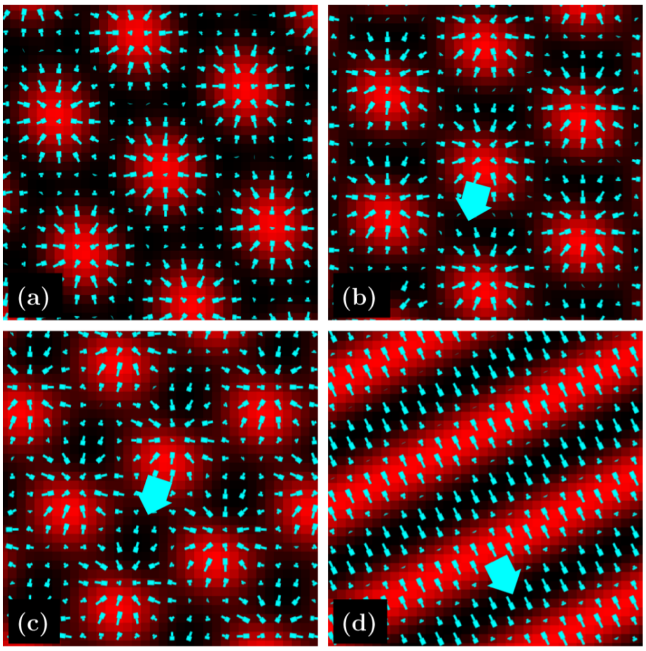

Figure 2.6: Snapshots of the density and polar order parameter coming from equation (2.13) with parameters $(\bar{\psi}, r, C_1, C_4, D_r) = (-0.4, -0.98, 0.2, 0, 0.5)$. Varying the activity different phases of the active PFC model are observed: (a) a resting hexagonal for low activity ($v_0 = 0.1$), (b) a traveling hexagonal ($v_0 = 0.5$), (c) a traveling quadratic ($v_0 = 1.0$) and (d) a traveling lamellar ($v_0 = 1.9$). The image is taken from [25].

In the next chapter we will present a modification of this microscopic field-theoretical approach where low densities are allowed. We will then study this new model in details and use it to explore the collective dynamics of active particles on large scale. In chapter 4 this microscopic field-theoretical approach will be extended to mixtures of interacting passive and active particles, allowing us to describe generic properties of such systems.

### 2.4.1 Hydrodynamic interactions

Equations (2.13) can be extended to consider particles surrounded by a fluid. To this end, hydrodynamic interactions between the particles must be taken into consideration. This is done in [25, 26] by using an approach inspired to the fluid particle dynamics (FPD) method [47], already introduced in chapter 1.

Calling $\boldsymbol{u}$ the fluid velocity, the new set of dynamical equations reads:

$$\begin{aligned}\partial_t\psi &= M_0\Delta\frac{\delta\mathcal{F}}{\delta\psi} - v_0\nabla\cdot\boldsymbol{P} - \boldsymbol{u}\cdot\nabla\psi,\\ \partial_t\boldsymbol{P} &= \Delta\frac{\delta\mathcal{F}}{\delta\boldsymbol{P}} - D_r\frac{\delta\mathcal{F}}{\delta\boldsymbol{P}} - v_0\boldsymbol{\nabla}\psi - \boldsymbol{u}\cdot\nabla\boldsymbol{P} + \boldsymbol{\Omega}\cdot\boldsymbol{P},\\ \partial_t\boldsymbol{u} + \boldsymbol{u}\cdot\nabla\boldsymbol{u} &= \boldsymbol{F} + \eta\{\psi\}\nabla\boldsymbol{u} - \alpha\boldsymbol{u},\\ \nabla\cdot\boldsymbol{u} &= 0.\end{aligned} \tag{2.16}$$

$\alpha$ is the friction constant, $\Omega$ is the vorticity tensor defined above and it describes rotations due to convection, while flow alignment of the polarization field is not considered. In [25, 26] the force term $\boldsymbol{F}$ is modeled using the discrete form given by equation (1.24). As explained when introducing the FPD method in chapter 1, the viscosity $\eta$ varies with the density $\psi$. In this case, $\eta$ is set to a certain value at the position where the density $\psi$ is the lowest and it linearly increases by a factor of $2-3$ when it goes to regions of high density $\psi$ (which correspond to particles). In [26] it is shown that hydrodynamic interactions introduced via (2.16) speed-up the collective migration speed $v_m$ and destabilize the crystalline order of the system.

This model for self-propelled particles with hydrodynamic interactions could be extended by considering the continuous approximation for the force term $\boldsymbol{F}$, equation (1.25), instead of the discrete form used here. We also observe that, unlike in the phase field active polar gel presented above, the activity strength $v_0$ does not influence directly the fluid. This is also something that should be addressed in a future work. These questions remain however open and are not addressed further in this thesis.

### 2.4.2 Active crystals on a sphere

In [90] the microscopic field-theoretical approach presented above is extended to a sphere. The resulting model is used to study crystals of self-propelled colloidal particles on a sphere and to explore the different crystalline states and the defects therein. Here, we want to show how equations (2.13) have been generalized to a sphere $\mathcal{S}$ of radius $R$. The starting point is the parametrization of the position vector $\boldsymbol{r}$ as $\boldsymbol{r}(\theta,\phi) = R\hat{\boldsymbol{u}}(\theta,\phi)$, where $\hat{\boldsymbol{u}}(\theta,\phi) = (\sin(\theta)\cos(\phi), \sin(\theta)\sin(\phi), \cos(\theta))^{\intercal}$ is the orientational unit vector with spherical coordinates $\theta\in[0,\pi]$ and $\phi\in[0,2\pi)$, as shown in figure 2.7. The polarization field $\boldsymbol{P}(\boldsymbol{r},t)$ is defined as a three-dimensional vector field tangential to $\mathcal{S}$ at $\boldsymbol{r}$:

$$\boldsymbol{P}(\boldsymbol{r},t) = P_\theta(\boldsymbol{r},t)\partial_\theta\hat{\boldsymbol{u}} + P_\phi(\boldsymbol{r},t)\partial_\phi\hat{\boldsymbol{u}}, \tag{2.17}$$

where $P_\theta(\boldsymbol{r},t)$ and $P_\phi(\boldsymbol{r},t)$ are scalar functions and $\boldsymbol{P}(\boldsymbol{r},t) \in \mathcal{T}_{\boldsymbol{r}}\mathcal{S}$, with $\mathcal{T}_{\boldsymbol{r}}\mathcal{S}$ the tangent space of the sphere $\mathcal{S}$ in the point $\boldsymbol{r}$.

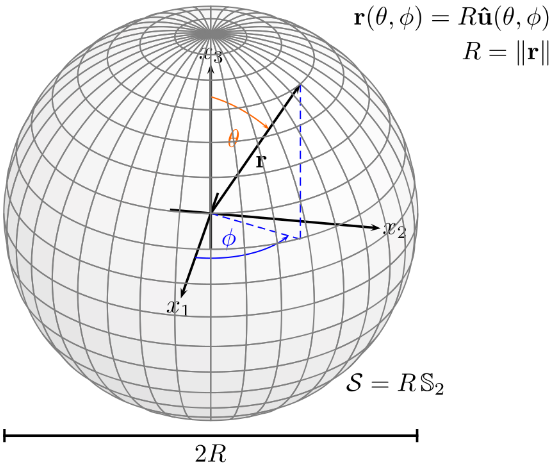

Figure 2.7: Image of a sphere $\mathcal{S}$ of radius $R$. The parametrization of the position vector $\boldsymbol{r}(\theta,\phi)$ is shown, together with the spherical coordinates $\theta$ and $\phi$. The image is taken from [90].

The energy functionals (1.4) and (2.14) are substituted with:

$$\begin{aligned} \mathcal{F}_{\text{pfc}}[\psi] &= \int_{\mathcal{S}} \left\{ \frac{\psi}{2} \left[ r + (1+\Delta_{\mathcal{S}})^2 \right] \psi + \frac{\psi^4}{4} \right\} d\boldsymbol{r}, \\ \mathcal{F}_{\boldsymbol{P}}[\boldsymbol{P}] &= \int_{\mathcal{S}} \left[ \frac{1}{2} C_1 \boldsymbol{P}^2 + \frac{1}{4} C_4 (\boldsymbol{P}^2)^2 \right] d\boldsymbol{r}, \end{aligned} \tag{2.18}$$

where the integration is now over the sphere $\mathcal{S}$, $\Delta_{\mathcal{S}} = \text{div}_{\mathcal{S}}\,\text{grad}_{\mathcal{S}}$ is the Laplace-Beltrami operator and we define the gradient and divergence operators in spherical coordinates as:

$$\begin{aligned} \text{grad}_{\mathcal{S}}\psi &= \frac{1}{R} \left[ (\partial_\theta \hat{\boldsymbol{u}}) \partial_\theta \psi + \frac{1}{\sin(\theta)^2} (\partial_\phi \hat{\boldsymbol{u}}) \partial_\phi \psi \right] \\ \text{div}_{\mathcal{S}}\boldsymbol{P} &= \frac{1}{R} [\cot(\theta) P_\theta + \partial_\theta P_\theta + \partial_\phi P_\phi]. \end{aligned} \tag{2.19}$$

The dynamics of $\psi$ and $\boldsymbol{P}$ restricted to the sphere [92, 129, 130] reads:

$$\begin{aligned} \partial_t \psi &= M_0 \Delta_{\mathcal{S}} \frac{\delta \mathcal{F}}{\delta \psi} - v_0 \text{div}_{\mathcal{S}} \boldsymbol{P} \\ \partial_t \boldsymbol{P} &= -(\Delta_{\text{dR}} + D_r) \frac{\delta \mathcal{F}}{\delta \boldsymbol{P}} - v_0 \text{grad}_{\mathcal{S}} \psi, \end{aligned} \tag{2.20}$$

where $\mathcal{F} = \mathcal{F}_{\text{pfc}} + \mathcal{F}_{\boldsymbol{P}}$, with $\mathcal{F}_{\text{pfc}}$ and $\mathcal{F}_{\boldsymbol{P}}$ given by (2.18). The Cartesian Laplace operator

$\Delta$ acting on $\delta\mathcal{F}/\delta\psi$ has been replaced with the Laplace-Beltrami operator $\Delta_{\mathcal{S}}$ defined above and the Cartesian Laplace operator acting on the vector-valued $\delta\mathcal{F}/\delta\boldsymbol{P}$ has been replaced with the surface Laplace-de Rham operator $\Delta_{\mathrm{dR}} = -\mathrm{grad}_{\mathcal{S}}\mathrm{div}_{\mathcal{S}} - \mathrm{rot}_{\mathcal{S}}\mathrm{Rot}_{\mathcal{S}}$. The surface curl operators in spherical coordinates are given by:

$$\begin{aligned}
\mathrm{rot}_{\mathcal{S}}\psi &= \frac{1}{R\sin(\theta)}[-(\partial_\theta\hat{\boldsymbol{u}})\partial_\phi\psi + (\partial_\phi\hat{\boldsymbol{u}})\partial_\theta\psi], \\
\mathrm{Rot}_{\mathcal{S}}\boldsymbol{P} &= \frac{1}{R}\left[2\cos(\theta)P_\phi - \frac{1}{\sin(\theta)}\partial_\phi P_\theta + \sin(\theta)\partial_\theta P_\phi\right].
\end{aligned} \tag{2.21}$$

The set of equations (2.20) describes the dynamics of self-propelled particles tangential to the sphere $\mathcal{S}$ and it can be seen as a minimal field-theoretical model for active crystals on a sphere. Notice that, in the limit $R \to \infty$, equations (2.20) locally reduces to the description on the plane, given by equations (2.13).

Another interesting possible extension of the connection between a microscopic field-theoretical approach and topological active matter would be the study of active nematics on surfaces [84–86]. To this end a third variable should be coupled to the system, namely the nematic order parameter given by a tensor $\boldsymbol{Q}$. While steps have been made in this direction [91], the exact coupling between the tensor $\boldsymbol{Q}$ and the PFC model remains an open question. For this reason, we studied an agent-based model to perform a preliminary study of dry active nematics on surfaces [84]. This is presented in chapter 5, together with some results about the defect dynamics.

## 2.5 Summary

In summary, in this chapter we have given an overview over the different models that have been introduced over the years to describe active matter and the observed collective phenomena that characterize this field. We started by identifying the main underlying features of active systems and by explaining the role of symmetries, medium and topological confinement. After, we described how simple agent-based models have been successfully used to numerically simulate different phenomena observed in active matter. The Vicsek model, that is considered to have started the field of active matter, has been discussed in more details. We then shifted our attention towards a more macroscopic point of view, discussing how hydrodynamic approaches can be used to shed light on the long time- and large length-scale dynamics of a very large system. In this context, we introduced the Toner-Tu model, which describes the dynamics of dry flocks, and we sketched two possible derivations of it: a phenomenological one and a microscopic one.

Further, we have shown how newly developed microscopic phase field approaches can be used to deal with deformable particles and to keep track of physical processes happening inside particles. These methods, that have proven to be particularly successful in the field of cell motility, are however very expensive from a computational point of view. Finally, we have seen that a microscopic field-theoretical approach originally developed for active crystals can be seen as a coarse-grained version of phase field descriptions. This allows to use this description to efficiently simulate a much larger number of particles than possible with phase field approaches, while at the same time still accounting for particle internal structure and, to some extent, its deformations.

# 3 A microscopic field theoretical approach for active systems

Our aim in this chapter is to extend the active PFC continuum model introduced in the previous chapter to describe active crystals [25, 26]. This has been one of the first continuum models in active matter which addressed, besides orientational ordering, also positional ordering. We propose an extension of this model to also allow for low densities. To this end we consider a variant of the PFC model, the vacancy PFC (VPFC) model, which can be used to describe individual particles. The resulting microscopic field-theoretical approach can be considered as a minimal continuum model to describe generic properties of active systems and emerging collective phenomena on a large scale. After introducing the model, we validate it by reproducing results obtained with corresponding agent-based microscopic models [15]. We consider binary collisions, collective motion and vortex formation. In the previous chapter it was mentioned that this microscopic field-theoretical approach can be seen as a coarse-grained model of the detailed phase field description given by equations (2.12). We present a comparison between these two models, which give results that are in qualitative agreement with each other.

Considering larger systems the formation of collective motion can be analyzed. For high densities we observe a coarsening process of regions of different directions of collective motion. This was already mentioned in [25], but not analyzed. In a broader context the observations can also be related to defects in active crystals. For orientational ordering this was e.g. analyzed in [131]. Another remarkable property of active systems is giant number fluctuation in a cluster formation process. In contrast to equilibrium systems, where the standard deviation $\Delta N$ in the mean number of particles $N$ scales as $\sqrt{N}$ for $N \to \infty$, in active systems $\Delta N$ can become very large and scales as $N^{\alpha}$, with $\alpha$ an exponent as large as $1$ in two dimensions. This theoretical prediction is often associated with elongated particles and a broken orientational symmetry [10, 70–72], but it has also been verified in simulations of agent-based models for disks with no-alignment rule, see [18], and was demonstrated by experiments and simulations in [132]. We use large scale simulations to show giant number fluctuations in the proposed microscopic field-theoretical approach.

## 3.1 The model

Our starting point is the active phase field crystal model derived in [25, 26], whose dynamical equations are given by equation (2.13). Inserting equation (2.14) into (2.13), making the following substitutions:

$$C_1 \to \tilde{\alpha_2}, \qquad C_4 \to \tilde{C_2}, \qquad D_r C_1 \to \tilde{\alpha_4}, \qquad D_r C_4 \to \tilde{C_4}, \tag{3.1}$$

and omitting the tilde we obtain:

$$\begin{aligned} \partial_t \psi &= M_0 \Delta \frac{\delta \mathcal{F}_{\mathrm{pfc}}}{\delta \psi} - v_0 \nabla \cdot \boldsymbol{P} \\ \partial_t \boldsymbol{P} &= \Delta \left( \alpha_2 \boldsymbol{P} + C_2 \boldsymbol{P}^3 \right) - \left( \alpha_4 \boldsymbol{P} + C_4 \boldsymbol{P}^3 \right) - v_0 \nabla \psi. \end{aligned} \tag{3.2}$$

$\mathcal{F}_{\mathrm{pfc}}$ is the dimensionless PFC energy function, equation (1.4). $\boldsymbol{P}(\boldsymbol{r}, t)$ is the polar order parameter and the remaining parameters are: $M_0$ mobility, $v_0$ self-propulsion determining the strength of the activity, $\alpha_2$ and $\alpha_4$ two parameters related to relaxation and orientation of the polarization field, and $C_2$ and $C_4$ are parameters which govern the local orientational ordering. In chapter 2 we have seen how the equation for the polar order $\boldsymbol{P}$ is related to the Toner-Tu model. This analogy has allowed us to identify regimes where orientational order is energetically favorable ($\alpha_{2,4} < 0$) or not ($\alpha_{2,4} > 0$). The model is used in [25, 26] to study crystallization in active systems and we want to extend it to allow for individual particles.

### 3.1.1 Adding vacancies

To allow for a description of individual particles, we consider the VPFC model introduced in chapter 1 [38, 40, 133]. Having now single particles we would like to have a more classical transport term for the local density field $\psi$ than the one appearing in equation (3.2). Following other, more coarse-grained models for active systems [1–3], we use a transport term with advection velocity $v_0 \boldsymbol{P}$ for the local density field $\psi$. This modification is more general and turns out to be more stable in comparison to the term used in (3.2), if considered for individual particles. A second modification ensures the polar order parameter $\boldsymbol{P}$ to be a local quantity that is different from zero only inside the particles. This allows us to interpret $\boldsymbol{P}$ in the context of cells as a coarse-grained orientation of actin filaments, similar to [23, 24]. The new set of dynamical equations we obtain is:

$$\begin{aligned}
\partial_t \psi &= M_0 \Delta \frac{\delta \mathcal{F}_{\text{vpfc}}}{\delta \psi} - v_0 \nabla \cdot (\psi \boldsymbol{P}) \\
\partial_t \boldsymbol{P} &= \Delta \left( \alpha_2 \boldsymbol{P} + C_2 \boldsymbol{P}^3 \right) - \left( \alpha_4 \boldsymbol{P} + C_4 \boldsymbol{P}^3 \right) - v_0 \nabla \psi - \beta \boldsymbol{P} \mathbb{1}_{\psi \leq 0},
\end{aligned} \tag{3.3}$$

with $\mathcal{F}_{\text{vpfc}}$ given by equation (1.11) and $\beta$ a parameter, which is typically larger than the other terms entering the $\boldsymbol{P}$ equation. The set of equations (3.3) describes the model that we call “active vacancy phase field crystal” (active VPFC) . The rest of this chapter is devoted to show how this set of equations can be used to describe active particles.

### 3.1.2 Computational details

We consider a sequential finite element approach to solve the evolution equations (3.3). An operator splitting approach is used, where the equation for $\boldsymbol{\psi}$ is discretized according to [134] and the equation for $\mathbf{P}$ using a semi-implicit Euler-scheme with all nonlinear terms linearized around the value of the last time step. Elements of polynomial degree one are used. The resulting linear systems are solved using a direct solver UMFPACK [135]. See also the section at the end of chapter 1 for more details on the finite element implementation within the AMDiS framework [56, 57].

The maxima in the local one-particle density field $\psi$ are always tracked for post-processing and evaluation, and every maximum is interpreted as a particle (see [42] for a discussion about the validity of this interpretation). The morphology of the particle is obtained from a contour line of the density field, see below for details, and its velocity is computed as the discrete time derivative of two successive maxima. The computational domain varies for the different examples and is specified below. The initial condition for $\psi$ is given by the sum of the local density peaks, formula (1.14), with the center placed either randomly or in a given position, see [40] for more details. Only for high densities a perturbation from a hexagonal ordered state is chosen as initial condition. The $\boldsymbol{P}$ field is set to zero initially, unless otherwise stated.

## 3.2 Model Validation

The aim of this section is to show that the microscopic field-theoretical model equation (3.3) can be used to simulate active particles and allows the recovery of known phenomena. The versatility of the model thereby allows us to apply it to different physical situations that have been previously studied using agent-based models, see e.g. [15]. We first consider the situation of one particle, followed by studying the interaction of two particles. These simple computations allow for detailed parameter studies. We found no qualitative difference in the results of our simulations when the parameters $C_2$ and $C_4$ are set to zero. Therefore we simplify our model by restricting ourselves to the case $C_2 = C_4 = 0$, which allows only gradients in the density field $\psi$ to induce local polar order[1]. $M_0$ and $v_0$ will be specified for each simulation. The other parameters are $(\alpha_2, \alpha_4, \beta, H, r) = (0.2, 0.1, 2, 1500, -0.9)$, unless otherwise specified in the figure captions. After having shown the results for these simple systems, we shift our attention to collective migration and other collective phenomena. We fix the number of particles $N \simeq 100$ and show the emergence of collective migration in a system with periodic boundary conditions. The emergence of other collective phenomena, such as vortex formation and oscillatory motion, in confined geometries is shown as well.

### 3.2.1 Onset of movement and particle shape

We at first want to understand what happens in a minimal system, where a single active particle is free to move. In particular, since we are in a regime where orientational order is not energetically favorable ($\alpha_{2,4} > 0$), we are interested to know if there is a critical value for the activity $v_0$ required for the onset of movement, as it has been observed in [25] for active crystals and shown in figure 2.5.

In figure 3.1(a) the particle velocity is plotted as a function of the activity $v_0$ and we can see that for small activities ($v_0 < 0.5$) the particle does not move at all. After a certain threshold value $v_{0,t} \simeq 0.5$ the particle starts to move with a constant velocity, which approximately linearly increases for increasing $v_0$. This is exactly the same behavior observed in figure 2.5 (blue dots) for the collective migration speed $v_m$ of the active crystals [25, 26].

An important new feature of our model has to do with the mobility term $M_0$ entering

---

[1] In this case thermodynamic stability dictates $\alpha_2 > 0$ and $\alpha_4 > 0$, as discussed in chapter 2.

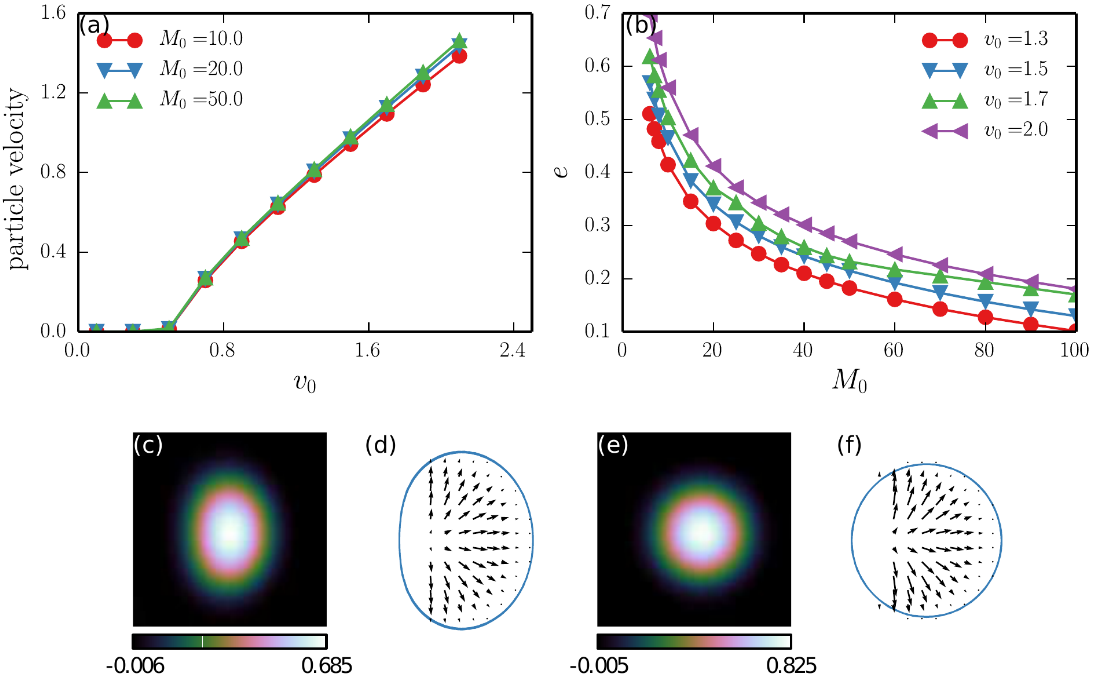

Figure 3.1: (a) Velocity of a particle as a function of the activity strength $v_0$ for different values of the mobility $M_0$. At a threshold value $v_{0,t} \simeq 0.5$ the particle starts to move. (b) Eccentricity $e$ of a single particle as a function of mobility. The eccentricity is defined as $e = \sqrt{1 - b^2/a^2}$ where $a, b$ are the length of the semi-major and semi-minor axis, respectively. For small values of $M_0$ the particles have the form of an elongated ellipse (c), (d) ($v_0 = 2, M_0 = 7$), whereas for larger $M_0$ their form is similar to a circle (e), (f) ($v_0 = 2, M_0 = 100$). (c) and (e) show the contour plot of $\psi$ and (d) and (f) the morphology of the particle identified by the contour line of an intermediate value of $\psi$ between $0.001$ and $0.01$, together with the $\boldsymbol{P}$ field.

equation (3.3). $M_0 = 1$ is used in [25]. This value would lead to strong numerical instabilities when using the modified model equation (3.3). Larger values for $M_0$ can suppress this numerical instability. While the mobility does not particularly change the particle velocity, we observe that $M_0$ directly influences the shape of the particle: for small (but still greater than 1) $M_0$ the particle shows an elliptic form, whereas further increasing $M_0$ restores a circular shape for the particle, see figure 3.1(b). The dependency of the particle shape on the value of $M_0$ is shown in figure 3.1(b) for different values of $v_0$ above the threshold value. Two examples of the morphology are shown in figures 3.1(c-f) together with the $\boldsymbol{P}$ field.

Similar results can be obtained using the (mathematically more complicated) dry microscopic phase field model [23, 24] given by equations (2.12). In figure 3.2(a) we see that an activity threshold is present also in this model. For small values of $v_0$ the particle (or, more precisely, the cell) does not move. Above the threshold value, the cell velocity increases approximately linearly with the activity strength, as in figure 3.1(a). However, in figure 3.2(a) the threshold value $v_{0,t}$ and the cell velocity are both significantly smaller than for the active VPFC model. Finally, notice that in figure 3.2(a) the parameter $c_1$ is negative. This is necessary to obtain an activity threshold value for the cell velocity. Setting $c_1 > 0$, no threshold value is observed anymore and the cell velocity increases approximately linearly with $v_0$ (data not shown), similarly to [26] for the active PFC model, see also figure 2.5.

A phase field model can easily handle particle deformations. In fact, increasing the strength of the surface tension effects, i.e. decreasing the parameter $Ca$ in equations (2.12), the cell shape changes from elliptical (figure 3.2(b),(c)) to spherical (panel (d),(e)). This resembles the behavior observed in figure 3.1(c-f), which was obtained by changing the mobility $M_0$ in equations (3.3).

This suggests that a comparison between the phase field active polar gel model and the active VPFC model could help to shed some light on the physical meaning of the latter, equations (3.3). However, this requires a more detailed comparison between the two models than the one presented here and it remains as an open question.

### 3.2.2 Binary collisions and elastic deformation

The study of binary collisions between particles is often used as a benchmark problem to predict how larger systems evolve, see e.g. [23, 79]. In particular, it has been observed

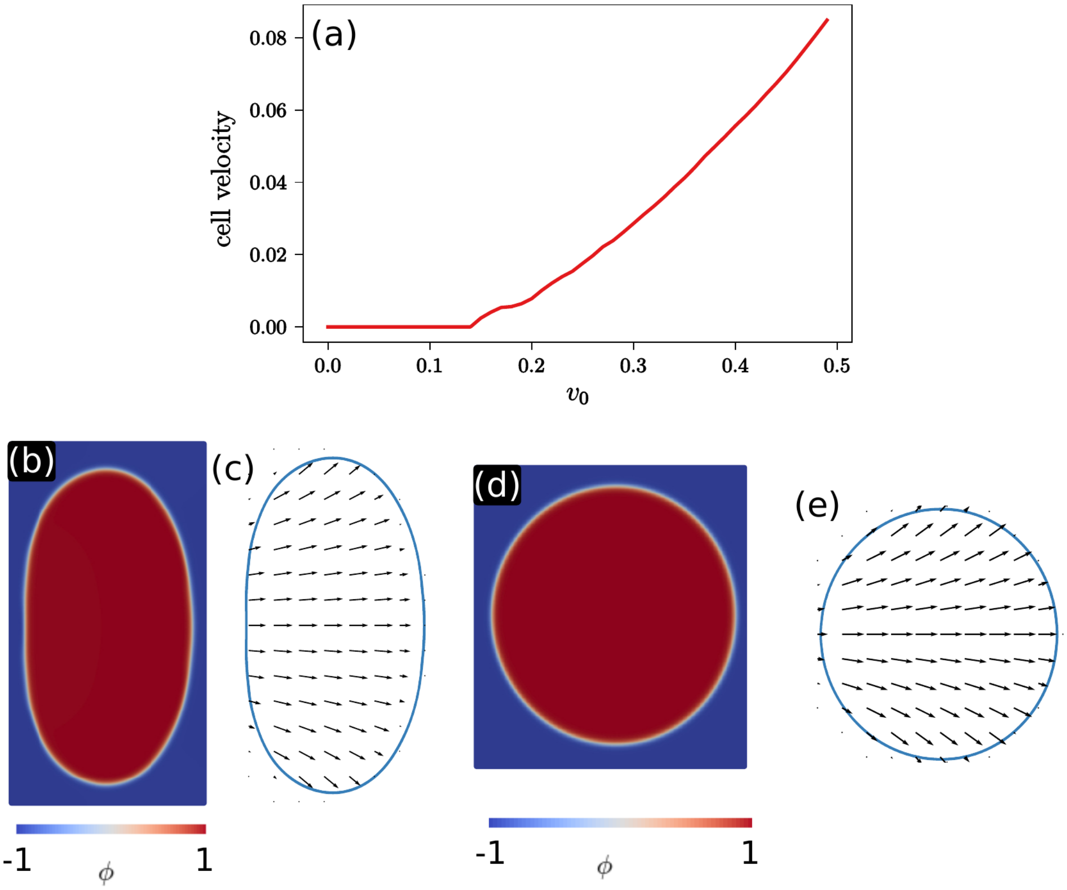

Figure 3.2: (a) Cell velocity as a function of the activity strength $v_0$ for the dry microscopic phase field model. Also in this case we observe a threshold value $v_{0,t}$, however the cell velocity and $v_{0,t}$ are both much smaller than in figure 3.1. The parameters are $(Ca, Pa, \gamma, \epsilon, c_1, c_4, \kappa, In, v_1, \beta_1, \beta_2) = (0.05, 10, 1, 0.2, -10, 10, 1, 0, 0, 0, 0.01)$. (b), (c) For $Ca = 0.01$ the cell shows an elliptic shape, while decreasing $Ca = 0.001$ the shape becomes circular (d),(e). (b) and (d) shows the contour plot of the phase field $\phi$, (c) and (e) the morphology of the cell identified by the contour line of an intermediate value of $\phi$ between $-0.4$ and $0.4$, together with the $\boldsymbol{P}$ field. (b)-(e) Other parameters are $(Pa, \gamma, \epsilon, c_1, c_4, \kappa, In, v_0, v_1, \beta_1, \beta_2) = (10, 1, 0.2, 10, 10, 1, 0, 1, 0, 0.5, 0.5)$. The data for this figure have been produced from Dennis Wenzel solving equations (2.12).

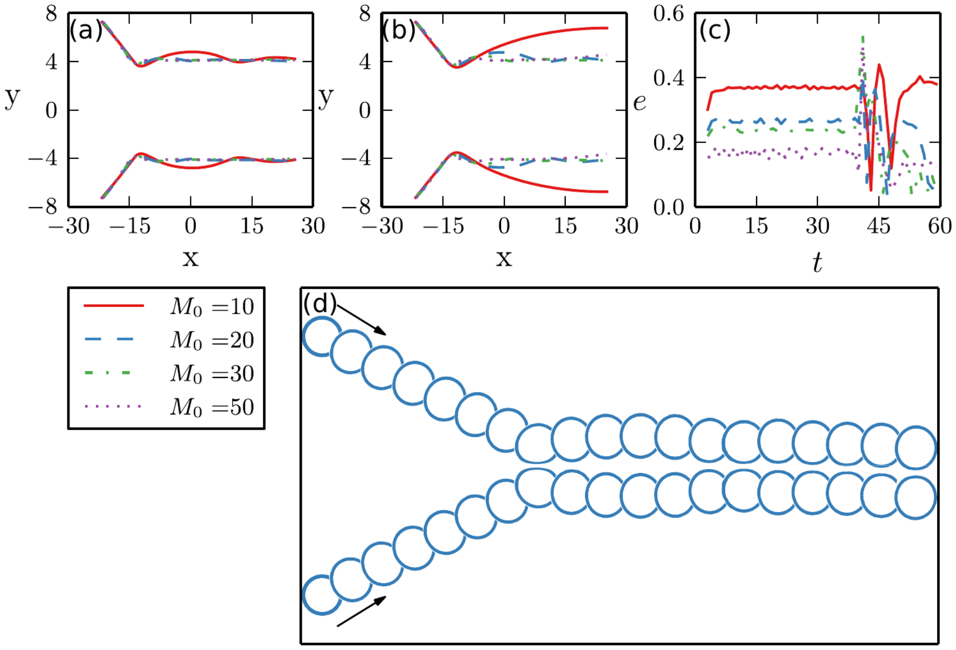

Figure 3.3: (a)-(b) Two particles colliding in a perfectly symmetric way for (a) $v_0 = 1.5$ and (b) $v_0 = 2.5$. The net effect of the collision is an alignment of the particles direction. (c)Eccentricity of a particle as a function of time during a collision for $v_0 = 1.5$ and different mobility values. We observe a sudden change in the particle eccentricity at $t \simeq 40$, corresponding to the collision time. (d) Time series of a two-particle collision for $v_0 = 1.5$ and $M_0 = 10$. Notice how the form of the particles is slightly changed during the collision. The shape of the particles is identified as a fixed contour line of $\psi$.

that completely inelastic collisions lead to a force that aligns the particles direction [15]. We here consider only perfectly symmetric collisions meaning that the incidence angle and the initial velocity are the same for both particles. This is achieved by setting the norm of the $\boldsymbol{P}$ field at time $t = 0$ equal to one inside the two particles and zero outside, whereas the black arrows in figure 3.3(d) show its direction. Different particle trajectories obtained using different mobility $M_0$ and activity $v_0$ are shown in figures 3.3(a) and (b). The elastic deformation of a single particle during a collision can be seen in figure 3.3(c), where the eccentricity is plotted as a function of time, whereas a time series of a single collision is shown in figure 3.3(d). Collisions of deformable particles have also been considered in agent-based models [16], with a qualitatively similar behavior. However, the deformations in our approach strongly depend on $M_0$ and are negligible for large values. We therefore do not analyze this effect further and interpret the particles as being spherical in the coming simulations, which are all done for large $M_0$.

All results indicate the particle alignment to be not instantaneous. There is an initial

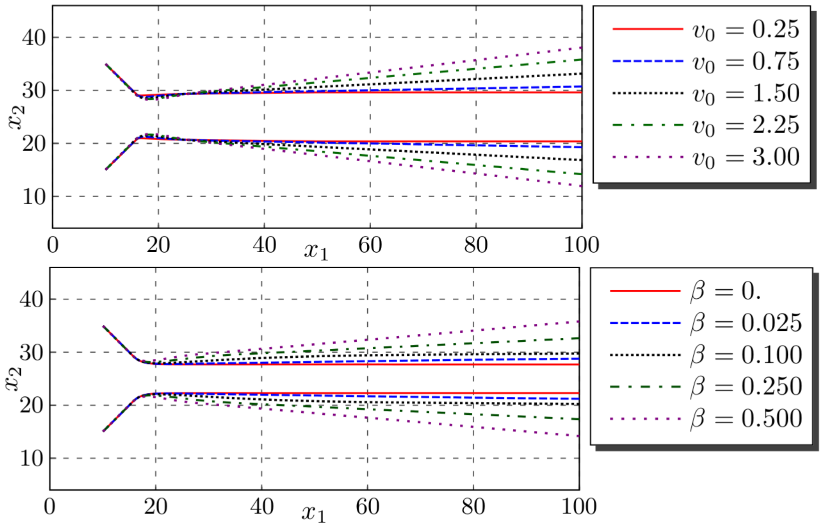

Figure 3.4: Cell trajectories for the dry microscopic phase field model. The parameters are $(Ca, Pa, \gamma, \epsilon, c_1, c_4, \kappa, In) = (0.0281, 0.1, 1, 0.2, 10, 10, 1, 0.1125)$ and $\beta = \beta_1 = \beta_2 = 0.5$ (top) and $v_0 = v_1 = 2.25$ (bottom). For $\beta = 0$ we have perfectly inelastic collision and the collisions become slightly more elastic as $\beta$ or $v_0$ are increased. The image is taken from [121].

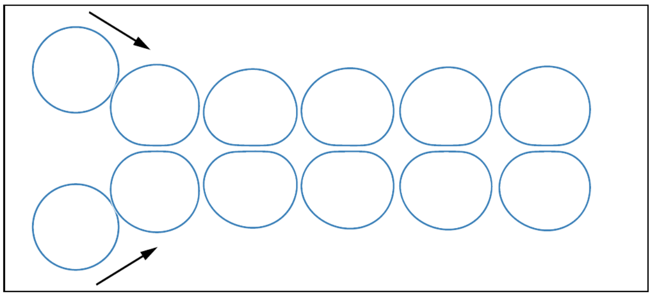

Figure 3.5: Time series of a collision between two cells. Shown are the cell shapes and the orientation fields. The parameters are $(Ca, Pa, \gamma, \epsilon, c_1, c_4, \kappa, In, v_0, v_1, \beta_1, \beta_2) = (0.01, 1, 1, 0.2, 10, 10, 1, 1, 2.25, 0, 0, 0.01)$ The data for this figure have been produced from Dennis Wenzel solving equations (2.12).

oscillatory phase, whose length and magnitude depends on $M_0$ and $v_0$. Small activity and large mobility lead to an almost instantaneous alignment, whereas large activity and small mobility lead to oscillations for a certain period of time, before the particles finally align and travel together.

Also in this case, a comparison with the dry microscopic phase field model can be made. A time series of a single collision event is shown in figure 3.5. The alignment between the cells is instantaneous, in agreement with the results from figure 3.3 for small activity $v_0$ and large mobility $M_0$. In figure 3.4 cell trajectories of a binary collision event are shown for different parameters. All collisions are strongly inelastic and there is an almost instantaneous alignment. Increasing $\beta_{1,2}$ or $v_{0,1}$ the collisions become slightly more elastic and the qualitative agreement with the active VPFC model is partially lost.

### 3.2.3 Collective motion in confined geometries

As already analyzed using agent-based [15, 16] and phase field models [23, 24] the interaction of a moderate number of particles can lead to collective motion. We here consider simulations with $N \simeq 100$ particles to recover these results. To analyze the phenomena we define the translational order parameter $\phi_T$ and the rotational order parameter $\phi_R$ as

$$\phi_T(t) = \frac{1}{N}\left|\sum_{i=1}^{N} \hat{\boldsymbol{v}}_i(t)\right|, \qquad \phi_R(t) = \frac{1}{N}\sum_{i=1}^{N} \hat{\boldsymbol{e}}_{\theta_i(t)} \cdot \hat{\boldsymbol{v}}_i(t), \tag{3.4}$$

where $\hat{\boldsymbol{v}}_i(t)$ is the unit velocity vector of particle $i$ at time $t$, $\hat{\boldsymbol{e}}_{\theta_i(t)} = (-\sin(\theta_i(t)), \cos(\theta_i(t)))$ is the unit angular direction vector of particle $i$ at time $t$, and $N$ is the number of particles. In case of collective migration we obtain $\phi_T = 1$ and rotational migration (i.e. particles forming a vortex) leads to $\phi_R = \pm 1$.

#### Collective migration

We consider a square domain with periodic boundary conditions, i.e. simulating an infinite plane where particles are free to move without obstacles. Figure 3.6 shows the resulting behavior. At the beginning (figure 3.6(a)) there is no specific order and particles move towards different directions. After the first collisions take place some particles start to align with each other and small blocks of particles, in which particles orient in the same direction are formed (figure 3.6(b)). If these blocks collide they change their

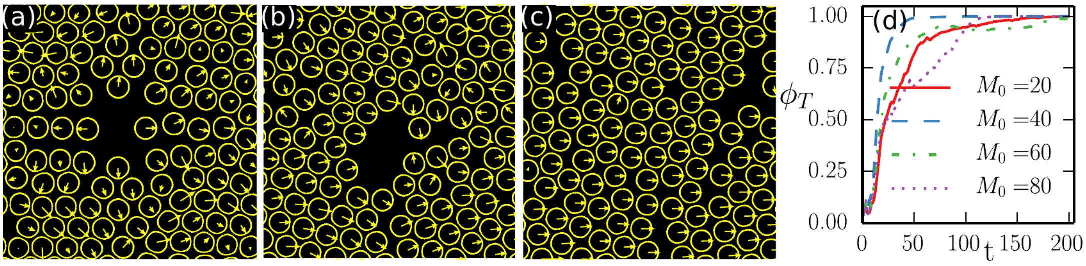

Figure 3.6: (a)-(c) Snapshots of a single simulation of $N \simeq 100$ active particles in a square with periodic boundary conditions for $v_0 = 1.5$ and $M_0 = 50$. After an initial chaotic phase particles travel together in the same direction. (d) Translational order parameter $\phi_T$ for different values of $M_0$: mobility does not seem to affect the emergence of collective migration. Each curve has been obtained as the average of 10 different simulations started with different initial conditions and $v_0 = 1.5$.

direction until all the particles in the system are traveling in the same direction (figure 3.6(c)). This behavior is further confirmed by the translational order parameter $\phi_T \simeq 1$ after a certain time, see figure 3.6(d). We also observe that this migration state is not particularly affected by the value of the mobility $M_0$.

In figure 3.7 we show snapshots for the simulation of $N \simeq 600$ particles obtained using the dry phase field active polar gel model on a square domain with periodic boundary conditions. The volume fraction (i.e. the ratio between the surface occupied by the particles and the total surface, formally defined below) is lower than in figure 3.6, but collective migration is observed also in this case. At time $t = 0$ the particles are randomly distributed and the orientation $\boldsymbol{P}_i$ is set to a normalized random vector assuming a constant value inside cell $i$ and zero outside. Different cell colors correspond to different orientations. At the beginning (figure 3.7(a)) cells are oriented in random direction. Some order starts to emerge as time passes (figure 3.7(b),(c)), until we find all cells moving collectively in the same direction (figure 3.7(d)). This is in qualitative agreement with the results obtained using the active VPFC model, as confirmed by a translational order parameter $\phi_T \simeq 1$ after a certain transient time. In figure 3.8 we also see that the behavior of $\phi_T$ over time is similar for the active VPFC and the dry phase field models. This is not always the case: for both models, different parameters lead to a different duration of the transient phase. However, collective migration is observed in both cases, meaning that the translational order parameter $\phi_T \to 1$ asymptotically over time for both models.

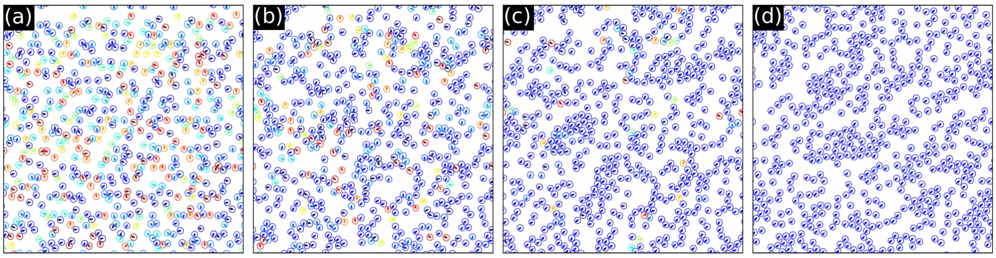

Figure 3.7: Snapshots showing the emergence of collective motion for the dry phase field active polar gel model introduced in chapter 2. They correspond to time: (a) $t = 7$, (b) $t = 25$, (c) $t = 50$, (d) $t = 200$. The cell shapes and the cell average orientations are shown. The color code corresponds to the orientations of the particles. The parameters are $(Ca, Pa, \gamma, \epsilon, c_1, c_4, \kappa, In, v_0, v_1, \beta_1, \beta_2) = (0.025, 1, 1, 0.15, 10, 10, 1, 0.05, 2.5, 2.5, 0.01, 0.01)$. Figures and simulations from Simon Praetorius, based on [90].

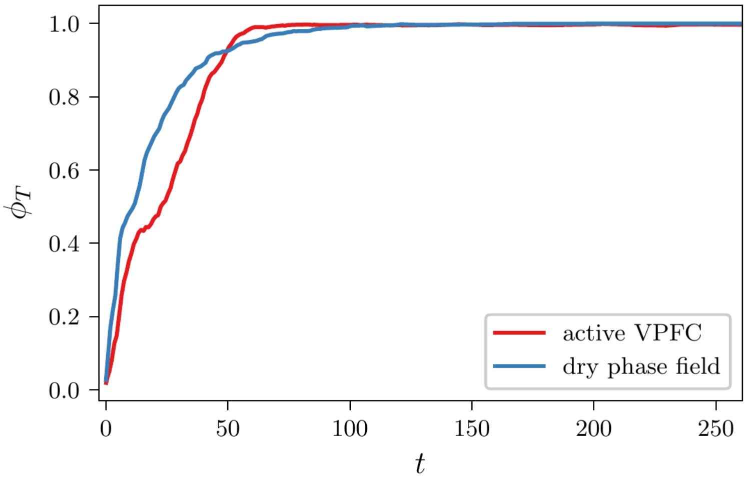

Figure 3.8: Translational order parameter $\phi_T$ as a function of time for the active VPFC model (red curve) and the dry phase field active polar gel model introduced in chapter 2 (blue curve). $M_0 = 100$ and $v_0 = 1.5$ for the red curve, whereas the parameters for the blue curve are as in figure 3.7. Both curves show a similar behavior over time; this is a consequence of the parameters used for the two models. More importantly, $\phi_T \to 1$ asymptotically over time, meaning that collective migration is present in both models. The data for the blue curve have been provided by Simon Praetorius and published in [90].

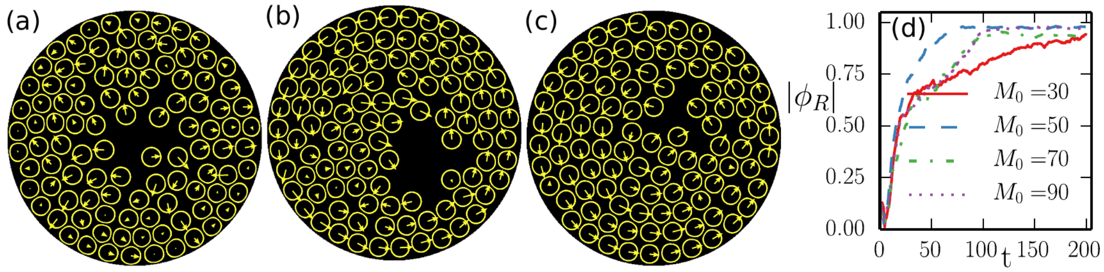

Figure 3.9: (a)-(c) Snapshots of a vortex formation by active particles confined in a disk for $v_0 = 1.5$ and $M_0 = 60$. (d) The rotational order parameter $|\phi_R|$ shows that after a transient phase the particles follow a circular motion for different values of $M_0$. Also in this case each curve has been obtained as the average of 10 different simulations started with different initial conditions and $v_0 = 1.5$.

### Vortex formation and oscillatory motion

We now consider a confined geometry and specify $\psi = 0$ and $\boldsymbol{P} = 0$ at the boundary, which serve as an approximation for reflecting boundary conditions. The first geometry is a disk. Here, again, at the beginning the particles move in a chaotic way, see figure 3.9(a). Then a vortex is formed and most of the particles follow an anticlockwise trajectory. In the center some particles move in the opposite direction, see figure 3.9(b). Eventually also these particles are forced to align with the rest of the system, see figure 3.9(c). This behavior is confirmed by the rotational order parameter $\phi_R$. If clockwise or anticlockwise rotation is observed depends on the initial condition, we therefore plot $|\phi_R|$ instead of $\phi_R$ in figure 3.9(d). Similarly to the collective migration case studied above, the mobility $M_0$ does not play a major role in the formation of the vortex.

Ellipses provide a more interesting geometry and confining active particles inside them can give rise to different kind of collective phenomena, where the ellipse aspect ratio $A/B$, where $A, B$ are the length of the semi-major and semi-minor axis, respectively, plays an important role. An ellipse with a small $A/B \leq 3$ shows a similar behavior as the disc shape. Such geometries produce once again a vortex, where the particles move along the boundaries. More elongated shapes with $A/B = 10$ dramatically change the behavior. As already shown in [15] particles move collectively along the major axis with oscillating direction. The same behavior could be observed with our model, see figure 3.10. All particles move in one direction until they hit the high curvature region. This produces an impulse that propagates fast along the whole system and reverts the direction of the particles. The whole process repeats every time a boundary is reached and an oscillatory motion is the result. To obtain this result and ensure a constant particle

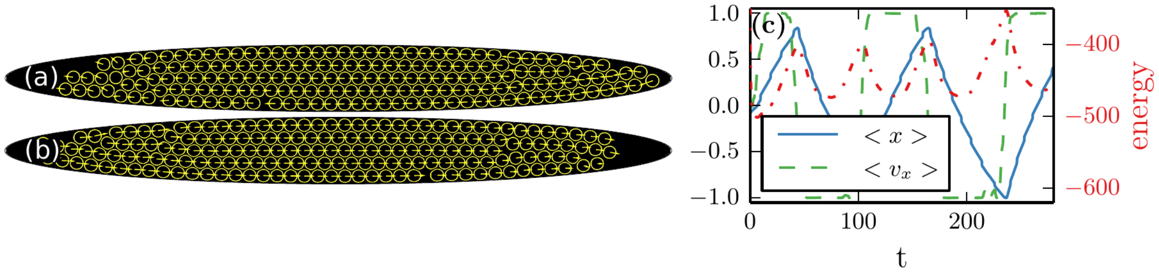

Figure 3.10: (a)-(b) Snapshots of two different moments of the collective travel of active particles inside an elongated ellipse with $A/B = 10$. Particles move together along the major axis and change orientation when they reach a boundary. (c) There is an oscillating behavior along the $x$ direction. Shown are the scaled mean position and scaled mean velocity over time together with the computed energy $\mathcal{F}_{\text{pfc}}$. Other simulation parameters are $(v_0, M_0) = (1.5, 500)$

number it is necessary to use a particularly high value for the mobility, $M_0 = 500$. Figure 3.10(c) shows the scaled mean position and mean velocity of the particles together with the computed energy $\mathcal{F}_{\text{pfc}}$. Maxima in the energy thereby correspond to turning point of direction, whereas minima are associated with situations, where the mean particle velocity is constant. If the particles hit the high curvature region the particles get jammed, which results in an increase in $\mathcal{F}_{\text{pfc}}$, resampling the elastic effects. After a certain energy value is reached an energy barrier can be overcome and the system starts to relax by moving in the opposite direction.

It would be interesting to reproduce these results about active particles on confined geometries using the dry microscopic phase field model as well. To this end, this model must be extended to account for reflecting boundary conditions and this has not been done yet.

### Validation and numerical issues

These examples demonstrate the validity of our continuous modeling approach. All known qualitative properties which have been shown using agent-based simulations could be reproduced. Until now a sequential finite element approach has been used to solve the evolution equation. For larger systems we must work in a parallel environment with multiple processors. We adopt a block-Jacobi preconditioner [48, 136] that allows us to use a direct solver locally. The approach is implemented again in AMDiS [56, 57] (see chapter 1) and shows good scaling properties, which allows to consider systems with $\simeq 15,000$ particles on the available hardware.

## 3.3 Results

We again consider a system with periodic boundary conditions for which collective migration and cluster formation is expected also for larger numbers of particles. However, how the collective migration state is reached is not well understood and will be analyzed in detail. We start with a system with high volume fraction. The volume fraction is defined as $\phi = N\sigma/|\Omega|$, with number of particles $N$, domain size $|\Omega|$ and $\sigma$ the area occupied by a single particle, which is equal to $\sigma = \pi(d/2)^2$, with $d = 4\pi/\sqrt{3}$ the lattice distance determined by the free energy equation (1.4). For $\phi > 0.6$ the system shows behavior of active crystals. Figure 3.11(a) shows various snapshots of the evolution with regions of particles moving in the same direction color coded. The regions can be identified as active grains, which undergo a coarsening process. The black particles determine orientational defects. They are identified as particles where the change in orientation from one particle to its neighbors is above a certain threshold. The number of black particles certainly depends on the threshold value, however its decrease is independent on the value. The data is not sufficient to identify a scaling law. However, the robustness of the coarsening process is shown in figure 3.11(b).

If we decrease the volume fraction the behavior changes. For very low density, $\phi = 0.03$, figure 3.12(a) shows the tendency of the particles to group together, but the formed clusters are very small and there remain many single particle in the system. Increasing the density, $\phi = 0.12$, increases the size of the formed clusters, but the average size of a cluster remains very small if compared to the total number of particles, see figure 3.12(b). Further increasing the density, $\phi = 0.25$, leads to the formation of large mobile clusters and a drastic reduction of the number of particles which do not belong to any cluster, see figure 3.12(c). This behavior is similar to the results in [78] for (quasi-) two-dimensional colloidal suspensions of self-propelled particles. For these systems we compute the standard deviation $\Delta N$ as a function of the mean number of particles $N$. For active systems it is theoretically predicted that $\Delta N$ scale as $N^\alpha$, with $0.5 < \alpha \leq 1$ and giant number fluctuations occur if $\alpha \approx 1$, see [8].

We compute $\alpha$ by considering different subregions of our computational domain[2]. The results for $\simeq 600$ particles are shown in figure 3.13, demonstrating an increase of $\alpha$ with increasing $\phi$, with the largest value reached being $\alpha = 0.79$. This continuous increase in $\alpha$, as well as the obtained values are consistent with the behavior found in [18] for

---

[2] According to [137] we are actually calculating apparent giant fluctuations.

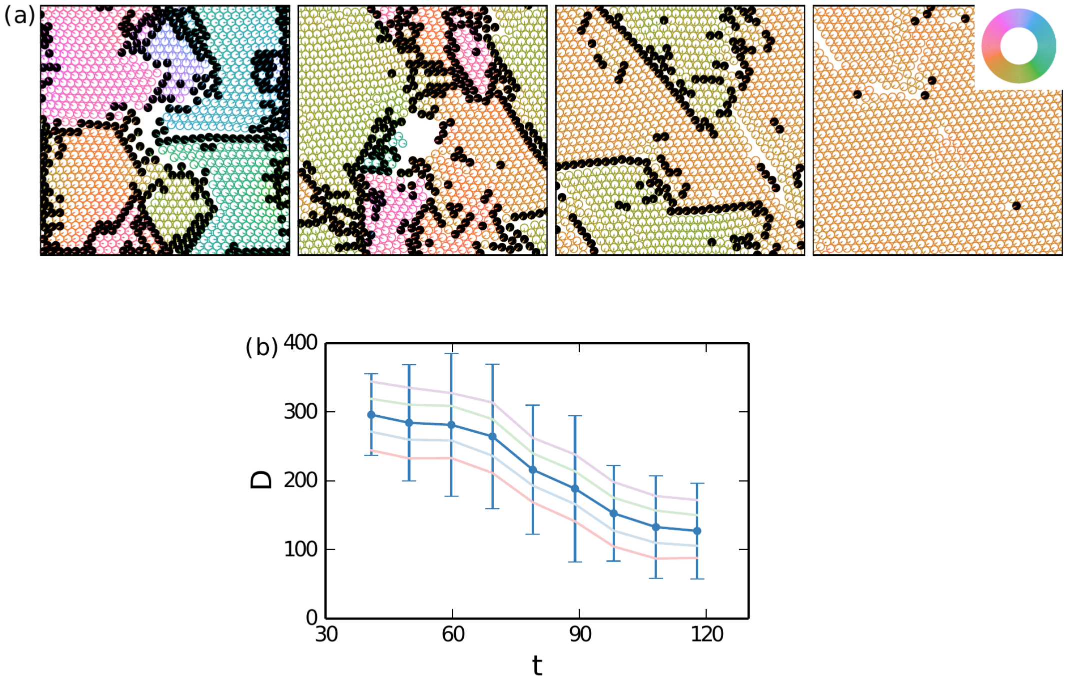

Figure 3.11: (a) Snapshots of $\simeq 1,000$ particles inside a square with periodic boundary conditions. Different colors correspond to different orientations, particles colored in black are those where there is a change in the orientation. (b) Decrease of the number of orientational defects $D$ as a function of time. Average and standard deviation of the data for six different simulations started with different initial conditions and a tolerance parameter equal to $\pi/10$ are shown in blue. Each of the shaded curves has been obtained as the average of the six simulations, but using different values for the tolerance parameter, $\pi/8$, $\pi/9$, $\pi/10$, $\pi/11$ and $\pi/12$ from top to bottom. Simulation parameters are $(v_0, M_0) = (2, 60)$

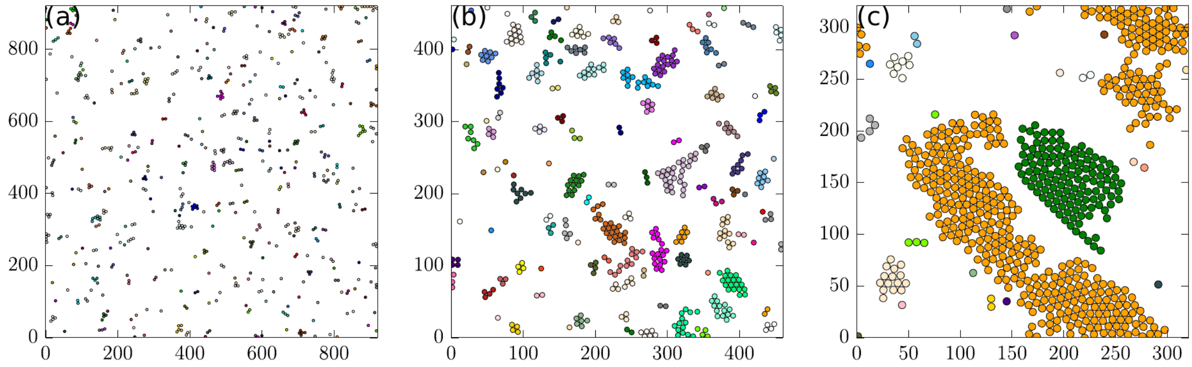

Figure 3.12: Snapshots of systems having different particle density $\phi$. Particles with the same color belong to the same cluster. (a) For $\phi = 0.03$ no cluster is present. (b) $\phi$ is increased until 0.12 and some bigger clusters appear. (c) We clearly observe two big clusters when $\phi = 0.25$. Other simulation parameters are $(v_0, M_0) = (1.5, 50)$

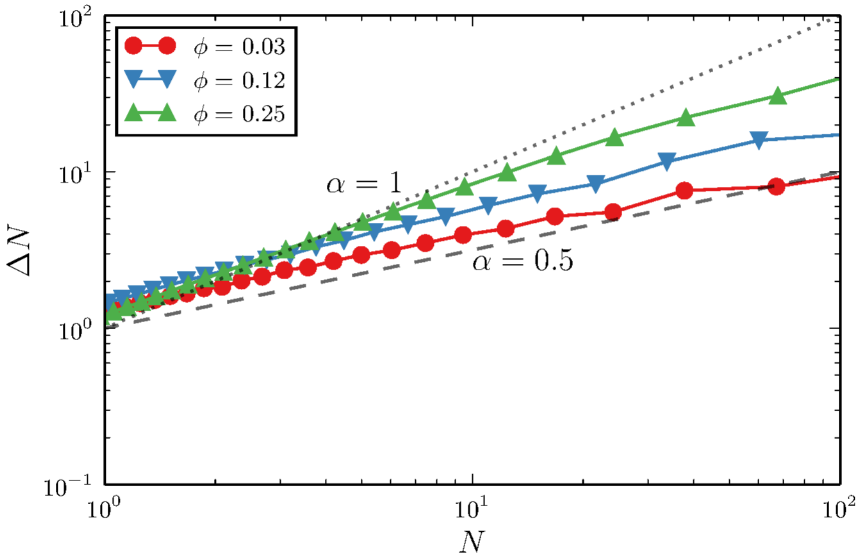

Figure 3.13: Number fluctuations for the three different values of $\phi$ shown in figure 3.12. The dashed and dotted line correspond to the case $\alpha = 0.5$ and $\alpha = 1$, respectively.

moderate numbers of particles but larger volume fractions. However, there is a significant difference, the formed clusters in [18] are stationary, our clusters are mobile, similar to the light activated living crystals in [132]. The experimental results as well as the simulations in [132] lead to similar values of $\alpha$ as ours already for smaller $\phi$.

## 3.4 Summary

In summary, we extended the phase field crystal model for active crystals [25, 26], which combines the classical phase field crystal model of Elder et al. [27, 28] with a polar order parameter, based on a simplified Toner-Tu model, and a self-propulsion velocity, by considering individual active particles. This can be realized by penalizing a locally vanishing one-particle density, as considered in [38]. The resulting microscopic field-theoretical model has been validated against known results obtained with minimal agent-based models [15]. We found a threshold value for the activity, necessary to induce motion for a particle. Collective motion and vortex formations have been identified, as well as oscillatory motion, depending on the considered confinement. All these results are in agreement with the results in [15]. We have further shown that using a dry phase field approach, equations (2.12) [23, 24], many of these results, such as the presence of an activity threshold for particle motion, alignment between particles during binary collisions and collective migration, could be reproduced. For larger systems we analyzed the formation of a traveling crystal if prepared from an initially disordered state. The traveling crystals emerge through a coarsening process from a multidomain texture of domains traveling collectively in different directions. For lower volume fractions we could identify giant number fluctuations. As theoretically predicted the standard deviation $\Delta N$ scales as $N^{\alpha}$ for active systems. The computed exponent $\alpha$ as a function of volume fraction is in agreement with experimental and simulation results obtained for light activated colloidal particles [132].

The proposed microscopic field-theoretical model can be extended from two to three spatial dimensions. Another possible extension is the inclusion of hydrodynamic interactions, using system (2.16) as a starting point [26, 40]. In [44–46] hydrodynamic interactions within the phase field crystal model for passive systems are also considered. An extension to binary mixtures [138] is considered in chapter 4. Other variants of the phase field crystal model have also been used to simulate the dynamics of epithelial cell colonies [139]. Together with efficient numerical algorithms [48] this provides the possibility to study emerging macroscopic phenomena in active systems with microscopic details, e.g. to validate coarse-grained approaches, as considered in [140, 141].

# 4 Binary mixtures of interacting active and passive particles

In the previous chapter we have shown a model that describes a system composed of interacting active particles. Even more interesting are mixtures of active and passive particles. Situations of active particles in crowded environments or passive particles in an active bath resemble the situation in living matter more realistically and might even shed light on the active dynamic processes within a cell [142]. Observed phenomena in mixtures of active and passive particles are e.g. activity-induced phase-separation [143], the formation of large defect-free crystalline domains [144], propagating interfaces [145], laning states [146] but also a transition from diffusive to subdiffusive dynamics [147, 148] and suppressed collective motion [149]. To understand this wide span of phenomena is crucial to almost all applications of active systems.

In this chapter we want to extend the microscopic field-theoretical approach introduced in chapter 3 to mixtures of active and passive particles in order to describe generic properties of such heterogeneous systems within a continuum framework. We first introduce the model, which is based on the binary PFC [34, 39, 42]. We validate the approach by reproducing experimental results, as well as results obtained with agent-based simulations. The approach is valid for the whole spectrum from highly dilute suspensions of passive particles and interacting active particles in a dense background of passive particles. However, we concentrate only on the extreme cases, as for the situation with similar fractions of active and passive particles emerging structures are hard to analyze and experimental results are missing. We perform a preliminary study of binary collisions between active and passive particles, which provide useful predictions to understand how larger systems may evolve. We then use the model to study the effect of a few active particles in passive systems (active doping) [144, 150, 151], how passive particles perturb collective migration in an active bath [147, 152–154] and in an intermediate regime the formation of lanes of active particles which move in opposite direction [5, 16, 146, 155]. For the first case we observe enhanced crystallization in the passive system, in qualitative agreement with the results of [144]. For the active bath case we investigate how collective migration is affected by a disordered environment. For the special case of immobile passive particles these results are in agreement with [148, 149]. However, for mobile passive particles new phenomena and patterns emerge, which ask for experimental validation. In the intermediate regime of similar fractions of active and passive particles a laning state is found, which is characterized by an alignment that is globally nematic, but polar within each lane. This is in qualitative agreement with [146]. However, here it is also observed for spherical-like particles. Finally, we show how this model can be extended to consider two active species or several passive species of different sizes interacting with an active species.

## 4.1 Modeling binary mixtures of active and passive particles

The starting point for the derivation of the model is the microscopic field-theoretical model for active particles introduced in chapter 3 given by the set of equations (3.3). We have to extend this model to include passive particles as well. To this end we use the binary PFC model used to describe binary mixtures introduced in chapter 1. The approach that we have chosen consists in considering energies for two species - species $A$ and species $B$ - plus a purely repulsive interaction energy, as given by equations (1.16) and (1.17). The densities of both species ($\psi_A$ and $\psi_B$) evolve according to the usual conservative equation of motion (1.18).

In principle both species appearing in (1.16) could be made active. Our aim is however to simulate mixtures of interacting active and passive particles. With this in mind we couple only species A to the polar order parameter $\mathbf{P}$. We assume $\mathcal{F}^A_{\text{vpfc}} = \mathcal{F}^B_{\text{vpfc}} = \mathcal{F}_{\text{vpfc}}$ and thus e.g. equal lattice distance of the active and passive particles. The resulting dynamical equations are:

$$\begin{aligned}
\frac{\partial \psi_A}{\partial t} &= M_0^A \Delta \left( \frac{\delta \mathcal{F}[\psi_A]}{\delta \psi_A} + a\psi_A \psi_B^2 \right) - v_0 \nabla \cdot (\psi_A \mathbf{P}) \\
\partial_t \mathbf{P} &= \alpha_2 \Delta \mathbf{P} - \alpha_4 \mathbf{P} - v_0 \nabla \psi_A - \beta \mathbf{P} \mathbb{1}_{\psi_A \leq 0} \\
\frac{\partial \psi_B}{\partial t} &= M_0^B \Delta \left( \frac{\delta \mathcal{F}[\psi_B]}{\delta \psi_B} + a\psi_A^2 \psi_B \right),
\end{aligned} \tag{4.1}$$

which define a microscopic field-theoretical approach for binary mixtures of interacting active and passive particles.

## 4.2 Results

We solve equations (4.1) in two dimensions using the same parallel finite element approach described in the previous chapter and at the end of chapter 1 [29, 134]. The computational domain is a square of size $L = 200$ with periodic boundary conditions. The initial condition for $\psi_A$ and $\psi_B$ is calculated using the sum of the local density peaks, formula (1.14), with lattice distance $d = 4\pi/\sqrt{3}$ determined by the free energy equation (1.4) [40], with the centers placed randomly according to a packing algorithm [156]. The $\mathbf{P}$ field is set to zero initially, unless otherwise specified.

As in chapter 3 each maximum in the one-particle density fields $\psi_A$ and $\psi_B$ is interpreted as an active or passive particle, respectively. The diameter of the particle is defined by the lattice distance $d$. We track again the particle positions $\mathbf{x}^i_{A,B}(t)$ and use this information to compute the particle velocities $\mathbf{v}^i_{A,B}(t)$ as the discrete time derivative of two successive maxima. We define the total particle density $\phi = N\sigma/L^2$, with $N$ the total number of particles $N = N_A + N_B$ and $N_{A,B}$ the number of $A$ and $B$ particles, respectively. The parameter $\sigma = \pi(d/2)^2$ is the area occupied by a single particle. The fraction of active particles present in the system is $\eta_A = N_A/N$. When a small fraction of particles is active ($\eta_A < 0.2$) we are in the regime of active doping, and analyse how a passive system is influenced by the presence of a few active particles. Increasing the number of active particles ($\eta_A > 0.7$) we are in the regime of an active bath and study how a few passive particles affect an active system.

When simulating equations (4.1) we fix the following parameters, see table 4.1, unless otherwise specified in the figure captions.

| $a$ | $v_0$ | $\alpha_2$ | $\alpha_4$ | $\beta$ | $H$ | $r$ | $M_0^A$ | $M_0^B$ |
|---|---|---|---|---|---|---|---|---|
| 200 | 1.5 | 0.2 | 0.1 | 2 | 1500 | -0.9 | 70 | 70 |

Table 4.1: Model parameters to be used in the simulations.

### 4.2.1 A preliminary study: binary collisions between active and passive particles

We begin with analyzing a binary collision of an active and a passive particle. Figures 4.1(a) and (b) shows the results for two different values of the mobility of the passive particle, $M_0^B = 10$ (left) and $M_0^B = 70$ (right). At time $t = 0$ a passive particle (shown as a black disk) is placed at the origin. An active particle, shown as a fixed contour line of $\psi_A$, is placed a few lattice lengths to the left with a homogeneous polarization directed towards the right. For the low mobility case ($M_0^B = 10$, left) the active particle bounces back after colliding with the passive particle, which does not move. This is confirmed by a plot of the $x-$component of the velocity for both particles (figure 4.1(c)).

For the opposite case of high mobility ($M_0^B = 70$, right) the passive particle is transported along the $x-$axis by the active particle (the black arrow in figure 4.1(b) represents the trajectory of the passive particle). The $x-$component of the velocities shown in figure 4.1(d)) confirm this. The collision causes a slow down of the active particle, and results in a movement of the active and the passive particle with the same velocity.

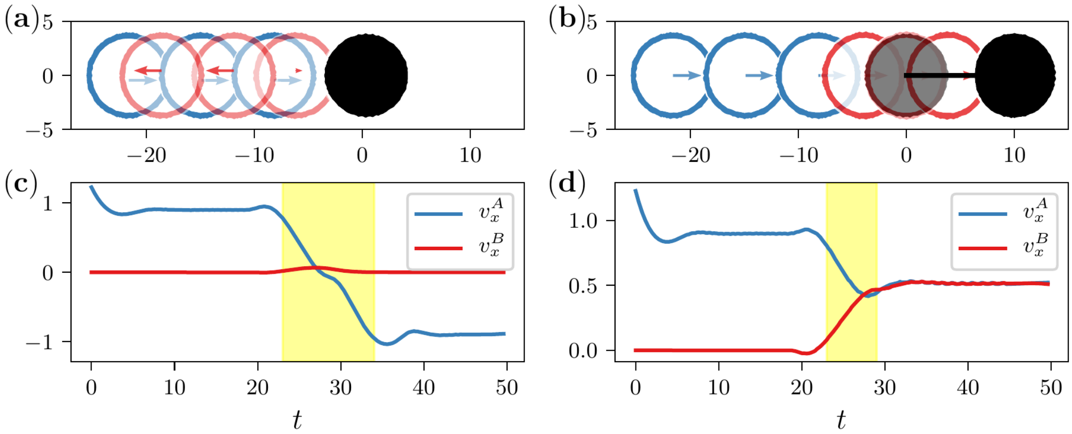

Figure 4.1: (a), (b) Time series of a head-on collision between an active and a passive particle for low passive mobility $M_0^B = 10$ (a) and high passive mobility $M_0^B = 70$ (b). The active particle is shown (at different times) as a contour line of $\psi_A$ and its orientation is represented by an arrow. The blue (red) color is used to show the particle before (after) the collision. The final position of the passive particle is shown as a black disk, whereas in (b) the transparent black disk represents the initial condition of the passive particle and the black line its trajectory. The active particle bounces back after the collision (a) and transport the passive particle (b). The velocities along the $x-$direction of active and passive particles are shown as a function of time in figure (c) for $M_0^B = 10$ and (d) for $M_0^B = 70$. The yellow region represents the approximate time of the collision.

This preliminary analysis shows that for low values of the passive mobility $M_0^B$ passive particles can act as fixed obstacles. In this case a collision causes a change in the active particle direction. However, for large values of $M_0^B$ the passive particle is transported by the active particle. The active particle does not change its direction, only its velocity decreases. These qualitative differences will also affect larger systems, which will be analyzed next.

### 4.2.2 Active doping: how active particles can enhance crystallization

It has been shown by particle simulations [150, 151] and experimentally [144] that the crystalline structure of passive particles is altered by the presence of active agents. More precisely active particles generate density variations in the passive system and promote crystallization, leading to the formation of passive clusters. To analyze these phenomena with our microscopic field-theoretical approach we need to identify if a particle belongs to a cluster. We follow the definition of [144] where two criteria have to be fulfilled. The nearest neighbor distances are less than $3/2d$ and the coordination number is $6$. We also add to the cluster all the remaining particles that are within a distance of $3/2d$ from it.

Figure 4.2 shows snapshots with passive clusters for different $\eta_A$ and $\phi$. The time evolution of the percentage of passive particles which belong to a cluster $X_f$ is shown in figure 4.3. For dilute systems ($\phi = 0.5$, figure 4.2(a)) $X_f$ slowly increases with time. Increasing the fraction of active particles $\eta_A$ leads to larger values of $X_f$. However, it remains relatively low, rarely exceeding $20\%$, for the considered time ($t = 1000$). Increasing the density ($\phi = 0.6$, figure 4.2(b)) the system changes from a state where no clusters are present ($t = 0$) to a state where up to $50\%$ of the passive particles are found in clusters. A maximum $X_f$ is observed for $\eta_A = 0.1$, where $X_f$ saturates at $t = 1000$. Further increasing the number of active particles leads to a reduction of $X_f$. Adding more and more active particles to systems with already existing crystalline clusters introduces disorder, a phenomena already observed in [144]. By further increasing the density ($\phi = 0.7$, figure 4.2(c)) some clusters are already present for the random initial configuration at $t = 0$, due to spontaneous crystallization. Active particles can be inside these regions, thus disturbing their symmetry. This explains why the system behaves in the opposite way as for the dilute case, with $X_f$ decreasing as the fraction of active particles $\eta_A$ increases. Finally for $\phi = 0.8$ the initial configuration is already almost completely crystallized ($X_f \simeq 1$ for $t = 0$, figure 4.2(d)). Adding active particles partially destroys the crystalline structure (figure 4.3(d)) and $X_f$ decreases for increasing $\eta_A$. We thus observe both phenomena, enhanced crystallization in dilute systems and suppressed crystallization in dense systems.

All these results are in qualitative agreement with [144]. It is in principle possible to perform a more quantitative analysis, comparing, for instance, the number of clusters vs

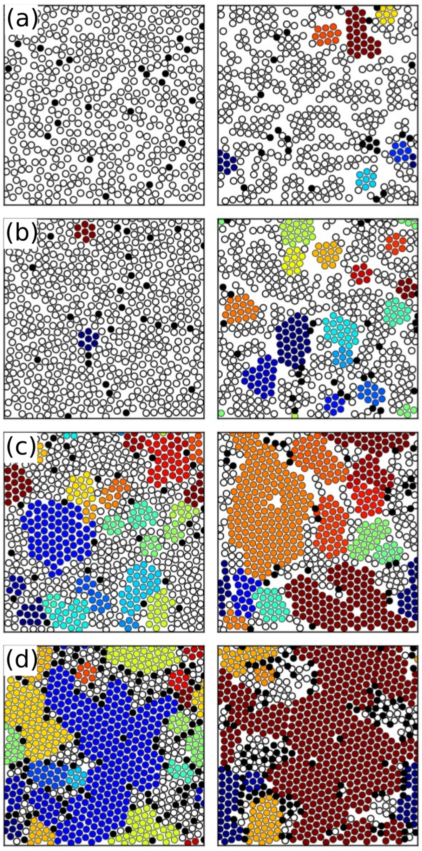

Figure 4.2: Snapshots showing passive clusters for different total densities and fractions of active particles $\phi$ and $\eta_A$ at time $t = 0$ (first column) and at time $t = 1000$ (second column). Particles with the same color belong to the same cluster, white disks represent passive particles not belonging to any cluster and black disks are active particles. (a) $\phi = 0.5$, $\eta_A = 0.05$, (b) $\phi = 0.6$, $\eta_A = 0.05$ (c) $\phi = 0.7$, $\eta_A = 0.05$, (d) $\phi = 0.8$, $\eta_A = 0.15$. Other parameters are $M_0^A = M_0^B = 50$.

time. This would require a more comprehensive model than the one presented here and it goes beyond the scope of our work.

A final observation concerns how the dynamics of the active particles is affected by the presence of passive ones. In figure 4.4 the maximum of the particle-averaged mean square displacement $\langle \Delta r^2(t) \rangle$ for active particles is shown as a function of $\phi$ and $\eta_A$. No data is shown for $\eta_A = 0.01$, as the number of active particles is too small for meaningful averages. We observe a clear correlation between this value and the crystallization in the system: the higher $X_f$, the smaller is the maximum displacement of active particles until, for the extreme case of $\phi = 0.8$ and $\eta_A = 0.05$, active particles are trapped inside a big passive cluster and show a very small displacement.

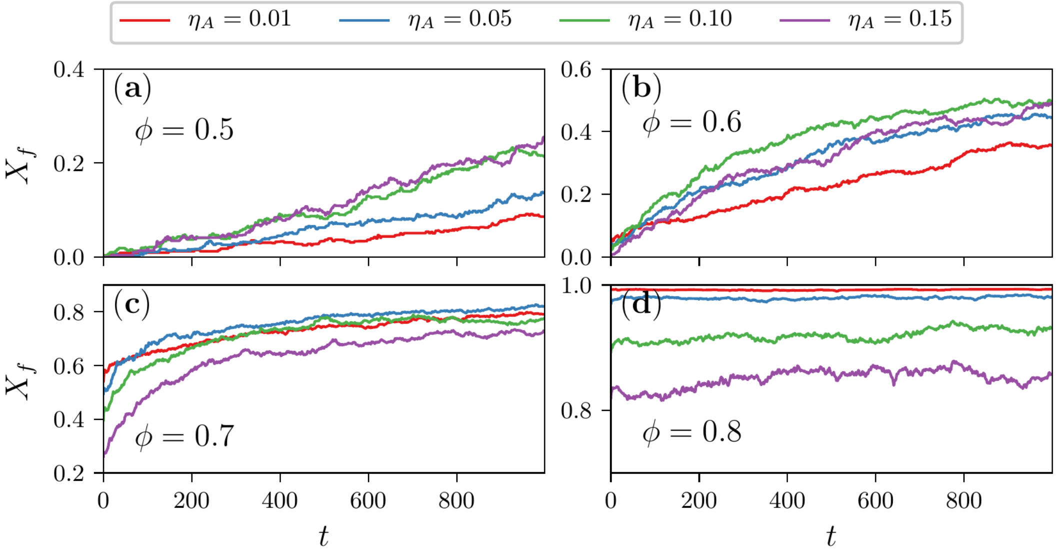

Figure 4.3: Percentage of passive particles belonging to a cluster $X_f$ as a function of time for different total densities and fractions of active particles $\phi$ and $\eta_A$. We observe that for $\phi = 0.5$ and $\phi = 0.6$ (top row), increasing the number of active particles lead to an increase of $X_f$, whereas the opposite is true for $\phi = 0.7$ and $\phi = 0.8$ (bottom row). Other parameters are $M_0^A = M_0^B = 50$. Each curve has been obtained as the average of five different simulations started with different initial conditions.

### 4.2.3 Active bath: how passive particles can suppress collective migration

In chapter 3 we have seen that inelastic collisions in systems which are composed solely of active particles can lead to collective motion. We characterized the state of collective migration by the translational order parameter $\phi_T = 1/N_A \left|\sum_{i=1}^{N_A} \hat{\mathbf{v}}_A^i(t)\right|$ being close to one, with $\hat{\mathbf{v}}_A^i(t)$ the unit velocity vector for the $i-$th active particle at time $t$. We here analyze the stability of the state of collective migration, if passive particles are introduced in the system. How do the total density $\phi$, the fraction of active particles $\eta_A$ and the mobility of passive particles $M_0^B$ affect this state?

To consider a dense system we fix $\phi = 0.9$ and we further set $\eta_A = 0.9$. We have seen (figure 4.1) that for low mobility $M_0^B$ passive particles act as fixed objects. The situation is therefore comparable with experimental studies for active colloids in disordered environments [149], which show a suppression of collective motion. Also in our simulations the active system does not reach a state of collective motion, as shown from the time series of $\phi_T$ (figure 4.5(b)). However, the situation changes if we increase $M_0^B$, thus making passive particles mobile. Figure 4.5(a) shows the average velocity $\tilde{\mathbf{v}}_B$ of the passive particles as a function of their mobility. Increasing $M_0^B$, the average passive

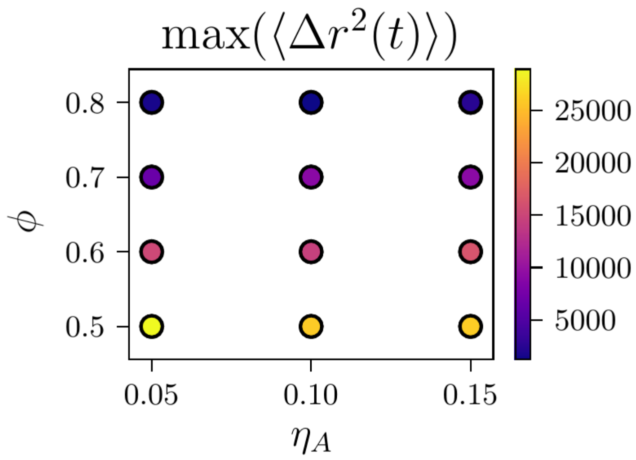

Figure 4.4: Maximum of the particle-averaged mean square displacement $\langle \Delta r^2(t) \rangle$ of active particles moving in a binary mixture for different values of $\phi$ and $\eta_A$. Active particles travel a longer distance when the passive particles have not crystallized, until the extreme case of $\phi = 0.8$, $\eta_A = 0.05$ where the maximum mean square displacement is so low that active particles are basically trapped. Other parameters are $M_0^A = M_0^B = 50$. Each point has been obtained as the average of five different simulations started with different initial conditions.

particles velocity $\tilde{\mathbf{v}}_B$ also increases, meaning that passive particles are transported by the active ones, as expected. For $M_0^B \geq 50$ a state of collective migration is reached (figure 4.5(b)), even though the time required to reach it is larger than in the homogeneous case $\eta_A = 1$ (no passive particles present).

We now fix the mobility $M_0^B = 70$ and vary $\phi$ and $\eta_A$. We reduce $\phi$ down to $0.7$, a limit for which a state of collective migration would still be reached in a homogeneous active system ($\eta_A = 1$), as seen from the purple lines in figure 4.6. For $\phi = 0.9$ a state of collective migration is reached for $\eta_A = 0.9$ but with a longer transient phase than for the homogeneous case (green line in figure 4.6(c)). For $\eta_A = 0.8$ we already see a small perturbation from the unit value for $\phi_T$ and for $\eta_A = 0.7$ collective migration is no longer reached. We here observe the accumulation of passive particles in certain regions, see also figure 4.7(d). This hinders the active particles from following a straight trajectory and thus the formation of collective migration. Things change by reducing the total density to $\phi = 0.8$. The state of collective migration is not reached, independently of the value of $\eta_A$ (figure 4.6(b)). However, for $\eta_A = 0.9$, green curve in figure 4.6(b), a new state is formed, where the order parameter $\phi_T$ is at least locally close to one. This new state is discussed below and can be seen in the snapshots in figures 4.7(a) and (b). For

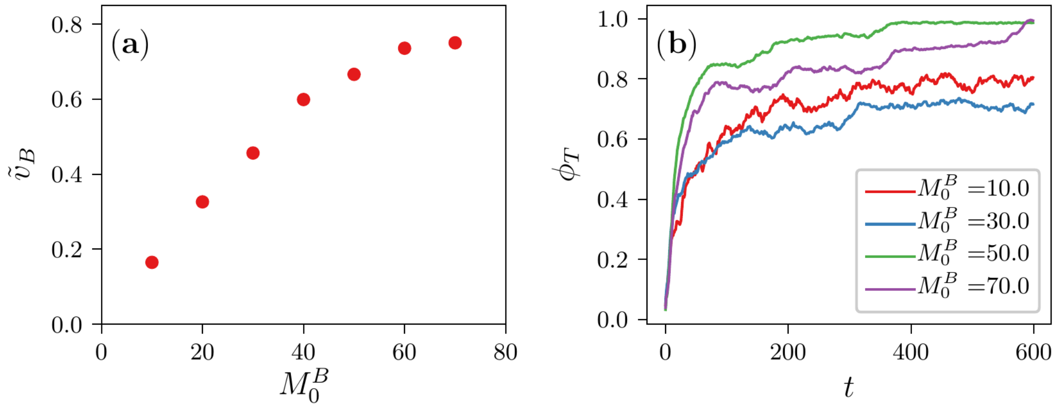

Figure 4.5: (a) Average velocity $\tilde{v}_B$ of passive particles as a function of their mobility in an active bath with $\phi = 0.9$, $\eta_A = 0.9$. $\tilde{v}_B$ increases almost linearly for small $M_0^B$ until it starts to saturate at around $M_0^B = 70$. (b) Translational order parameter $\phi_T$ as a function of time for different mobility $M_0^B$. For small values of $M_0^B$ there is no collective migration, for intermediate values this state is reached quite fast, whereas for high mobility the transient phase to reach collective migration increases. However simulations are not so numerically stable for small and intermediate values of the mobility and this is why we choose $M_0^B = 70$ for the analysis in figure 4.6. $M_0^A = 100$ for both cases. The data have been obtained as the average of ten different simulations started with different initial conditions.

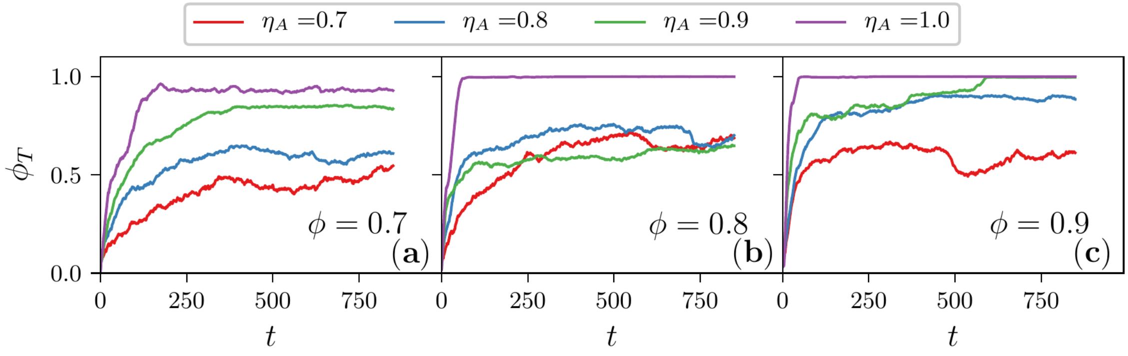

Figure 4.6: Order parameter $\phi_T$ as a function of time for different values of $\phi$ and $\eta_A$. The purple curve corresponds to the case $\eta_A = 1$, i.e. no passive particles present. We see that in all other cases the state of collective migration is reached later (longer transient phase) or not reached at all, especially for lower $\eta_A$ (red curves). Other parameters are $M_0^A = 100$ and $M_0^B = 70$. The data have been obtained as the average of ten different simulations started with different initial conditions.

$\phi = 0.7$ (figure 4.6(a)) a decrease in $\eta_A$ leads to a decrease of $\phi_T$. In this situation there is enough empty space in the system to allow active particles to change their trajectories when interacting with passive ones. This causes a perturbation that gets bigger as the number of passive particles increase, leading to a decrease of $\phi_T$.

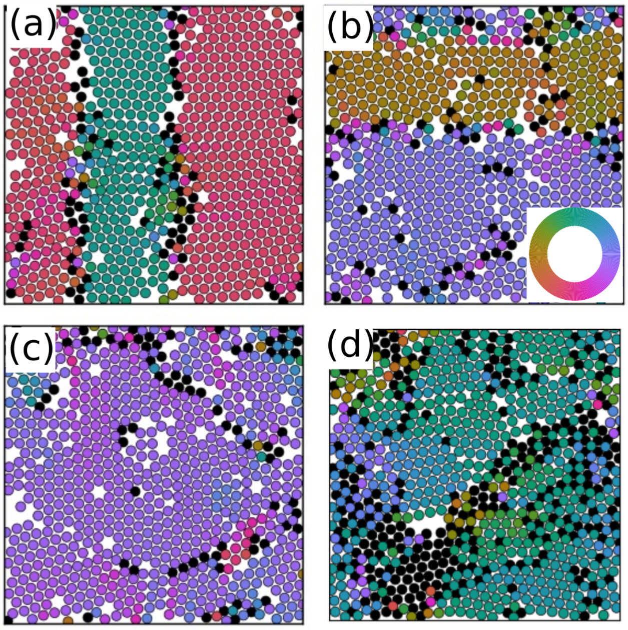

Figure 4.7: The color code corresponds to the orientation of the single particle velocity and black disks represent passive particles. (a) Snapshot of a laning state, with two macro regions of active particles having exactly opposite orientation. This state can last for a long time thanks to the presence of passive particles at the boundary between the two regions. (b) Another laning state. Here, less passive particles are accumulated at the boundary between the moving active regions. This situation is less stable and, at a later time (c), active particles all move in the same direction, whereas passive ones form chains, which persist over longer periods of time. (d) Passive particles forming clusters in an active bath. (a) - (c) regime $\phi = 0.8$, $\eta_A = 0.9$, (d) regime $\phi = 0.9$, $\eta_A = 0.7$.

A more detailed investigation of the intermediate regime with $\phi = 0.8$ and $\eta_A = 0.9$ (figure 4.7(a) and (b)) shows an intermediate state with two lanes of active particles moving in opposite direction. The lanes are separated by passive particles (black disks), that prevent the alignment of the collectively migrating domains. It is more stable in figure 4.7(a), persisting for the whole simulation time, and less stable in figure 4.7(b), where the alignment of passive particles will be destroyed after a while and a transition to collective migration follows. This state is known as laning state and it is characterized by an alignment that is globally nematic, but polar within each lane. It has already been observed for self-propelled rods with an effective nematic alignment [5, 155], soft deformable self-propelled particles with high aspect ratio [16] and a mixture of self-propelled and passive rods interacting solely through excluded volume interactions [146]. It is to our knowledge the first time that this laning state is observed in a mixture of interacting spherical-like particles whose velocity alignment would be globally polar in the absence of passive particles, see figure 3.6 [29].

Even if a state of pure collective migration is reached, the passive particles are not randomly distributed, but are transported by the active particles, filling the holes between them. For $\phi \simeq 0.8$ the packing of the collectively migrating active particles allows the passive particles to arrange in the free space. They form chain-like structures (figure 4.7(c)) which persist over longer periods of time and are transported by the active particles. If the number of passive particles is increased $\eta_A = 0.7$ a clustering of passive particles within the active bath can be observed, see figure 4.7(d). These new states and patterns are characteristic for binary mixtures and should be explored further, both numerically and experimentally.

## 4.3 Extensions

Several possible extensions are possible starting from the dynamical equations to describe binary mixtures of interacting active and passive particles, system (4.1). We here show the dynamical equations for two of these, namely how to make both species active and how to couple several passive species with different lattice distance to an active species. We will however not show any results for these cases in this thesis. An extension to include a different interaction potential than the repulsive one given by equation (1.17) is also possible, but will not be considered here.

### 4.3.1 Both species active

First, we consider the case where we have two different species of active particles described by densities $\psi_A$ and $\psi_B$ with two different orientation fields $\boldsymbol{P}_A$ and $\boldsymbol{P}_B$. Allowing for two different lattice distances $d_{q_i} = \frac{4\pi}{\sqrt{3}q_i}$, $i = A, B$, the dynamical equations for such a system read:

$$\begin{aligned}
\frac{\partial \psi_A}{\partial t} &= M_0^A \Delta \left( \frac{\delta \mathcal{F}_{\mathrm{vpfc}}^{(q_a)}[\psi_A]}{\delta \psi_A} + a\psi_A \psi_B^2 \right) - v_0^A \nabla \cdot (\psi_A \mathbf{P}_A) \\
\partial_t \mathbf{P}_A &= \alpha_2^A \Delta \mathbf{P}_A - \alpha_4^A \mathbf{P}_A - v_0^A \nabla \psi_A - \beta \mathbf{P}_A \mathbb{1}_{\psi_A \leq 0} \\
\frac{\partial \psi_B}{\partial t} &= M_0^B \Delta \left( \frac{\delta \mathcal{F}_{\mathrm{vpfc}}^{(q_b)}[\psi_B]}{\delta \psi_B} + a\psi_A^2 \psi_B \right) - v_0^B \nabla \cdot (\psi_B \mathbf{P}_B) \\
\partial_t \mathbf{P}_B &= \alpha_2^B \Delta \mathbf{P}_B - \alpha_4^B \mathbf{P}_B - v_0^B \nabla \psi_B - \beta \mathbf{P}_B \mathbb{1}_{\psi_B \leq 0},
\end{aligned} \tag{4.2}$$

where the superscripts in the coefficients refer to the different species and $\mathcal{F}_{\mathrm{vpfc}}^{(q_i)} = \mathcal{F}_{\mathrm{pfc}}^{(q_i)} + \mathcal{F}_{\mathrm{penalty}}$, with $\mathcal{F}_{\mathrm{pfc}}^{(q_i)}$ and $\mathcal{F}_{\mathrm{penalty}}$ given by equations (1.20) and (1.10), respectively.

### 4.3.2 Several species

We now consider the case of $N$ different species. The particle radius of species $i$ is given by $r_{q_i} = \frac{2\pi}{\sqrt{3}q_i}$ and they interact repulsively via an extension of the interaction energy (1.17):

$$\mathcal{F}_{\mathrm{int}}^{1,\ldots,N}[\psi_1, \ldots, \psi_N] = a \prod_{i=1}^{N} \psi_i^2. \tag{4.3}$$

We make species 1 active by coupling it to a polarization field $\boldsymbol{P}$, while species $i = 2..N$ remain passive. We then obtain the following system of $N+1$ dynamical equations:

$$\begin{aligned}
\frac{\partial \psi_1}{\partial t} &= M_0^1 \Delta \left( \frac{\delta \mathcal{F}_{\mathrm{vpfc}}^{(q_1)}[\psi_1]}{\delta \psi_1} + a\psi_1 \prod_{j=2}^{N} \psi_j^2 \right) - v_0 \nabla \cdot (\psi_1 \mathbf{P}) \\
\partial_t \mathbf{P} &= \alpha_2 \Delta \mathbf{P} - \alpha_4 \mathbf{P} - v_0 \nabla \psi_1 - \beta \mathbf{P} \mathbb{1}_{\psi_1 \leq 0} \\
\frac{\partial \psi_i}{\partial t} &= M_0^i \Delta \left( \frac{\delta \mathcal{F}_{\mathrm{vpfc}}^{(q_i)}[\psi_i]}{\delta \psi_i} + a\psi_i \prod_{\substack{j=1 \\ j \neq i}}^{N} \psi_j^2 \right), \quad i = 2..N,
\end{aligned} \tag{4.4}$$

where again the superscripts in the coefficients refer to the different species and $\mathcal{F}_{\mathrm{vpfc}}^{(q_i)} = \mathcal{F}_{\mathrm{pfc}}^{(q_i)} + \mathcal{F}_{\mathrm{penalty}}$, with $\mathcal{F}_{\mathrm{pfc}}^{(q_i)}$ and $\mathcal{F}_{\mathrm{penalty}}$ given by equations (1.20) and (1.10), respectively.

## 4.4 Summary

In summary, our microscopic field-theoretical approach for mixtures of interacting active and passive particles has been used to investigate a wide spectrum from systems with $\phi < 0.7$ to dense systems $\phi > 0.7$ with a relatively low fraction of active particles $\eta_A < 0.2$ (active doping) and a relatively high fraction $\eta_A > 0.7$ (active bath), respectively. We have demonstrated with one and the same model a variety of known phenomena, such as enhanced crystallization via active doping [144, 150] and suppressed crystallization in dense systems [144]. We also analyzed the limits of collective migration, which for the special case of immobile passive particles qualitatively reproduce the results in [149]. Within the experiments in [144] and in our simulations the suppression of collective migration sensitively depends on the fraction of immobile passive particles. Within the experimentally less explored state of mobile passive particles we found new phenomena. For fractions of passive particles, for which collective migration is suppressed if the passive particles are immobile, collective motion is still possible if the mobility of these particles is large enough. But there are also intermediate regimes, known as laning states, where lanes of active particles moving in opposite direction are separated by boundary layers of passive ones. We further found chains of passive particles and clusters which persist for a relatively long time. A rigorous classification of these states remains open and should be addressed together with experimental investigations.

Finally, we have shown how the approach can easily be modified to consider more than two species with different sizes and two active species with different self-propulsion velocities and orientation fields. This makes the active binary VPFC model, system (4.1), a generic tool to study active systems in complex environments. While the approach is unable to reach system sizes possible with classical agent-based methods, it provides a minimal approach for a more detailed microscopic description of binary mixtures, which does not need any explicit alignment rule, accounts for processes within the particle and allows for small particle deformations. Another step towards an even more microscopic description would be to extend the dry phase field model, equations 2.12, to include a passive species as well. A comparison between this model and the active binary VPFC one presented in this chapter would then be possible, similarly to what we have done for the single species case in chapter 3.

# 5 Dry active nematics on curved surfaces

When active systems are confined on curved surfaces, topological constraints strongly influence the emerging spatiotemporal patterns. Using these topological constraints to guide collective cell behavior might be a key in morphogenesis [82] and active nematic films on surfaces have been proposed as a promising road to engineer synthetic materials that mimic living organisms [30]. However, the complex dynamics of such topological active systems remains wildly unexplored. It is therefore tempting to extend the microscopic field-theoretical model introduced in chapter 3 to curved surfaces in order to shed some light on these phenomena. In chapter 2 we have seen how this has been done for crystals of self-propelled colloidal particles on a sphere [90], equations (2.20). We have also seen that an extension of the microscopic field-theoretical model of chapter 3 to active nematics on curved surfaces would involve the coupling of a nematic order tensor $\boldsymbol{Q}$ [91] to the PFC model and this is not trivial. Given these difficulties we want to introduce a simpler model in order to perform a preliminary study of these systems and thus understand them better. For this reason, in this chapter we introduce an agent-based model to describe dry active nematics on curved surfaces [84].

First, we shortly describe how defects behave in active nematics and then we introduce an agent-based model for active particles on curved surfaces. Thanks to the flexibility of the model, we show that it can be used to describe active particles with different kind of symmetries (such as nematic or polar). We use this model to study the spatiotemporal patterns that emerge when an active nematic film is topologically constraint. These topological constraints allow to control the nonequilibrium dynamics of the active system. We consider ellipsoidal shapes for which the resulting defects are 1/2 disclinations and analyze the relation between their location and dynamics and local geometric properties of the ellipsoid. We highlight two dynamic modes: a tunable periodic state that oscillates between two defect configurations on a spherical shape and a tunable rotating state for oblate spheroids. We further demonstrate the relation between defects and high Gaussian curvature and umbilical points and point out limits for a coarse-grained description of defects as self-propelled particles. Finally, we show how the same model can be used to describe nematic and polar active particles on toroidal surfaces. For the nematic case, we observe a localization of positive and negative defects on regions of positive and negative curvature, respectively, as experimentally found in [83]. An oscillating state, where particles rotate along the toroidal direction of the surface, regularly changing direction, is observed for the polar case.

## 5.1 Defect dynamics in active nematics

As in passive systems the mathematical Poincaré-Hopf theorem forces topological defects to be present in a topologically constraint active nematic film. On a sphere this leads to an equilibrium defect configuration with four $+1/2$ disclinations arranged as a tetrahedron [157–159], see figure 2.1. The disclinations repel each other and this arrangement maximizes their distance. In active systems unbalanced stresses drive this configuration out of equilibrium. But in contrast to planar active nematics with continuous creation and annihilation of defects [160–163] the creation of additional defect pairs can be suppressed on curved surfaces, which is demonstrated in [30, 86] for an active nematic film of microtubules and molecular motors, encapsulated within a spherical lipid vesicle. This provides an unique way to study the dynamics of the four defects in a controlled manner and leads to the discovery of a tunable periodic state that oscillates between the tetrahedral and a planar defect configuration. We confirm this finding by computer simulations, see figure 5.2. On a surface with non-constant Gaussian curvature local geometric properties influence the position of the defects and thus can be used to control defect dynamics.

Within a coarse-grained model $+1/2$ disclinations in planar active nematic films can be effectively described by self-propelled particles with a velocity proportional to the activity [164]. In [30] this relation is extended to spherical nematics. Four self-propelled particles on a sphere also oscillate between the planar and tetrahedral configuration. Both descriptions can be quantitatively linked to each other, but also differences can be pointed out, which become more evident for more general surfaces.

## 5.2 A model for active particles on curved surfaces

For active systems in flat geometries various theoretical descriptions have been proposed, see e.g. [1, 59]. One of the most studied approaches are Vicsek-like models [14]. We consider an extension of these models which includes excluded volume [18, 165–167] and classify systems by the head-tail symmetry of their particles in polar or nematic. We do not include any noise term in our model and also do not consider hydrodynamic interactions.

We consider $N$ active particles of mass $m_i = 1$, which are constrained to move on a surface algebraically described by $g(\mathbf{q}) = 0$, with particle positions $\mathbf{q} = (\mathbf{q}_1, \ldots, \mathbf{q}_N)$. Newton's equations of motion (EOM) with holonomic constraint $g(\mathbf{q})$ read:

$$\frac{\mathrm{d}}{\mathrm{d}t}\mathbf{q} = \mathbf{v}, \quad \frac{\mathrm{d}}{\mathrm{d}t}\mathbf{v} = \mathbf{F} - G\left(\mathbf{q}\right)^T \boldsymbol{\lambda}, \quad g\left(\mathbf{q}\right) = \mathbf{0}, \tag{5.1}$$

with forces $\mathbf{F} = (\mathbf{F}_1, \ldots, \mathbf{F}_N)$ and velocities $\mathbf{v} = (\mathbf{v}_1, \ldots, \mathbf{v}_N)$. $\boldsymbol{\lambda} = (\lambda_1, \ldots, \lambda_N)$ are the Lagrange multipliers and $G(\mathbf{q}) = \nabla_{\mathbf{q}} g(\mathbf{q})$ is the Jacobian of $g(\mathbf{q})$. The force $\mathbf{F}_i$ can be written as:

$$\mathbf{F}_i = -\gamma \mathbf{v}_i + \sum_{j=1}^{N} \mathbf{F}_{ij} + \mathbf{F}_i^{ac}, \tag{5.2}$$

where $\gamma$ is the translational friction coefficient, $\mathbf{F}_i^{ac}$ the active force acting on the $i$-th particle and $\mathbf{F}_{ij}$ the pair-interaction force between the $i$-th and the $j$-th particles. Additionally, every particle has an internal degree of freedom, namely its orientation $\mathbf{n}_i$. Denoting the angular velocity by $\boldsymbol{\omega}_i$ we have the following EOM for the orientational dynamics:

$$\frac{\mathrm{d}}{\mathrm{d}t}\mathbf{n}_i = \boldsymbol{\omega}_i \times \mathbf{n}_i, \quad \frac{\mathrm{d}}{\mathrm{d}t}\boldsymbol{\omega}_i = -\gamma_a \boldsymbol{\omega}_i + \mathbf{T}_i\left(\mathbf{q}, \mathbf{n}\right), \tag{5.3}$$

where $\gamma_a$ is the rotational friction coefficient and $\mathbf{T}_i(\mathbf{q}, \mathbf{n})$ is the torque acting on the $i$-th particle, with $\mathbf{n} = (\mathbf{n}_1, \ldots, \mathbf{n}_N)$. Depending on the specific form for the active force $\mathbf{F}_i^{ac}$, the pair-interaction force $\mathbf{F}_{ij}$, the torque $\mathbf{T}_i(\mathbf{q}, \mathbf{n})$ and the holonomic constraint $g(\mathbf{q})$ we will be able to describe polar and nematic active systems on various surfaces.

### 5.2.1 Active polar particles

For active polar particles on a sphere of radius $R$ we specify [87] $\mathbf{F}_i^{ac} = v_0 \mathbf{n}_i$ with a constant self-propulsion velocity $v_0$. The particles are spheres of radius $\sigma$ with a short-range repulsion between them. The pair-interaction force is therefore:

$$\mathbf{F}_{ij} = \begin{cases} k(2\sigma - q_{ij}^g)\frac{\mathbf{q}_i - \mathbf{q}_j}{q_{ij}}, & \text{for } q_{ij}^g < 2\sigma \\ 0, & \text{otherwise,} \end{cases} \tag{5.4}$$

where $k$ is an elastic constant, $q_{ij} = |\mathbf{q}_i - \mathbf{q}_j|$ the euclidean distance and $q_{ij}^g = |\mathbf{q}_i - \mathbf{q}_j|_g$ the geodesic distance. Parallel orientations between neighboring particles are favored and therefore we use the aligning torque $\mathbf{T}_i(\mathbf{q}, \mathbf{n}) = -J \sum_{j \in U(i)} (\mathbf{n}_i \times \mathbf{n}_j)$, with the strength $J > 0$ and the first shell of neighbors of particle $i$ $U(i)$, identified as all the particles within a cutoff radius of $2.4\sigma$ from $\mathbf{r}_i$. The holonomic constraint for a sphere of radius $R$ reads $g(\mathbf{q}_i) = q_{i,1}^2 + q_{i,2}^2 + q_{i,3}^2 - R^2$, with $\mathbf{q}_i = (q_{i,1}, q_{i,2}, q_{i,3}) \in \mathcal{R}^3$. This approach can be used to reproduce the results in [87] in which the overdamped limit, the euclidean distance instead of the geodesic distance and an additional noise term are considered. We use it at the end of the chapter to show simulations of active polar particles on a toroidal geometry. In this case, the simulation parameters are $(J, k, \sigma, \gamma, \gamma_a, v_0) = (5, 3, 2, 0.1, 2, 0.05)$.

### 5.2.2 Active nematic particles

We use the tensor order parameter $Q_{\alpha\beta}^j = \frac{1}{2}\left(3 n_\alpha^j n_\beta^j - \delta_{\alpha\beta}\right)$ to describe active nematic particles, where the upper index corresponds to the particles and the lower indices represent the components $x, y, z$. The active force does not distinguish 'head from tail' and it thus has the form:

$$\mathbf{F}_i^{ac} = -v_0 \sum_{j \in U(i)} \mathbf{Q}^j \frac{\mathbf{q}_i - \mathbf{q}_j}{q_{ij}^2}. \tag{5.5}$$

The torque reflects the fact that both parallel and anti-parallel configurations are favored. It has the form:

$$\mathbf{T}_i = J \sum_{j \in U(i)} \left( (\mathbf{n}_i \cdot \mathbf{n}_j) (\mathbf{n}_i \times \mathbf{n}_j) \right). \tag{5.6}$$

The pair-interaction force $\mathbf{F}_{ij}$ and the holonomic constraint $g(\mathbf{q})$ are the same as in the active polar particles case. The simulation parameters for this case are $(J, k, \sigma, \gamma, \gamma_a, v_0) =$

$(10, 3, 2, 0.1, 2.5, 0.7)$ unless otherwise specified.

### 5.2.3 Coarse-grained defect description

In the coarse-grained defects description by active polar particles [30, 164] the elastic energy between defects is $E \sim \log(q^g_{ij})$, where $q^g_{ij}$ is the geodesic distance between the defects. The pair-interaction force is therefore $\mathbf{F}_{ij} = \frac{k}{q^g_{ij}} \frac{\mathbf{q}_i - \mathbf{q}_j}{q_{ij}}$, which is no longer short-ranged. Defects align anti-parallel to each other and the restoring torque strength is $T_i = J \sum_{j \in U(i)} \cot(\frac{\theta_{ij}}{2})$, where $\theta_{ij}$ is the angle between $\mathbf{n}_i$ and $\mathbf{n}_j$ [30]. The vector form for the torque can be written in terms of the orientations as:

$$\mathbf{T}_i = J \sum_{j \in U(i)} (1 + \mathbf{n}_i \cdot \mathbf{n}_j) \frac{\mathbf{n}_i \times \mathbf{n}_j}{|\mathbf{n}_i \times \mathbf{n}_j|^2} \tag{5.7}$$

Finally the defects are treated as self-propelled particles and the active force is $\mathbf{F}^{ac}_i = v_0 \mathbf{n}_i$. The simulation parameters for this case are $(J, k, \gamma, \gamma_a, v_0) = (3, 4, 0.1, 2.5, 0.11)$ unless otherwise specified. A similar model can also be derived by rigorous perturbation expansion [168]. It differs in 2d from [164] by a velocity-dependent factor. Computational studies on curved surfaces indicate that also with this model the complex defect dynamics on surfaces of non-constant Gaussian curvature can not be obtained.

### 5.2.4 Numerical methods

Equations (5.1) have been numerically solved using RATTLE discretization [169]. The equations for the orientational dynamic, equations (5.3), have been first solved unconstrained with the torque $\mathbf{T}_i$ projected onto the normal plane of the surface at point $\mathbf{r}_i$. Afterwards the orientation $\mathbf{n}_i$ has been projected onto the tangent plane of the surface at point $\mathbf{r}_i$ and the angular velocity $\boldsymbol{\omega}_i$ takes the direction of the normal to the surface at point $\mathbf{r}_i$.

We fix the number of particles $N = 1000$ and the volume fraction $\phi \simeq 1$ (defined as the ratio of the area occupied by the particles and the total surface area, i.e. $\phi = N\pi\sigma^2/A$). The surface area for the sphere is equal to $A = 4\pi R^2$, with $R = 31.6$. The ellipsoid parameters $a, b, c$ have been chosen such that the surface area is equivalent to the surface area of the sphere and the aspect ratio is respected. The nematic order parameter $P$ is defined as the weighted local average of the tensor order parameter $Q$ with respect to the weight $w_{ij} = q_{ij}^{-1}$. The polar order parameter $\omega$ is defined as:

$$\omega_i = \frac{1}{\sum_j w_{ij}} \sum_j \frac{w_{ij}}{2} \boldsymbol{n}_i \cdot \boldsymbol{n}_j \tag{5.8}$$

where the sum is over the nearest neighbors and $w_{ij} = q_{ij}^{-1}$. Defects are calculated as the local center of mass for regions where the local order parameter $P_i$ is smaller then $0.45$ (some corrections were required for regions of high Gaussian curvature, due to strong distortion of the director field).

The simulation code is implemented in C++, using the GeographicLib library [170] for the calculation of the geodesic distances. However, for non-spheroidal ellipsoids the euclidean distance has been used. This approximation can be justified by the short-range interactions. Data have been analyzed using Python, Ovito [171] and Paraview.

### 5.2.5 Geometric properties

Besides a sphere we consider two classes of ellipsoidal surfaces: (i) spheroidal and (ii) non-spheroidal. These ellipsoids are characterized by their major axis $a$, $b$ and $c$ and have non-constant Gaussian curvature

$$K = \frac{a^2 b^6 c^6}{\left(c^4 b^4 + c^4(a^2 - b^2)y^2 + b^4(a^2 - c^2)z^2\right)^2}. \tag{5.9}$$

For spheroidal ellipsoids two of these values are equal. The algebraic description reads $g(\mathbf{q}_i) = \frac{q_{i,1}^2}{a^2} + \frac{q_{i,2}^2}{b^2} + \frac{q_{i,3}^2}{c^2} - 1 = 0$. An umbilical point is a point where the maximum and minimum curvatures coincide. At an umbilical point, the surface is ”locally spherical”. These points are found at

$$\left(\pm a\sqrt{\frac{a^2 - b^2}{a^2 - c^2}}, 0, \pm c\sqrt{\frac{b^2 - c^2}{a^2 - c^2}}\right)^T \tag{5.10}$$

In figure 5.1 we show three different ellipsoids, where umbilical points are highlighted and the color coding corresponds to the Gaussian curvature $K$.

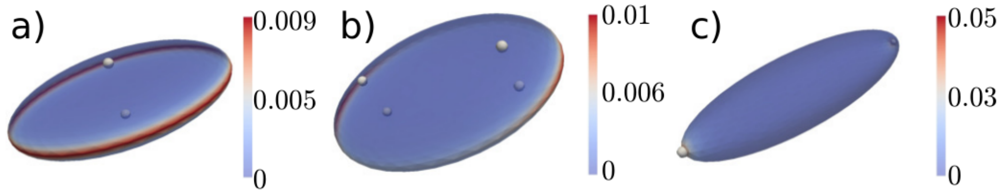

Figure 5.1: Example of an ellipsoid with major axis (a) $a/b = 1$ and $a/c = 4$ (oblate spheroid), (b) $a/b = 1.25$ and $a/c = 4$ (non-spheroidal ellipsoid) and (c) $a/b = 1$ and $a/c = 0.25$ (prolate spheroid). The parameters $a, b, c$ have been chosen such that the surface area of the ellipsoids is equivalent to the surface area of a sphere with radius $R = 31.6$. Umbilical points are shown as points and the Gaussian curvature $K$ is color coded.

## 5.3 Active nematics on closed surfaces

Models similar to the agent-based approach given in equations (5.1) and (5.3) have been formulated for active polar particles on a sphere [87] and on ellipsoidal surfaces [88]. In these situations a robust rotating-band structure around the waist, with two +1 defects at the poles, is found on a sphere. On an ellipsoid the location of the defects is linked to local geometric properties, similar to vortices in surface fluids [172–175]. The defects are related to the Gaussian curvature and to the umbilical points of the surface. For spheroidal ellipsoids there are two umbilical points, which locate the two +1 defects. This configuration is more stable for prolate spheroids, where the umbilical points are at the points of maximal Gaussian curvature at the poles and less stable for oblate spheroids, where the umbilical points and the maximum in Gaussian curvature are separated. As in the spherical case a rotating-band structure is formed, with possible sub-bands which counter rotate depending on the initial condition. New dynamical features are found for non-spherical ellipsoids. They have four umbilical points. For lower velocities the defects encircle pairs of umbilical points and for larger velocities the defects are found at the high Gaussian curvature regions between each pair of umbilical points. With this richness in dynamics found for active polar particles on non-constant Gaussian curvature surfaces, we expect similar behavior for active nematic particles. We perform a systematic investigation of the impact of non-constant Gaussian curvature constraints on the emergence of complex patterns and oscillations. We also ask up to which complexity of the geometry the dynamics of the four 1/2 disclinations can be effectively described by self-propelled polar particles.

### 5.3.1 Sphere

Before answering the questions above, we first analyze the spherical case in more detail. We track the oscillations between the planar and tetrahedral defect configurations on a spherical vesicle, figure 5.2, and the positions of the defects, as explained in the "numerical methods" section. To track the oscillations between the planar and tetrahedral configurations we calculate the average angle $\langle \alpha \rangle = \frac{1}{6} \sum_{i<j} \alpha_{ij}$, where $\alpha_{ij}$ denotes the angle between the radii connecting the center of the sphere to defects $i$ and $j$. Computing the power spectrum from the time series of the average angle $\langle \alpha \rangle$, we obtain the frequency for these oscillations, which linearly depends on the activity. The same results, but with a small offset and a different slope, are obtained for the coarse-grained description by self-propelled particles, see figure 5.3(a) and (c). As a consequence, for each activity in the nematic film a self-propulsion velocity can be determined in the coarse-grained description, which resamples the frequency of the planar-tetrahedral defect oscillation. Differences between both descriptions are found if we compare the trajectories of the defects and self-propelled particles. Within the considered time interval the 1/2 disclinations are locally confined, with each defect only covering a part of the vesicle. This is in contrast to the trajectories of the self-propelled particles, which rotate within a band structure leaving parts of the vesicle uncovered, see figure 5.3(b). The experimental defect trajectories in [30] differ from both descriptions: they are global, covering the whole vesicle. The discrepancy might be a consequence of the considered short-range interactions in our model for dry active nematics.

### 5.3.2 Spheroids

We next consider spheroidal ellipsoids. They are characterized by the aspect ratio $a/c$ and $a = b$, with $a$, $b$ and $c$ the length of the major axes. Due to the symmetry all geometric properties can be characterized with respect to the polar axis. As the geometry is topologically equivalent to a sphere we expect for passive systems again a minimal energy configuration with four 1/2 disclinations. They still try to maximize their distance, but are now also influenced by local geometric properties. The 1/2 disclinations tend to accumulate in regions of high Gaussian curvature [176, 177]. Computer simulations for thin passive nematic shells have shown that for prolate ellipsoids pairs of defects are located at opposite ends close to the poles. The defects in each pair arrange at opposite sides of the surface and tend to align perpendicular to the pair at the other pole [176]. As the distance between the defects is no longer maximized, the geometric effect seems

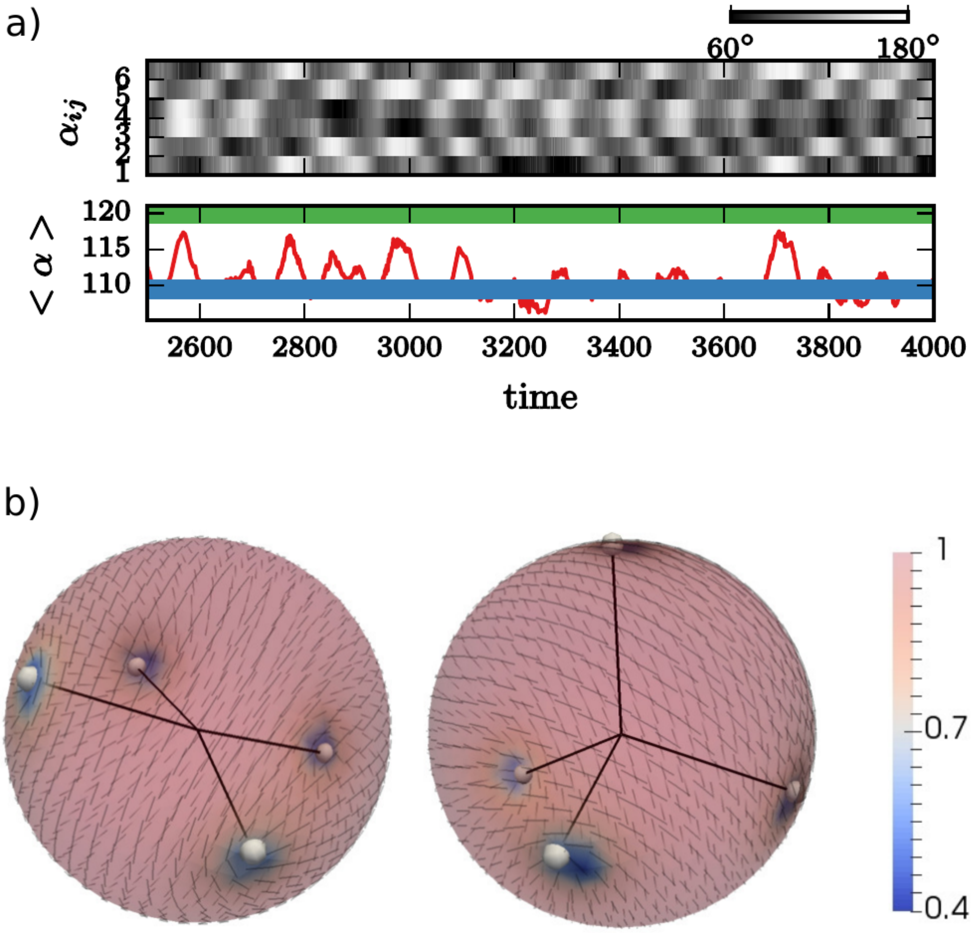

Figure 5.2: (a) Top: Kymograph showing the time evolution of the angles $\alpha_{ij}$. Bottom: Oscillation of the average angle $\langle\alpha\rangle$. The blue and the green lines correspond to the planar ($\langle\alpha\rangle = 120°$) and tetrahedral ($\langle\alpha\rangle = 109,5°$) defect configuration. (b) Snapshots showing the planar and tetrahedral defect configuration within a simulation of 1.000 particles (the four 1/2 disclinations are highlighted, the director field is shown - black lines - and the color coding corresponds to the nematic order parameter $P$, with minima in the four defects). The results are in excellent agreement with the experimental results in [30]

to dominate the repulsion in this case. For oblate ellipsoids the 1/2 disclinations are found near the waist, where the Gaussian curvature is largest. Again two pairs of defects are found, one on each side. They repel each other and are mutually perpendicular to the other pair, leading to an alternating ring of 1/2 disclinations, one above and one below the waist. This behavior seems to be independent of the film thickness [176], we have confirmed this behavior by our surface model without activity.

For active systems we observe again oscillatory behavior, see figure 5.4. For prolate

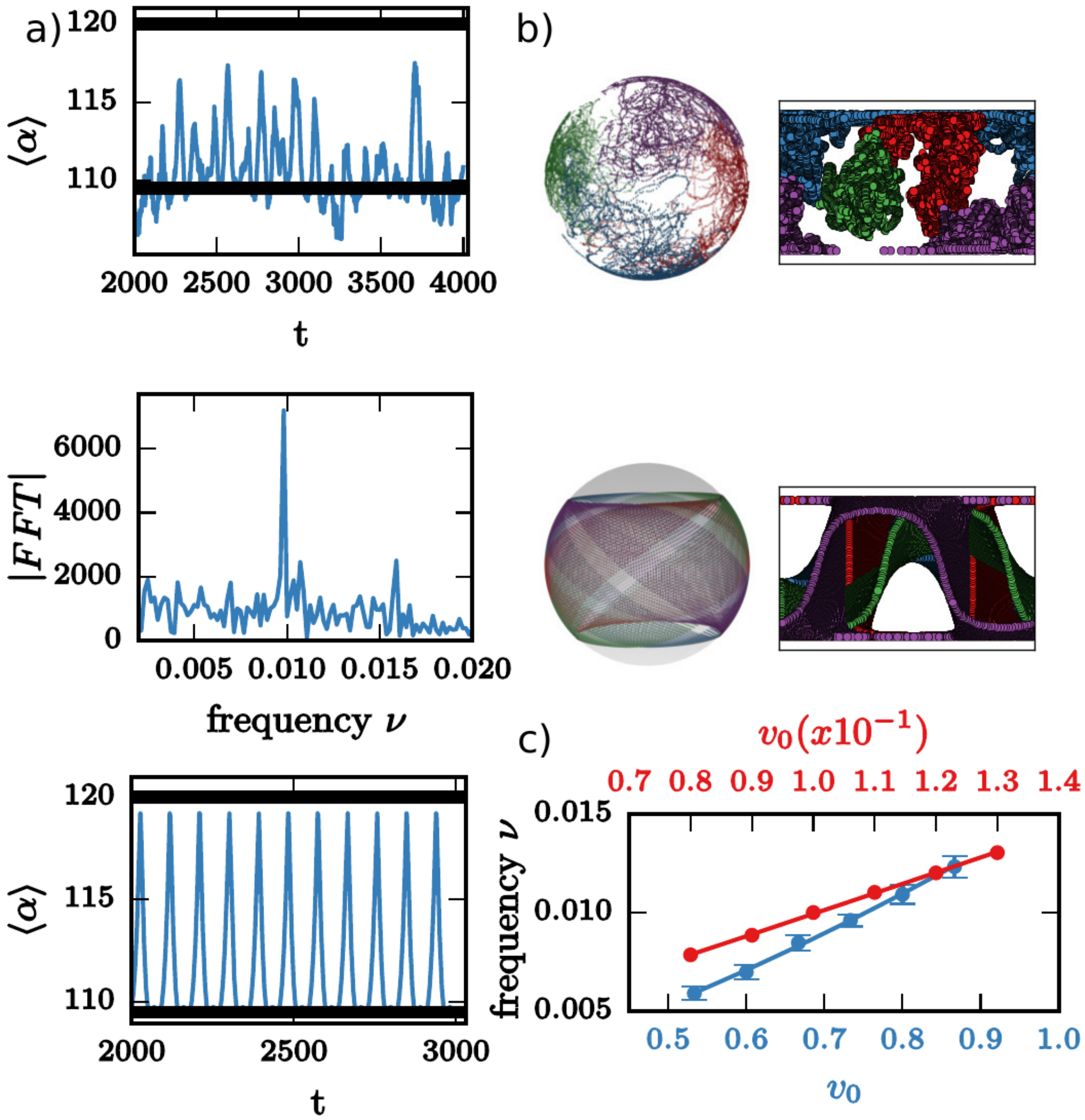

Figure 5.3: (a) Top: Oscillation of the average angle $\langle\alpha\rangle$ from figure 5.2(a), Middle: The power spectrum of $\langle\alpha\rangle$ obtained by using the Fast Fourier Transform (FFT), the peak is associated with the planar-tetrahedral oscillations, Bottom: Oscillation of the average angle $\langle\alpha\rangle$ for four self-propelled particles. (b) Top: Trajectories of the four 1/2 disclinations, each color corresponds to one defect, shown on the sphere and using the Gall-Peters projection, Bottom: same as Top but for the four self-propelled particles. (c) Frequency for the planar-tetrahedral oscillation corresponding to the peak in the power spectrum as a function of the activity for various realizations (blue curve). The trajectories of the four self-propelled particles show a perfect planar-tetrahedral oscillation, the frequency is obtained as the inverse of the distance between consecutive maxima and shown as a function of the self-propulsion velocity (red curve).

spheroids ($a/c < 1$) only two 1/2 disclinations are located at the poles, whereas the other two oscillate around the waist. The oscillations are very noisy and can not be tuned by the activity. Even if the distance between the two 1/2 disclinations at the waist is not optimal the average distance between all four defects is larger than in the passive case. While the 1/2 disclinations are still attracted by the high curvature regions at the poles, the active forces push one of the defects away leading to the observed metastable configuration. Within a transition zone ($a/c \approx 1$) we observe similar behavior as in the spherical case ($a/c = 1$) without any defect localization. The behavior changes for oblate spheroids ($a/c > 1$), where all four 1/2 disclinations are along the waist, maintaining a maximal distance to each other. This behavior is similar to the passive system, but the defects now oscillate between both sides. The frequency of the alternating oscillations above and below the waist can be extracted for various activities. However, a clear functional dependency on the activity could not be found. If the aspect ratio is further increased the situation changes to pairs of 1/2 disclinations which rotate around the umbilical points at the poles. The defects are no longer located at positions of maximal Gaussian curvature. The high curvature value at the waist creates a distortion of the nematic film, which can be seen from the nematic order parameter. It somehow serves as a barrier for the 1/2 disclinations preventing them from crossing the waist. The rotation is a consequence of the activity and the unfavorable short distance with respect to each other. The frequency of the rotation depends on the activity and can be tuned, see figure 5.5. Also the transition to this rotating state depends on the strength of the activity. The stronger the activity, the longer it is possible for the defects to cross the barrier at the waist. A tendency to locate the defects away from the high Gaussian curvature waist can also be seen for the passive case.

The four different regimes are shown in figure 5.6 using the average height $h$ of the defects along the polar axis as the order parameter $\eta = \langle |h| \rangle$. We have $\eta = 1$ if all defects are at the poles, $\eta = 0$ if they are at the waist and $\eta = 0.5$ if they are homogeneously distributed along the polar axis.

Within the coarse-grained description by self-propelled polar particles, using the corresponding self-propulsion velocity according to figure 5.3, we obtain a qualitatively different behavior. Within the considered parameter regime, the values for $\eta$ are independent of the self-propulsion velocity. For aspect ratios $a/c < 0.5$ the particles rotate on closed trajectories, well separated from each other at approximately equal distance along the polar axis. The transition zone with sphere-like behavior is more extended than

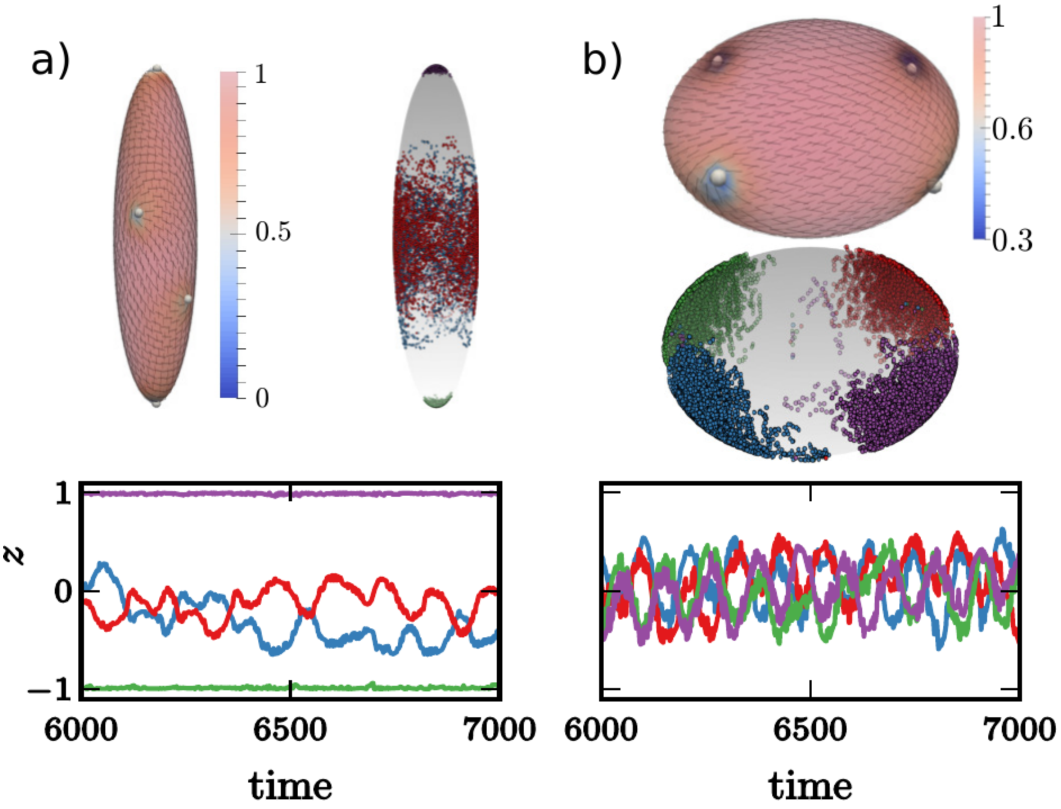

Figure 5.4: (a) Snapshot showing the defect configuration within a simulation of 1.000 particles on a prolate spheroid with $a/c = 0.25$ (the four 1/2 disclinations are highlighted, the director field - black lines - is shown and the color coding corresponds to the nematic order parameter $P$, with minima in the defects). In addition the trajectories of the four 1/2 disclinations are shown (each color corresponds to one defect). The height $h_i$ for each defect with respect to the waist is also shown as a function of time. (b) same as (a) for a oblate spheroid with $a/c = 2$. The oscillations of the four defects have the same frequency and alternate with respect to each other.

for the nematic defects. For $0.5 < a/c < 2$ a band structure is formed around the waist, which shrinks with increasing aspect ratio. For $a/c > 2$ all particles are positioned at the waist, rotating in one direction and maintaining their distance. The regime with pairwise rotating defects around the umbilical points could not be found within the coarse-grained model.

### 5.3.3 Non-spherical ellipsoids

Non-spherical ellipsoids, which are characterized by $a \neq b$, $a \neq c$ and $b \neq c$, have four umbilical points. They are either prolate-like or oblate-like but in any case have two distinct points of maximal Gaussian curvature. We thus analyze the distance of the

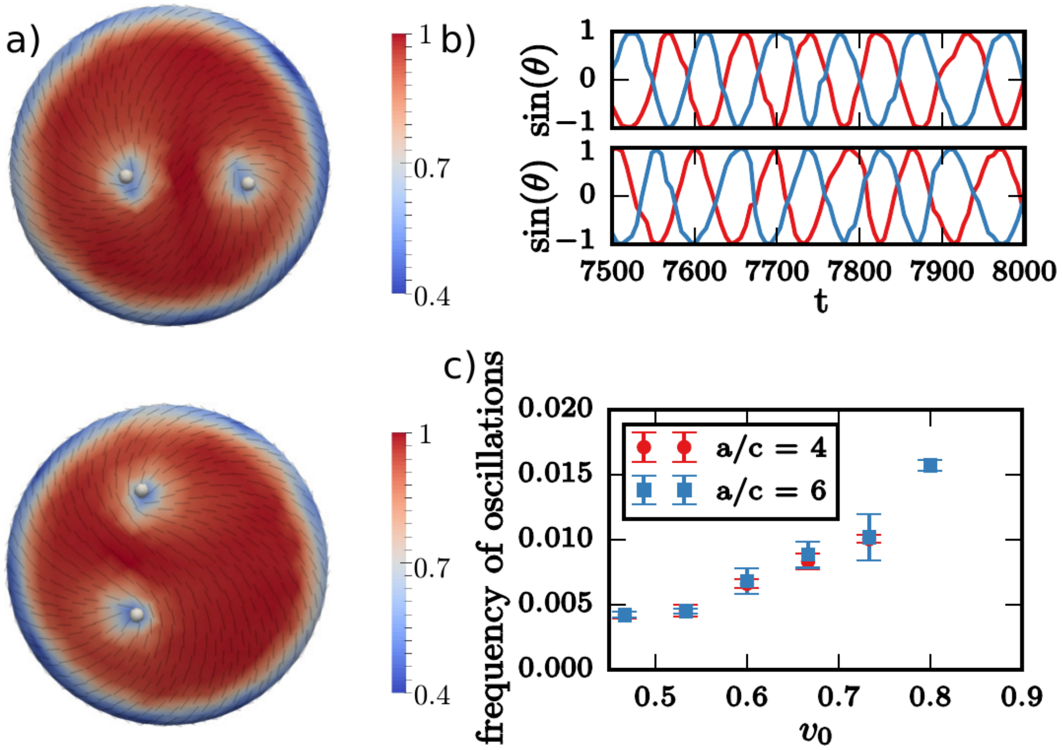

Figure 5.5: (a) Snapshots from above and below showing the defect configuration within a simulation with 1.000 particles on an oblate spheroid with $a/c = 6$ (the four 1/2 disclinations are highlighted, the director field - black lines - is shown and the color coding corresponds to the nematic order parameter $P$, with minima in the defects). (b) Oscillations of the angle measuring the rotation around the umbilical points (top and bottom) and (c) frequency of the oscillation as a function of activity for two different aspect ratios.

four 1/2 disclinations with respect to the umbilical points $\langle DDU\rangle$ and the points of maximal Gaussian curvature $\langle DDG\rangle$ using the average geodesic distances. Figure 5.7, which is inspired by [88], shows the distances as a function of the aspect ratios $a/b$ and $a/c$. Spheroids are also included, the first column shows the previous results for oblate and the diagonal for prolate geometries. Each row in between thus corresponds to a transition from oblate-like to prolate-like geometries. In most cases the 1/2 disclinations are closer to the high Gaussian curvature points than to the umbilical points, with the only exception for oblate-like ellipsoids with a large aspect ration $a/c \geq 4$. This leads to the conclusion that 1/2 disclinations tend to be attracted by points of high Gaussian curvature.

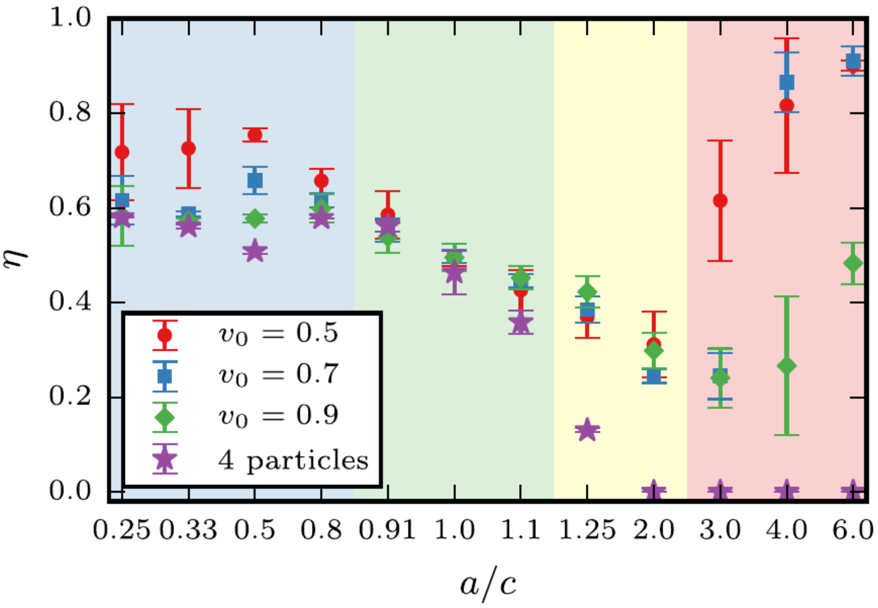

Figure 5.6: Phase diagram for patterns and oscillations on spheroidal ellipsoids for 1/2 disclinations and self-propelled particles. The results for the coarse-grained description by self-propelled particles are independent of the activity in the corresponding regime to the considered velocities $v_0$. From left to right we have (blue) the situation for prolate shapes with location of two defects at the poles, leading to $\eta > 0.5$, (green) spherical like shapes with no clear location of the defects, leading to $\eta \approx 0.5$, (yellow) oblate shapes with location of the defects along the waist, leading to $\eta < 0.5$, (red) for larger $a/c$ we obtain a phase transition towards the rotating state, with the defects located around the poles, leading to $\eta > 0.5$. The transition towards this state depends on the activity.

### 5.3.4 Torus

We now want to see the effects that changing topology has on the system. For this reason, we constraint the self-propelled particles to a toroidal surface of major and minor radius $R = 21.8$ and $r = 14.6$, respectively. These parameters correspond to a surface area of the torus that is equivalent to the surface area of the spheroids considered above. The number of particles is also in this case $N \simeq 1000$. The holonomic constraint in equation (5.1) in this case reads: $g(\boldsymbol{q}_i) = \left(\sqrt{q_{i,1}^2 + q_{i,2}^2} - R\right)^2 + q_{i,3}^2 - r^2$. The toroidal surface differs from the spheroids previously considered because it has a genus $g(\mathcal{S}) = 1$. Broadly speaking, the genus of a surface is the number of holes it has. All the spheroids considered above have therefore a genus equal to zero. It is in this respect that we can say that the torus has a different topology. This fact has an important consequence for the defects in the orientation fields. In fact, according to the Poincaré-Hopf theorem, it it

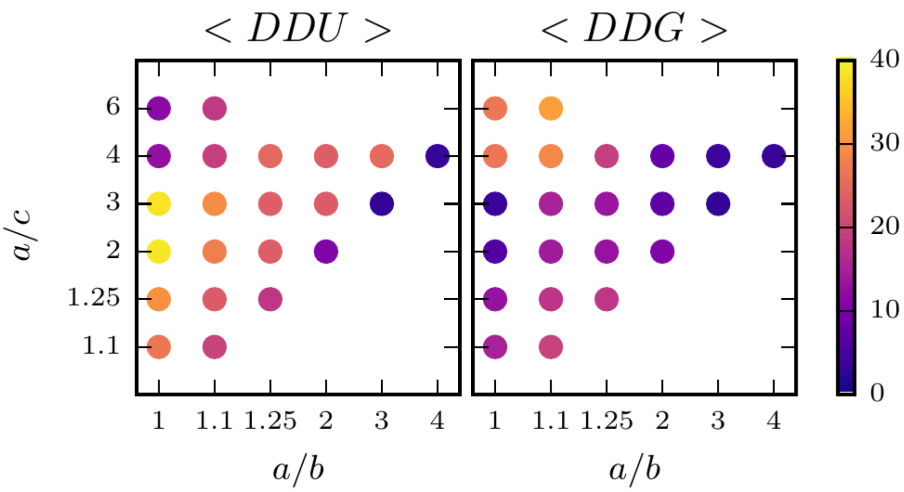

Figure 5.7: Average geodesic distance of 1/2 disclinations to the umbilical points $\langle DDU \rangle$ (left) and to the points of maximal Gaussian curvature $\langle DDG \rangle$ (right) for non-spheroidal and spheroidal (first column - oblate and diagonal - prolate) ellipsoids of different aspect ratio. Only for the extreme case of $a/c = 4, 6$ and $a/b = 1.1$ the disclinations are closer to the umbilical points. Also in these cases a rotating state as in figure 5.5 can be observed, which however is not as regular. In all other situations the disclinations are closer to the points of maximal Gaussian curvature.

possible to cover a surface with genus equal to one without generating any defects. In [83], it has however being experimentally shown that in active nematic toroids there are pairs of defects of opposite sign (i.e. $+1/2$ and $-1/2$ defects) that unbind and segregate in regions of opposite Gaussian curvature. We simulated active nematic particles on a toroidal surface and observed if defects of opposite sign arise. In figure 5.8 we show two snapshots of the resulting simulation, taken at different time. In both cases, a positive (yellow circle) and a negative (green triangle) defects are found, located in the regions of positive and negative Gaussian curvature, respectively. We observe that this effect is still present for different major and minor radius $R$ and $r$. A more quantitative analysis is needed in order to address questions such as the role of the activity strength, the number of defects pair present in the system and a relation between the exact defect position and the value of the Gaussian curvature. However, figure 5.8 already shows that numerical simulations of active nematics on a toroidal surface obtained using equations (5.1) and (5.3) are in agreement with the experimental data observed in [83].

Even more interesting is the case of polar active particles on a toroidal geometry, shown in figure 5.9. Numerical simulations show that the polar particles rotate along the toroidal direction in a counter-clockwise direction (panel a). They then collectively

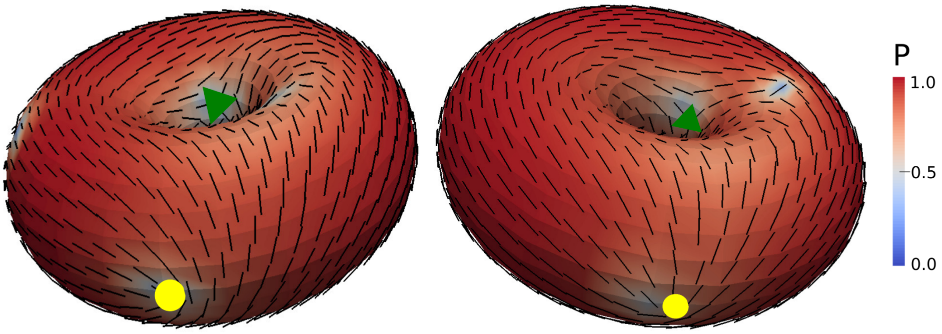

Figure 5.8: Snapshots taken at different time showing a simulation of 1.000 active nematic particles on a toroidal geometry with $R = 21.8$ and $r = 14.6$. The color coding corresponds to the nematic order parameter $P$ and the black lines represents the director field. $+1/2$ ($-1/2$) defects are shown as yellow circle (green triangle).

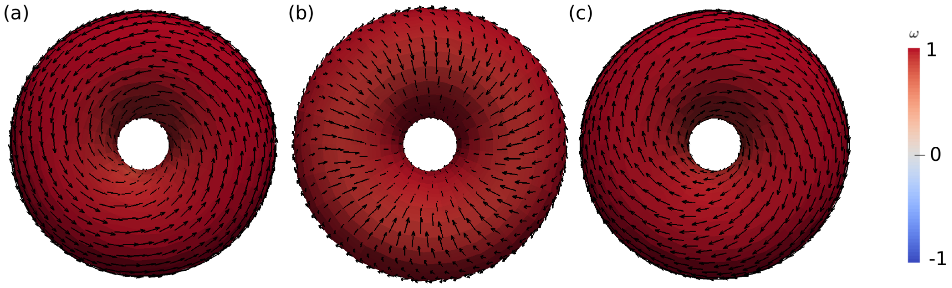

Figure 5.9: Snapshots taken at different time showing a simulation of 1.000 active polar particles on a toroidal geometry with $R = 21.8$ and $r = 14.6$. The particles rotate along the toroidal direction in a counter-clockwise (a) or clockwise (c) direction. They shortly align along the poloidal direction when collectively changing direction (b). The color coding corresponds to the polar order parameter $\omega$ and the black arrows represent the particle directions.

change direction by orienting themselves along the poloidal direction (panel b), before starting rotating again along the toroidal direction in a clockwise direction (panel c). This cycle repeats itself over and over.

In summary, in [83] the localization of positive and negative defects on regions of positive and negative curvature respectively has been experimentally observed for an active nematic toroid. We could confirm this result within our model, see figure 5.8, even though a more exhaustive analysis is needed. We treated the polar case as well, where no defects were present in the system. We found an oscillating state, where the polar particles rotate along the toroidal direction of the torus, changing direction at regular intervals. Both these effects show the richness of phenomena that is possible to discover in topological active matter and, together with the study of surfaces of different topology, such as a 2- or 3-torus, should be explored further.

## 5.4 Summary

In [30] it was shown that in a confined active system, namely a dense suspension of microtubules and molecular motors on the surface of a spherical lipid vesicle, cyclic oscillations between defect configurations can be observed. They result from topological constraints and the coupling between velocity fields and defect-defect interactions. Our work extends the understanding of the delicate relations between topology, geometry and defect dynamics on non-spherical shapes for the system considered in [30]. We are concerned with ellipsoidal surfaces and identify crucial geometric features which influence collective motion patterns in active nematic films. We have shown that 1/2 disclinations are related to both, maxima in the Gaussian curvature and umbilical points of the surface. On prolate spheroids maxima in Gaussian curvature and umbilical points coincide, they are located at the two poles and attract the 1/2 disclinations. However, the repulsive defect-defect interaction allows only two of the defects to be located at the poles, the other two try to maximize their distance and are located around the waist, where they oscillate. Spherical like shapes lead to similar behavior as observed on a sphere, with no distinguished location of the defects and an oscillation between a tetrahedral and planar defect configuration. For oblate spheroids all 1/2 disclinations are located at the waist, the region of high Gaussian curvature. They again maximize their distance and oscillate. With increasing aspect ratio $a/c$ the situation changes. The defects can no longer cross the waist, where the high Gaussian curvature leads to a distortion of the nematic order. As a consequence pairs of 1/2 disclinations rotate around the umbilical points. The frequency of the rotation depends on the activity and can be tuned. This found rotating state is an other step towards a controllable transformation of chemical into mechanical energy in nanoscale active matter and asks for experimental validation. The results for non-spheroidal ellipsoids confirm these findings, even if the separation of the different states is not as distinct as in figure 5.6. A smooth transition of the dynamics between prolate-like and oblate-like shapes is identified in figure 5.7 with a clear tendency of the 1/2 disclinations to locate at points of maximal Gaussian curvature. Only for extreme values of $a/c$ and almost spheroidal shapes the situation changes and the rotating state around the umbilical points could be identified.

We have further demonstrated that the proposed coarse-grained description of 1/2 disclinations in active nematic matter by self-propelled particles fails if geometric properties come into play. Already on spherical shapes the trajectories of the defects and the self-propelled particles differ significantly and on spheroidal ellipsoids both descriptions do not even qualitatively agree.

We have also seen the effects that changing topology has on the system by simulating nematic and polar active particles on a toroidal surface. In this case, the presence of defects is not dictated by the Poincaré-Hopf theorem and this is what we observed for polar particles. However, for nematic particles we observed pairs of $+1/2$ and $-1/2$ defects that are localized in regions of opposite Gaussian curvature, as observed experimentally in [83].

In summary, in this chapter we explored the complex interaction of topology, geometry and defect dynamics in nematic films on ellipsoidal surfaces and demonstrated how topological constraints and geometric properties can be used to control the collective behavior in nanoscale active matter. The non-linear coupling between non-constant Gaussian curvature and defect-defect interactions leads to tunable spatiotemporal patterns. Among these findings is a stable rotating state on strongly oblate-like ellipsoids, which suggests an other pathway towards a controllable generation of mechanical work in nanoscale active matter. The richness of physics observed in our work will further increase if the underlying shape is deformable. First experimental results of such an interplay between activity-driven defect motion and deformability of the vesicle are already shown in [30] and discussed in [178]. However, for theoretical descriptions of these phenomena new methods will be required.

# Conclusions

Different theoretical methods have been proposed to model the many collective phenomena that characterize the field of active matter. Agent-based models are very common, thanks to their efficiency. However with these methods the physical internal processes are lost, as well as the deformations of the particles. On the other side, we have microscopic phase field modeling, which offers a very detailed physical description, but its computational capabilities are limited to a small number of particles.

In chapter 3 we proposed a microscopic field-theoretical approach that fills the gap between agent-based model and microscopic phase field descriptions of active matter. This model combines the phase field crystal method with a polar order parameter and a self-propulsion term. It can therefore be thought as a phase field crystal modeling of active matter. We have shown that this model can be used to describe different known collective phenomena in active matter, such as vortex formation and collective migration. Thanks to a parallel finite element implementation, it has been possible to simulate thousands of active particles. This helped us to shed some light on the coarsening process that lead to collective migration and to the mechanisms behind the formation of mobile clusters.

An extension towards binary mixtures of interacting active and passive particles was possible with the aid of the binary phase field crystal method. In this case, we explored the phenomenon of enhanced crystallization of passive particles via active doping, quantitatively reproducing experimental results. During the study of head-on collision between a passive and an active particle we were able to identify a single parameter controlling the mobility of passive particles. We exploited this fact to show that collective migration is suppressed in an active bath in the presence of fixed obstacles. In the more interesting case of mobile passive particles, we were able to offer a theoretical prediction that can be validated experimentally, namely the existence of a state where the alignment between the active particles is globally nematic, but polar within each lane, known as laning state.

Topological active matter is a field that studies the interplay between curvature, activity and topology. In chapter 5 we developed a minimal model to describe active nematic particles on curved surfaces and we have analyzed the spatiotemporal patterns that emerge in the defects dynamics. For the case of a sphere, we could reproduce oscillations between different configurations that were observed experimentally [30]. For the case of an ellipsoid, we studied the connection between the defects location and geometric properties of the surface, such as Gaussian curvature and umbilical points.

It would be interesting to link the phase field crystal approach to active matter that we introduced in this thesis to the field of topological active matter explored in chapter 5. Steps have been made in this directions in [90], where a polar active crystal on a sphere has been studied using a phase field crystal approach. Even more interesting would be an extension towards nematic symmetry, thus confirming our findings of chapter 5 about dry active nematics on surfaces. Such a model would provide a powerful tool to theoretically study the dynamics of active systems on *deformable* surfaces, especially considering that experimental results on deformable surfaces have already been obtained [30].

In [40] a fully continuous model to describe (passive) suspensions have been developed by coupling the phase field crystal method with the Navier-Stokes equation. It is therefore tempting to couple the active vacancy phase field crystal model with the Navier-Stokes equation, thus describing active suspensions. In this way it would be possible to obtain a better understanding of the interplay between activity and hydrodynamic interactions.

# Acknowledgements

In the spirit of this thesis, I will keep also this section short. Therefore I would like to thank all the people involved, directly or indirectly, in this thesis. In particular, the people at the Institute of Scientific Computing, where I spent the last years working on this thesis. Among them a special thanks goes to Simon Praetorius, Axel Voigt, Marco Salvalaglio, Christian Köhler, Sebastian Aland, Sebastian Reuther, Wieland Marth, Rainer Backofen, Florian Stenger, Siqi Ling and Dennis Wenzel. Thanks also to the European Union (ERDF) and the Free State of Saxony via the ESF project 100231947 (Young Investigatorts Group Computer Simulations for Materials Design—CoSiMa) and to Florian Pump for coordinating it. To Valentina, for always proofreading everything I sent her. To Fabio, Piotr, Mathias and Folke for having shared a few bike rides with me during this time and to Amayra for being a nice and fun flatmate. Finally, to Juliane, and my parents, Paola and Aurelio.

# Bibliography

[1] M. C. Marchetti *et al.* Hydrodynamics of soft active matter. *Rev. Mod. Phys.*, 85: 1143–1189, 2013.

[2] S. Ramaswamy. The mechanics and statistics of active matter. *Annu. Rev. Condens. Matter Phys.*, 1:323–345, 2010.

[3] M. Cates. Diffusive transport without detailed balance in motile bacteria: does microbiology need statistical physics? *Rep. Prog. Phys.*, 75:042601, 2012.

[4] A. Cavagna *et al.* Scale-free correlations in starling flocks. *Proc. Natl. Acad. Sci. U. S. A.*, 107:11865–11870, 2010.

[5] H. Wensink *et al.* Meso-scale turbulence in living fluids. *Proc. Natl. Acad. Sci. U. S. A.*, 109:14308, 2012.

[6] P. M. Chaikin and T. C. Lubensky. *Principles of condensed matter physics*. 2000.

[7] R. Zwanzig. *Nonequilibrium Statistical Mechanics*. 2001.

[8] J. Toner and Y. Tu. Long-range order in a two-dimensional dynamical XY model: How birds fly together. *Phys. Rev. Lett.*, 75:4326–4329, 1995.

[9] J. Toner and Y. Tu. Flocks, herds, and schools: A quantitative theory of flocking. *Phys. Rev. E,* 58:4828–4858, 1998.

[10] J. Toner, Y. Tu and S. Ramaswamy. Hydrodynamics and phases of flocks. *Ann. Phys.*, 318:170–244, 2005.

[11] K. Kruse *et al.* Asters, vortices, and rotating spirals in active gels of polar filaments. *Phys. Rev. Lett.*, 92:078101, 2004.

[12] J.-F. Joanny and J. Prost. Active gels as a description of the actin-myosin cytoskeleton. *HFSP journal*, 3:94–104, 2009.

[13] J. Prost, F. Jülicher and J.-F. Joanny. Active gel physics. *Nat. Phys.*, 11:111, 2015.

[14] T. Vicsek *et al.* Novel type of phase transition in a system of self-driven particles. *Phys. Rev. Lett.*, 75:1226–1229, 1995.

[15] D. Grossman, I. S. Aranson and E. Ben Jacob. Emergence of agent swarm migration and vortex formation through inelastic collisions. *New J. Phys.*, 10:023036, 2008.

[16] A. M. Menzel and T. Ohta. Soft deformable self-propelled particles. *EPL (Europhysics Letters)*, 99:58001, 2012.

[17] F. Peruani, A. Deutsch and M. Bär. Nonequilibrium clustering of self-propelled rods. *Phys. Rev. E*, 74:030904, 2006.

[18] Y. Fily and M. C. Marchetti. Athermal phase separation of self-propelled particles with no alignment. *Phys. Rev. Lett.*, 108:235702, 2012.

[19] M. E. Cates and J. Tailleur. Motility-induced phase separation. *Annu. Rev. Condens. Matter Phys.*, 6:219–244, 2015.

[20] M. Cates and J. Tailleur. When are active brownian particles and run-and-tumble particles equivalent? consequences for motility-induced phase separation. *EPL (Europhysics Letters)*, 101:20010, 2013.

[21] G. S. Redner, M. F. Hagan and A. Baskaran. Structure and dynamics of a phase-separating active colloidal fluid. *Phys. Rev. Lett.*, 110:055701, 2013.

[22] B. Szabó *et al.* Phase transition in the collective migration of tissue cells: Experiment and model. *Phys. Rev. E*, 74:061908, 2006.

[23] J. Löber, F. Ziebert and I. S. Aranson. Collisions of deformable cells lead to collective migration. *Sci. Rep.*, 5:9172, 2015.

[24] W. Marth and A. Voigt. Collective migration under hydrodynamic interactions: a computational approach. *Interface Focus,* 6:20160037, 2016.

[25] A. M. Menzel and H. Löwen. Traveling and resting crystals in active systems. *Phys. Rev. Lett.*, 110:055702, 2013.

[26] A. M. Menzel, T. Ohta and H. Löwen. Active crystals and their stability. *Phys. Rev. E*, 89:022301, 2014.

[27] K. R. Elder, M. Katakowski, M. Haataja and M. Grant. Modeling elasticity in crystal growth. *Phys. Rev. Lett.*, 88:245701, 2002.

[28] K. R. Elder and M. Grant. Modeling elastic and plastic deformations in nonequilibrium processing using phase field crystals. *Phys. Rev. E*, 70:051605, 2004.

[29] F. Alaimo, S. Praetorius and A. Voigt. A microscopic field theoretical approach for active systems. *New J. Phys.*, 18:083008, 2016.

[30] F. C. Keber *et al.* Topology and dynamics of active nematic vesicles. *Science*, 345: 1135–1139, 2014.

[31] R. Backofen and A. Voigt. A phase-field-crystal approach to critical nuclei. *J. Phys.: Condens. Matter*, 22:364104, 2010.

[32] G. I. Tóth *et al.* Polymorphism, crystal nucleation and growth in the phase-field crystal model in 2d and 3d. *J. Phys.: Condens. Matter*, 22:364101, 2010.

[33] S. Tang *et al.* Three-dimensional phase-field crystal modeling of fcc and bcc dendritic crystal growth. *J. Cryst. Growth*, 334:146–152, 2011.

[34] K. R. Elder *et al.* Phase-field crystal modeling and classical density functional theory of freezing. *Phys. Rev. B*, 75:064107, 2007.

[35] S. van Teeffelen, R. Backofen, A. Voigt and H. Löwen. Derivation of the phase-field-crystal model for colloidal solidification. *Phys. Rev. E*, 79:051404, 2009.

[36] J. Swift and P. C. Hohenberg. Hydrodynamic fluctuations at the convective instability. *Phys. Rev. A*, 15:319–328, 1977.

[37] K.-A. Wu and P. W. Voorhees. Stress-induced morphological instabilities at the nanoscale examined using the phase field crystal approach. *Phys. Rev. B*, 80: 125408, 2009.

[38] P. Y. Chan, N. Goldenfeld and J. Dantzig. Molecular dynamics on diffusive time scales from the phase-field-crystal equation. *Phys. Rev. E*, 79:035701, 2009.

[39] P. Y. Chan. *Scaling and Pattern Formation in Condensed Matter Systems*. PhD thesis, University of Illinois at Urbana-Champaign, 2007.

[40] S. Praetorius and A. Voigt. A navier-stokes phase-field crystal model for colloidal suspensions. *J. Chem. Phys.*, 142:154904, 2015.

[41] U. Thiele *et al.* Localized states in the conserved Swift-Hohenberg equation with cubic nonlinearity. *Phys. Rev. E*, 87:042915, 2013.

[42] M. J. Robbins, A. J. Archer, U. Thiele and E. Knobloch. Modeling the structure of liquids and crystals using one- and two-component modified phase-field crystal models. *Phys. Rev. E*, 85:061408, 2012.

[43] T. V. Ramakrishnan and M. Yussouff. First-principles order-parameter theory of freezing. *Phys. Rev. B*, 19:2775–2794, 1979.

[44] B. D. Goddard *et al.* Unification of dynamic density functional theory for colloidal fluids to include inertia and hydrodynamic interactions: derivation and numerical experiments. *J. Phys.: Condens. Matter*, 25:035101, 2013.

[45] G. I. Tóth, L. Gránásy and G. Tegze. Nonlinear hydrodynamic theory of crystallization. *J. Phys.: Condens. Matter*, 26:055001, 2014.

[46] V. Heinonen *et al.* Consistent hydrodynamics for phase field crystals. *Phys. Rev. Lett.*, 116:024303, 2016.

[47] H. Tanaka and T. Araki. Simulation method of colloidal suspensions with hydrodynamic interactions: Fluid particle dynamics. *Phys. Rev. Lett.*, 85:1338–1341, 2000.

[48] S. Praetorius. *Efficient Solvers for the Phase-Field Crystal Equation - Development and Analysis of a Block-Preconditioner*. PhD thesis, Technische Universität Dresden, 2015.

[49] M. Roche. Rosenbrock methods for differential algebraic equations. *Numerische Mathematik*, 52:45–63, 1987.

[50] M. Cheng and J. A. Warren. An efficient algorithm for solving the phase field crystal model. *J. Comput. Phys.*, 227:6241–6248, 2008.

[51] A. Baskaran *et al.* Energy stable and efficient finite-difference nonlinear multigrid schemes for the modified phase field crystal equation. *J. Comput. Phys.*, 250: 270–292, 2013.

[52] H. Cao and Z. Sun. Two finite difference schemes for the phase field crystal equation. *Science China Mathematics*, 58:2435–2454, 2015.

[53] Z. Hu, S. M. Wise, C. Wang and J. S. Lowengrub. Stable and efficient finite-difference nonlinear-multigrid schemes for the phase field crystal equation. *J. Comput. Phys.*, 228:5323–5339, 2009.

[54] G. Tegze *et al.* Advanced operator splitting-based semi-implicit spectral method to solve the binary phase-field crystal equations with variable coefficients. *J. Comput. Phys.*, 228:1612–1623, 2009.

[55] M. Elsey and B. Wirth. A simple and efficient scheme for phase field crystal simulation. *ESAIM: Math. Model. Num.*, 47:1413–1432, 2013.

[56] S. Vey and A. Voigt. Amdis: adaptive multidimensional simulations. *Comput. Visualization Sci.*, 10:57–67, 2007.

[57] T. Witkowski, S. Ling, S. Praetorius and A. Voigt. Software concepts and numerical algorithms for a scalable adaptive parallel finite element method. *Adv. Comput. Math.*, 41:1145–1177, 2015.

[58] S. Ling. *Solving multi-physics problems using adaptive finite elements with independently refined meshes*. PhD thesis, Technische Universität Dresden, 2016.

[59] C. Bechinger *et al.* Active particles in complex and crowded environments. *Rev. Mod. Phys.*, 88:045006, 2016.

[60] A. Zöttl and H. Stark. Emergent behavior in active colloids. *J. Phys.: Condens. Matter*, 28:253001, 2016.

[61] A. Peshkov, E. Bertin, F. Ginelli and H. Chaté. Boltzmann-Ginzburg-Landau approach for continuous descriptions of generic vicsek-like models. *Eur. Phys. J. Spec. Top.*, 223:1315–1344, 2014.

[62] F. Peruani *et al.* Collective motion and nonequilibrium cluster formation in colonies of gliding bacteria. *Phys. Rev. Lett.*, 108:098102, 2012.

[63] A. Sokolov and I. S. Aranson. Reduction of viscosity in suspension of swimming bacteria. *Phys. Rev. Lett.*, 103:148101, 2009.

[64] H.-P. Zhang, A. Be'er, E.-L. Florin and H. L. Swinney. Collective motion and density fluctuations in bacterial colonies. *Proc. Natl. Acad. Sci. U. S. A.*, 107:13626–13630, 2010.

[65] W. F. Paxton *et al.* Catalytic nanomotors: autonomous movement of striped nanorods. *J. Am. Chem. Soc.*, 126:13424–13431, 2004.

[66] B. A. Camley and W.-J. Rappel. Physical models of collective cell motility: from cell to tissue. *J. Phys. D*, 50:113002, 2017.

[67] T. Vicsek and A. Zafeiris. Collective motion. *Phys. Rep.*, 517:71–140, 2012.

[68] W. Marth, S. Praetorius and A. Voigt. A mechanism for cell motility by active polar gels. *J. R. Soc. Interface*, 12:20150161, 2015.

[69] E. Tjhung, D. Marenduzzo and M. E. Cates. Spontaneous symmetry breaking in active droplets provides a generic route to motility. *Proc. Natl. Acad. Sci. U. S. A.*, 109:12381–12386, 2012.

[70] S. Ramaswamy, R. A. Simha and J. Toner. Active nematics on a substrate: giant number fluctuations and long-time tails. *EPL (Europhysics Letters)*, 62:196, 2003.

[71] V. Narayan, S. Ramaswamy and N. Menon. Long-lived giant number fluctuations in a swarming granular nematic. *Science*, 317:105–108, 2007.

[72] H. Chaté, F. Ginelli and R. Montagne. Simple model for active nematics: quasi-long-range order and giant fluctuations. *Phys. Rev. Lett.*, 96:180602, 2006.

[73] P. G. de Gennes and J. Prost. *The physics of liquid crystals*. 1993.

[74] E. Lauga and T. R. Powers. The hydrodynamics of swimming microorganisms. *Rep. Prog. Phys.*, 72:096601, 2009.

[75] A. Baskaran and M. C. Marchetti. Statistical mechanics and hydrodynamics of bacterial suspensions. *Proc. Natl. Acad. Sci. U. S. A.*, 106:15567–15572, 2009.

[76] J. Elgeti, R. G. Winkler and G. Gompper. Physics of microswimmers—single particle motion and collective behavior: a review. *Rep. Prog. Phys.*, 78:056601, 2015.

[77] Y. Hatwalne, S. Ramaswamy, M. Rao and R. A. Simha. Rheology of active-particle suspensions. *Phys. Rev. Lett.*, 92:118101, 2004.

[78] I. Buttinoni *et al.* Dynamical clustering and phase separation in suspensions of self-propelled colloidal particles. *Phys. Rev. Lett.*, 110:238301, 2013.

[79] E. Lushi and C. S. Peskin. Modeling and simulation of active suspensions containing large numbers of interacting micro-swimmers. *Comput. Struct.*, 122:239–248, 2013.

[80] E. Lushi, H. Wioland and R. E. Goldstein. Fluid flows created by swimming bacteria drive self-organization in confined suspensions. *Proc. Natl. Acad. Sci. U. S. A.*, 111: 9733–9738, 2014.

[81] L. S. Penrose. Dermatoglyphic topology. *Nature*, 205:544–546, 1965.

[82] A. Doostmohammadi, S. P. Thampi and J. M. Yeomans. Defect-mediated morphologies in growing cell colonies. *Phys. Rev. Lett.*, 117:048102, 2016.

[83] P. W. Ellis *et al.* Curvature-induced defect unbinding and dynamics in active nematic toroids. *Nat. Phys.*, 14:85, 2018.

[84] F. Alaimo, C. Köhler and A. Voigt. Curvature controlled defect dynamics in topological active nematics. *Sci. Rep.*, 7:5211, 2017.

[85] S. Henkes, M. C. Marchetti and R. Sknepnek. Dynamical patterns in nematic active matter on a sphere. *Phys. Rev. E,* 97:042605, 2018.

[86] R. Zhang, Y. Zhou, M. Rahimi and J. J. De Pablo. Dynamic structure of active nematic shells. *Nat. Commun.*, 7:13483, 2016.

[87] R. Sknepnek and S. Henkes. Active swarms on a sphere. *Phys. Rev. E*, 91:022306, 2015.

[88] S. Ehrig, J. Ferracci, R. Weinkamer and J. W. C. Dunlop. Curvature-controlled defect dynamics in active systems. *Phys. Rev. E*, 95:062609, 2017.

[89] S. Shankar, M. J. Bowick and M. C. Marchetti. Topological sound and flocking on curved surfaces. *Phys. Rev. X,* 7:031039, 2017.

[90] S. Praetorius, A. Voigt, R. Wittkowski and H. Löwen. Active crystals on a sphere. *Phys. Rev. E*, 97:052615, 2018.

[91] I. Nitschke *et al.* Nematic liquid crystals on curved surfaces: a thin film limit. *Proc. R. Soc. A*, 474:20170686, 2018.

[92] M. Nestler, I. Nitschke, S. Praetorius and A. Voigt. Orientational order on surfaces: The coupling of topology, geometry, and dynamics. *J. Nonlinear Sci.*, 28:147–191, 2018.

[93] J. Stenhammar, D. Marenduzzo, R. J. Allen and M. E. Cates. Phase behaviour of active brownian particles: the role of dimensionality. *Soft Matter*, 10:1489–1499, 2014.

[94] J. Stenhammar *et al.* Continuum theory of phase separation kinetics for active brownian particles. *Phys. Rev. Lett.*, 111:145702, 2013.

[95] L. M. Janssen, A. Kaiser and H. Löwen. Aging and rejuvenation of active matter under topological constraints. *Sci. Rep.*, 7:5667, 2017.

[96] P. Romanczuk *et al.* Active brownian particles. *Eur. Phys. J. Spec. Top.*, 202:1–162, 2012.

[97] U. Erdmann, W. Ebeling, L. Schimansky-Geier and F. Schweitzer. Brownian particles far from equilibrium. *Eur. Phys. J. B*, 15:105–113, 2000.

[98] A. Martín-Gómez, D. Levis, A. Díaz-Guilera and I. Pagonabarraga. Collective motion of active brownian particles with polar alignment. *Soft Matter*, 14:2610–2618, 2018.

[99] C. W. Reynolds. Flocks, herds and schools: A distributed behavioral model. In *ACM SIGGRAPH computer graphics*, volume 21, 1987, pages 25–34.

[100] F. Ginelli. The physics of the Vicsek model. *Eur. Phys. J. Spec. Top.*, 225:2099–2117, 2016.

[101] H. Chaté, F. Ginelli, G. Grégoire and F. Raynaud. Collective motion of self-propelled particles interacting without cohesion. *Phys. Rev. E*, 77:046113, 2008.

[102] N. D. Mermin and H. Wagner. Absence of ferromagnetism or antiferromagnetism in one-or two-dimensional isotropic heisenberg models. *Phys. Rev. Lett.*, 17:1133, 1966.

[103] G. Grégoire and H. Chaté. Onset of collective and cohesive motion. *Phys. Rev. Lett.*, 92:025702, 2004.

[104] F. Ginelli, F. Peruani, M. Bär and H. Chaté. Large-scale collective properties of self-propelled rods. *Phys. Rev. Lett.*, 104:184502, 2010.

[105] P. C. Martin, O. Parodi and P. S. Pershan. Unified hydrodynamic theory for crystals, liquid crystals, and normal fluids. *Phys. Rev. A*, 6:2401–2420, 1972.

[106] D. Forster. *Hydrodynamic fluctuations, broken symmetry, and correlation functions*. 1975.

[107] E. Bertin, M. Droz and G. Grégoire. Boltzmann and hydrodynamic description for self-propelled particles. *Phys. Rev. E*, 74:022101, 2006.

[108] E. Bertin, M. Droz and G. Grégoire. Hydrodynamic equations for self-propelled particles: microscopic derivation and stability analysis. *J. Phys. A*, 42:445001, 2009.

[109] T. Ihle. Kinetic theory of flocking: Derivation of hydrodynamic equations. *Phys. Rev. E*, 83:030901, 2011.

[110] A. Baskaran and M. C. Marchetti. Nonequilibrium statistical mechanics of self-propelled hard rods. *J. Stat. Mech.*, 2010:P04019, 2010.

[111] A. Baskaran and M. C. Marchetti. Enhanced diffusion and ordering of self-propelled rods. *Phys. Rev. Lett.*, 101:268101, 2008.

[112] A. Baskaran and M. C. Marchetti. Hydrodynamics of self-propelled hard rods. *Phys. Rev. E*, 77:011920, 2008.

[113] L.-Q. Chen. Phase-field models for microstructure evolution. *Annu. Rev. Mater. Res.*, 32:113–140, 2002.

[114] B. Li, J. Lowengrub, A. Ratz and A. Voigt. Geometric evolution laws for thin crystalline films: modeling and numerics. *Commun. Comput. Phys.*, 6:433, 2009.

[115] A. Mogilner and K. Keren. The shape of motile cells. *Curr. Biol.*, 19:R762–R771, 2009.

[116] M. Abercrombie. The crawling movement of metazoan cells. *Proc. R. Soc. London B*, 207:129–147, 1980.

[117] L. Blanchoin, R. Boujemaa-Paterski, C. Sykes and J. Plastino. Actin dynamics, architecture, and mechanics in cell motility. *Physiol. Rev.*, 94:235–263, 2014.

[118] U. S. Schwarz and S. A. Safran. Physics of adherent cells. *Rev. Mod. Phys.*, 85: 1327–1381, 2013.

[119] D. Shao, H. Levine and W.-J. Rappel. Coupling actin flow, adhesion, and morphology in a computational cell motility model. *Proc. Natl. Acad. Sci. U. S. A.*, 109: 6851–6856, 2012.

[120] P. Friedl and K. Wolf. Tumour-cell invasion and migration: diversity and escape mechanisms. *Nat. Rev. Cancer*, 3:362, 2003.

[121] W. Marth. *Hydrodynamic diffuse interface models for cell morphology and motility*. PhD thesis, Technische Universität Dresden, 2016.

[122] E. Tjhung, M. E. Cates and D. Marenduzzo. Nonequilibrium steady states in polar active fluids. *Soft Matter*, 7:7453–7464, 2011.

[123] J. Löber, F. Ziebert and I. S. Aranson. Modeling crawling cell movement on soft engineered substrates. *Soft matter*, 10:1365–1373, 2014.

[124] E. Tjhung, A. Tiribocchi, D. Marenduzzo and M. Cates. A minimal physical model captures the shapes of crawling cells. *Nat. Commun.*, 6:5420, 2015.

[125] F. Ziebert, S. Swaminathan and I. S. Aranson. Model for self-polarization and motility of keratocyte fragments. *J. R. Soc. Interface*, 9:1084–92, 2012.

[126] S. Praetorius and A. Voigt. Collective cell behavior - a cell-based parallelization approach for a phase field active polar gel model. *Proceedings of the 9th NIC Symposium*, 49:369–376, 2018.

[127] U. M. B. Marconi and P. Tarazona. Dynamic density functional theory of fluids. *J. Chem. Phys.*, 110:8032–8044, 1999.

[128] A. J. Archer. Dynamical density functional theory for molecular and colloidal fluids: A microscopic approach to fluid mechanics. *J. Chem. Phys.*, 130:014509, 2009.

[129] R. Backofen *et al.* A continuous approach to discrete ordering on $\mathbb{S}^2$. *Multisc. Model. Sim.*, 9:314–334, 2011.

[130] R. Backofen, A. Voigt and T. Witkowski. Particles on curved surfaces: A dynamic approach by a phase-field-crystal model. *Phys. Rev. E*, 81:025701, 2010.

[131] C. A. Weber, C. Bock and E. Frey. Defect-mediated phase transitions in active soft matter. *Phys. Rev. Lett.*, 112:168301, 2014.

[132] J. Palacci *et al.* Living crystals of light-activated colloidal surfers. *Science*, 339: 936–940, 2013.

[133] J. Berry and M. Grant. Modeling multiple time scales during glass formation with phase-field crystals. *Phys. Rev. Lett.*, 106:175702, 2011.

[134] R. Backofen, A. Rätz and A. Voigt. Nucleation and growth by a phase field crystal (pfc) model. *Phil. Mag. Lett.*, 87:813–820, 2007.

[135] T. A. Davis. A column pre-ordering strategy for the unsymmetric-pattern multifrontal method. *ACM Trans. Math. Softw.*, 30:165–195, 2004.

[136] C. Y. and X.-C. C. A scalable implicit solver for phase field crystal simulations. In *Parallel and Distributed Processing Symposium Workshops PhD Forum (IPDPSW), 2013 IEEE 27th International*, 2013, pages 1409–1416.

[137] I. S. Aranson, A. Snezhko, J. S. Olafsen and J. S. Urbach. Comment on ”long-lived giant number fluctuations in a swarming granular nematic”. *Science*, 320:612–612, 2008.

[138] K. R. Elder, Z.-F. Huang and N. Provatas. Amplitude expansion of the binary phase-field-crystal model. *Phys. Rev. E*, 81:011602, 2010.

[139] S. Aland, H. Hatzikirou, J. Lowengrub and A. Voigt. A mechanistic collective cell model for epithelial colony growth and contact inhibition. *Biophys. J.*, 109: 1347–1357, 2015.

[140] R. Wittkowski *et al.* Scalar $\varphi^4$ field theory for active-particle phase separation. *Nat. Commun.*, 5:4351, 2014.

[141] T. Speck, J. Bialké, A. M. Menzel and H. Löwen. Effective Cahn-Hilliard equation for the phase separation of active brownian particles. *Phys. Rev. Lett.*, 112:218304, 2014.

[142] A. Das, A. Polley and M. Rao. Phase segregation of passive advected particles in an active medium. *Phys. Rev. Lett.*, 116:068306, 2016.

[143] J. Stenhammar, R. Wittkowski, D. Marenduzzo and M. E. Cates. Activity-induced phase separation and self-assembly in mixtures of active and passive particles. *Phys. Rev. Lett.*, 114:018301, 2015.

[144] F. Kümmel *et al.* Formation, compression and surface melting of colloidal clusters by active particles. *Soft Matter*, 11:1–5, 2015.

[145] A. Wysocki, R. G. Winkler and G. Gompper. Propagating interfaces in mixtures of active and passive brownian particles. *New J. Phys.*, 18:123030, 2016.

[146] S. R. McCandlish, A. Baskaran and M. F. Hagan. Spontaneous segregation of self-propelled particles with different motilities. *Soft Matter*, 8:2527, 2012.

[147] M. Zeitz, K. Wolff and H. Stark. Active brownian particles moving in a random lorentz gas. *Eur. Phys. J. E*, 40:23, 2017.

[148] A. Morin, N. Desreumaux, J.-B. Caussin and D. Bartolo. Distortion and destruction of colloidal flocks in disordered environments. *Nat. Phys.*, 13:63, 2017.

[149] A. Morin, D. Lopes Cardozo, V. Chikkadi and D. Bartolo. Diffusion, subdiffusion, and localization of active colloids in random post lattices. *Phys. Rev. E*, 96:042611, 2017.

[150] R. Ni, M. A. Cohen Stuart, M. Dijkstra and P. G. Bolhuis. Crystallizing hard-sphere glasses by doping with active particles. *Soft Matter*, 10:6609–6613, 2014.

[151] B. van der Meer, M. Dijkstra and L. Filion. Removing grain boundaries from three-dimensional colloidal crystals using active dopants. *Soft Matter*, 12:5630–5635, 2016.

[152] X. L. Wu and A. Libchaber. Particle diffusion in a quasi-two-dimensional bacterial bath. *Phys. Rev. Lett.*, 84:3017–20, 2000.

[153] C. Valeriani *et al.* Colloids in a bacterial bath: simulations and experiments. *Soft Matter*, 7:5228, 2011.

[154] D. F. Hinz, A. Panchenko, T.-Y. Kim and E. Fried. Motility versus fluctuations in mixtures of self-propelled and passive agents. *Soft Matter*, 10:9082–9089, 2014.

[155] H. Wensink and H. Löwen. Emergent states in dense systems of active rods: from swarming to turbulence. *J. Phys.: Condens. Matter*, 24:464130, 2012.

[156] M. Skoge, A. Donev, F. H. Stillinger and S. Torquato. Packing hyperspheres in high-dimensional euclidean spaces. *Phys. Rev. E*, 74:041127, 2006.

[157] T. Lubensky and J. Prost. Orientational order and vesicle shape. *J. de Phys. II*, 2: 371, 1992.

[158] H. Shin, M. Bowick and X. Xing. Topological defects in spherical nematics. *Phys. Rev. Lett.*, 101:037802, 2008.

[159] G. Skačej and C. Zannoni. Controlling surface defect valence in colloids. *Phys. Rev. Lett.*, 100:197802, 2008.

[160] T. Sanchez *et al.* Spontaneous motion in hierarchically assembled active matter. *Nature*, 491:431, 2012.

[161] S. DeChamp *et al.* Orientational order of motile defects in active nematics. *Nat. Mater.*, 14:1110, 2015.

[162] J. Elgeti, M. Cates and D. Marenduzzo. Defect hydrodynamics in 2d polar active fluids. *Soft Matter*, 7:3177–3185, 2011.

[163] S. P. Thampi and J. M. Yeomans. Active turbulence in active nematics. *Eur. Phys. J. Spec. Top.*, 225:651–662, 2016.

[164] L. Giomi, M. Bowick, X. Ma and M. Marchetti. Defect annihilation and proliferation in active nematics. *Phys. Rev. Lett.*, 110:228101, 2013.

[165] J. Tailleur and M. Cates. Statistical mechanics of interacting run-and-tumble bacteria. *Phys. Rev. Lett.*, 100:218103, 2008.

[166] S. Henkes, Y. Fily and M. Marchetti. Active jamming: Self-propelled soft particles at high density. *Phys. Rev. E*, 84:040301, 2011.

[167] J. Bialke, T. Speck and H. Lowen. Crystallization in a dense suspension of self-propelled particles. *Phys. Rev. Lett.*, 108:168301, 2012.

[168] L. M. Pismen. Dynamics of defects in an active nematic layer. *Phys. Rev. E*, 88: 050502, 2013.

[169] B. Leimkuhler and S. Reich. *Simulating Hamiltonian dynamics*. 2004.

[170] C. F. F. Karney. Geodesics on an ellipsoid of revolution. *arXiv:1102.1215*, 2011.

[171] A. Stukowski. Visualization and analysis of atomistic simulation data with OVITO the open visualization tool. *Model. Sim. Mat. Sci. Eng.*, 18:015012, 2010.

[172] A. Turner, V. Vitelli and D. Nelson. Vortices on curved surfaces. *Rev. Mod. Phys.*, 82:1301, 2010.

[173] I. Nitschke, A. Voigt and J. Wensch. A finite element approach to incompressible two-phase flow on manifolds. *J. Fluid Mech.*, 708:418, 2012.

[174] S. Reuther and A. Voigt. The interplay of curvature and vortices in flow on curved surfaces. *Multisc. Model. Sim.*, 13:632, 2015.

[175] I. Nitschke, S. Reuther and A. Voigt. Discrete exterior calculus (DEC) for the surface navier-stokes equation. In *Transport Processes at Fluidic Interfaces*, D. Bothe and A. Reusken, editors, 2017, pages 177–197.

[176] M. Bates, G. Skacej and C. Zannoni. Defects and ordering in nematic coatings on uniaxial and biaxial colloids. *Soft Matter*, 6:655–663, 2010.

[177] F. Serra. Curvature and defects in nematic liquid crystals. *Liquid Crystals*, 43: 1920–1936, 2016.

[178] J. Yeomans. Playful topology. *Nat. Mater.*, 13:1004, 2015.

# Selbstständigkeitserklärung

Die eingereichte Dissertation zum Thema

*Phase Field Modeling of Active Matter*

wurde am Institut für Wissenschaftliches Rechnen der Technischen Universität Dresden unter Betreuung durch Prof. Dr. rer. nat. Axel Voigt angefertigt. Hiermit versichere ich, dass ich die vorliegende Arbeit ohne unzulässige Hilfe Dritter und ohne Benutzung anderer als der angegebenen Hilfsmittel angefertigt habe; die aus fremden Quellen direkt oder indirekt übernommenen Gedanken sind als solche kenntlich gemacht. Die Arbeit wurde bisher weder im Inland noch im Ausland in gleicher oder ähnlicher Form einer anderen Prüfungsbehörde vorgelegt.

Dresden, den 4. September 2018

Francesco Alaimo